STRUCTURAL AND OPTICAL CHARACTERIZATION OF NANOPARTICLES BY CO-PRECIPITATION METHOD

Project report submitted to the Department of Physics
ST. MARY'S COLLEGE (AUTONOMOUS)
THOOTHUKUDI
Affiliated to MANONMANIUM SUNDARANAR UNIVERSITY,
TIRUNELVELI

In partial fulfilment of the requirement for the award of
BACHELOR'S DEGREE IN PHYSICS

BY

S.V. Abi Nivetha - 20AUPH01

S. Anna Swathi - 20AUPH03

G.M. Nithiya Sri - 20AUPH23

E. Snowfina - 20AUPH35

S. Sundarammal@Gayathiri - 20AUPH37

Under the guidance of

Mrs. P. Dhanalakshmi M.Sc., B.Ed., SET

Department of Physics

ST. MARY'S COLLEGE (AUTONOMOUS)

Reaccredited with 'A+' Grade by NAAC
Thoothukudi

2022-2023

CERTIFICATE

This is to certify that this project work entitled "**STRUCTURAL AND OPTICAL CHARACTERIZATION OF NANOPARTICLES USING CO-PRECIPITATION METHOD**" is submitted to **ST. MARY'S COLLEGE (AUTONOMOUS), THOOTHUKUDI** in partial fulfilmem for the award of Bachelor's degree in Physics and is a record of the work done during the year 2022-2023 by the following students.

S.V. Abi Nivetha	- 20AUPH01
S. Anna Swathi	- 20AUPH03
G.M. Nithiya Sri	- 20AUPH23
E. Snowfina	- 20AUPH35
S. Sundarammal@Gayathiri	- 20AUPH37

Dhanalakshmi. P
GUIDE

13/4/23
EXAMINER

HEAD OF THE DEPARTMENT
HEAD
Department of Physics,
St. Mary's College (Autonomous),
Thoothukudi - 628 001.

Lucia Rose
PRINCIPAL
St. Mary's College (Autonomous)
Thoothukudi - 628 001.

DECLARATION

We hereby declare that the project entitled, **'SYNTHESIS AND OPTICAL CHARACTERISATION OF NANOPARTICLES BY COPRECIPITATION METHOD'** submitted to St. Mary's college (Autonomous), Thoothukudi, affiliated to Manonmaniam Sundaranar University, for the Bachelor's Degree of Science in Physics is our original work and that, it has not previously formed the basis for the award of any Degree, Diploma or similar title.

S.V. Abi Nivetha - 20AUPH01

S. Anna Swathi - 20AUPH03

G.M. Nithiya Sri - 20AUPH23

E. Snowfina - 20AUPH35

S. Sundarammal@Gayathiri - 20AUPH37

Station: Thoothukudi

Date: 03/04/2023

ACKNOWLEDGEMENT

First and Foremost, we feel obliged to our Almighty for his aid in the completion of our project work successfully.

We express our deepest gratitude to our Principal, Dr. Sr. A.S.J. Lucia Rose, M.Sc., M.Phil., Ph.D., PGDCA., for providing us with necessary facilities that enabled us to complete our project auspiciously.

We are very obliged to the head of our Department, Dr. Sr. Jessie Fernando, M.Sc., M.Phil., Ph.D., for providing us with an environment to complete our project triumphantly.

We are bound to our guide Mrs. P. Dhanalakshmi, M.Sc., B.Ed., SET for the useful ideas and guidance in bringing out this project successfully.

Words cannot express our gratitude to the non-teaching staff who helped us wholeheartedly.

We would like to extend our gratitude to the Marian Star Centre, St. Mary's College and the department of Physics, Manonmaniam Sundaranar University, Tirunelveli for their timely help in completing our project.

We also thank all the staff members, our family and friends for their help to make this project a successful one.

TABLE OF CONTENT

AIM OF THE PROJECT:

As nanoparticle is the growing field of future, it has numerous applications in various fields. Nanoparticles pave way for next computing generation. In the present investigation, the aim is to review the advanced application of the nanomaterials. Hence, as a step of interest we decided to prepare the CuI nanoparticles that has efficient applications as catalyst, a very efficient inorganic p-type material and also has potential applications in polymer solar cells.

CHAPTER I

INTRODUCTION

INTRODUCTION:

Nanoscience materials have been widely studied because of their better properties compared to bulk size.

Nanotechnology is the science that deals with:

1. Matter at the scale of 1 billionth of a meter
2. Study of manipulating matter at the atomic and molecular scale

Nanotechnology also lowers costs, produces stronger and lighter wind turbines, improves fuel efficiency and the thermal insulation of some nanocomponents, can save energy. Nanotechnology has seen a prosperous growth. It is well used and can be fundamental in the near future. Nanotechnology is often referred to as "The Future of Technology".

NANOPARTICLES:

Nanoparticles take a special place in Nanoscience and Nanotechnology because of their reduced dimensions and promising building blocks. This chapter gives an overview of the presence of nanoparticles in everyday life. It highlights the use of nanoparticles to obtain different end-products in different sectors of economic activity. The size of nanoparticles range between 1 nm and 100 nm. The nanoparticles have different physical and chemical properties. The optical property is one of the fundamental attractions and a characteristic of nanoparticles.

For example:

- A 20 nm gold nanoparticle has a characteristic with red colour
- A silver nanoparticle is yellowish grey

Nanoscale materials often present properties different from their bulk counterparts, as their high surface-to-volume ratio results in an exponential

increase of the reactivity at molecular level. The properties include electronic, optical, chemical and mechanical. Recently synthesized nanoparticles require the development of more precise and creditable protocols for their characterization. Some of the characterizations are incomplete sometimes due to the inherent difficulties of nanoscale materials. In addition, the multidisciplinary aspects of nanoscience and nanotechnology do not permit every research team to access easily to the broad range of characterization facilities. Characterization of nanoparticles requires a comprehensive approach. It is desirable to know the limitations and strengths of different techniques, in order to know if in some cases, the use of only one or two of them are enough to provide reliable information when studying a specific parameter (e.g. particle size). Nanoscience and nanotechnology are still undergoing constant growth, and the scientific community is rather aware that there may be certain differences between the way analytical characterization methods operate for nanomaterials, in comparison with the more 'traditional' modes of use for more 'conventional' (macroscopic) materials.

ADVANTAGES OF NANOPARTICLES:

- Enhancement of solubility and bioavailability
- Enhancement of pharmacological activity
- Sustained drug delivery
- Protection from degradation
- Enhancement of permeability
- Decreased side effects compared to conventional drug delivery
- Improved therapeutic effect

PROPERTIES OF NANOPARTICLES:

There are three major physical properties of nanoparticles, and all are interrelated:

(1) They are highly mobile in the free state

(2) They have enormous specific surface areas

(3) They may exhibit what are known as quantum effects.

Thus, nanoparticles have vast range of compositions, depending on the use of the product.

APPLICATIONS OF NANOPARTICLES:

Many benefits of nanotechnology depend on the fact that it is possible to tailor the structures of materials as extremely small scales to achieve specific properties, thus greatly extending the materials science toolkit. Using nanotechnology, materials can effectively be made stronger, lighter, more durable, more reactive, more sieve-like, or better electrical conductors, among many other traits.

- ✓ Nanoscale additives to or surface treatments of fabric can provide lightweight ballistic energy deflection in personal body armour, or can help them resist wrinkling, staining, and bacterial growth
- ✓ Clear Nano scale films on eyeglasses, computer and camera displays, windows and other surfaces can make them water and residue- repellent, antireflective, self-cleaning, resistant to ultraviolet or infrared light, antifog, antimicrobial, scratch-resistant or electrically conductive.

- ✓ Nanoscale materials are beginning to enable washable, durable "smart fabrics" equipped with flexible nanoscale sensors and electronics with capabilities for health monitoring, solar energy capture, and energy harvesting through movement.

- ✓ Light weighting of cars, trucks, airplanes, boats and space craft could lead to significant fuel savings. Nanoscale additives in polymer composite materials are being used in baseball bats, tennis rackets, bicycles, motorcycle helmets, automobile parts, luggage, and power tool housings, making them lightweight, stiff, durable and resilient. Carbon nanotubes sheets are now being produced for use in next generation air vehicles.

- ✓ Nano-engineered materials in automotive products include high-power rechargeable battery systems; thermoelectric materials for temperature control; tires with lower rolling resistance; high-efficiency/low-cost sensors and electronics; thin-film smart solar panels; and fuel additives for cleaner exhaust and extended range.

- ✓ Nanostructured ceramic coatings exhibit much greater toughness than conventional wear-resistant coatings for machine parts. Nanotechnology-enabled lubricants and engine oils also significantly reduce wear and tear, which can extend the lifetime of moving parts in everything from the power tools to industrial machinery.

- ✓ Nanoscale materials are also being incorporated into a variety of personal care products to improve performance. Nanoscale titanium dioxide and zinc oxide have been used for years in sunscreen to

provide protection from the sun while appearing invisible on the skin.

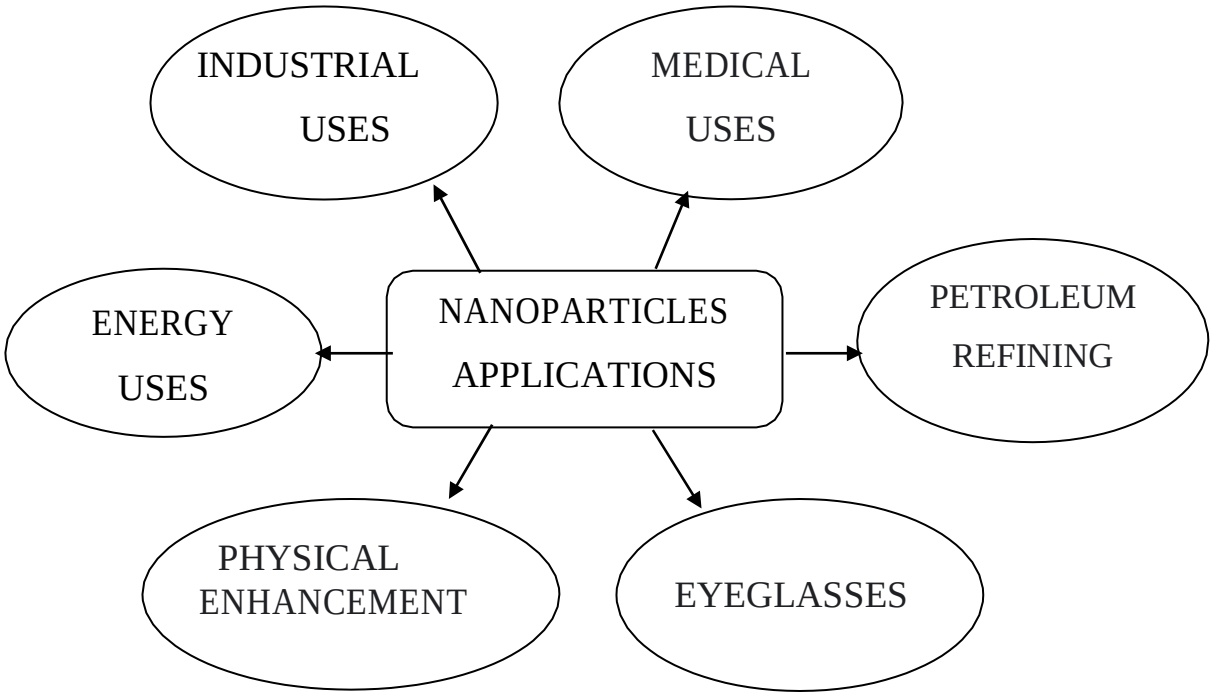

SYNTHESIS APPROACH:

Top-down approach

The top-down approach uses initial macroscopic structures. The methods begin with larger particles which are reduced to

Methods in top-down approach:

1. Physical vapour deposition
2. Chemical vapour deposition
3. Ion implantation
4. Electron beam lithography
5. X-ray lithography

Bottom-up approach:

Bottom-up approaches of production of nanomaterials comprise the miniaturisation of material constituents to the atomic level with the additional procedure leading to the development of nanostructures. Throughout the further progression, the physical forces working at nanoscale combined simple units into larger stable structures.

The methodology is principally based on the principle of molecular recognition (self-assembly). Self-assembly means growing more and more things about one's kind from them. Many of these techniques are still under development or are just beginning to be used for the commercial production of nanoparticles.

Methods in a bottom-up approach:

1. Sol-gel synthesis
2. Colloidal precipitation
3. Hydrothermal synthesis
4. Organometallic chemical route
5. Electrodeposition

FACTORS AFFECTING THE SYNTHESIS OF NANOPARTICLES:

- Temperature
- Pressure
- Time
- Particle size and shape
- Cost of preparation
- Pore size

METHODS OF SYNTHESIS:

There are three kinds of approaches for the production of nanoparticles

1. Physical Methods
2. Chemical Methods
3. Biological Methods

A. Physical methods

- ✓ Mechanical Method
- ✓ Pulse Laser Ablation
- ✓ Pulsed Wire Discharge Method
- ✓ Chemical Vapour Deposition

- ✓ Laser Pyrolysis
- ✓ Ionized Cluster Beam Deposition

B. Chemical methods

- ✓ Sol-gel Method
- ✓ Sonochemical Synthesis
- ✓ Co-precipitation Method
- ✓ Inert Gas Condensation Method
- ✓ Hydrothermal Synthesis

C. Biological methods

- ✓ Synthesis Using Microorganisms
- ✓ Synthesis Using Plant Extracts
- ✓ Synthesis Using Algae

FUTURE OF NANOTECHNOLOGY:

Nanotechnology can change dental medicine, healthcare, and human life more profoundly than several developments of the past. However, they even have the potential to evoke important advantages, like improved health, higher use of natural resources, and reduced environmental pollution.

1.9 REVIEW OF LITERATURE:

❖ Synthesis and characterization of nanoparticles using Oxidation method is done as a chemistry laboratory project which involve CuI synthesize and analysis by Lara A. Margolis, Richard Schreffer and Claude Yoder Department of chemistry, Franklin and Marshall College. It is published in ACS publication.

❖ Synthesis, Purification and UV-vis Spectrophotometric analysis of copper iodide by Haina Wang is used for the synthesize of crude CuI via redox reaction and to purify it using KI solution and also for the determination of the purity of the sample

❖ Aparna Calindi, Parisa Ansari CHEM 2133, Department of Chemistry have gone through the experiment on formation of Copper iodide to know its behaviour and its chemistry and also for determination of the purity of the compound.

❖ Kauffman G. B, Fang, L.Y. has carried out purification of copper iodide using KI solution this states the characteristic and uses of CuI. This is the laboratory preparation of CuI

❖ Synthesis and characterization of Copper Iodide nanoparticles through chemical route is studied by Mohd Rafi Johan, Kok Si-Wen, Norliza Hawari, Nurul Azri Khalisah Aznan Department of mechanical engineering, University of Malaya.

❖ Co-precipitation Preparation of Cu/Zn/Al-Hydrotalcite-Like Compound for Copper Removal from Electroplating Wastewater by Dongxia Huo, Quan Hong Ying, Ni Wang and Baixue Xia, Chengdu University of Technology, China. They state that coprecipitation synthetic technology and prepared Cu/Zn/Al-HTlc could be potentially used for electroplating wastewater treatment.

❖ A practical approach to particle size characterization of nanoparticles is done by B. Akbari, M. PirhadiTavandashil and M. Zandrahiml Department of material science and Engineering, University of Kerman. It states that the novel properties of nanoparticles do not prevail until the size has been reduced to the nanometer scale and also there is a good correlation between the BET, XRD and TEM measurements other than PCS that is sensitive to the presence of the agglomerates.

❖ Khi PoayBeh, Raed Abdalrheem, Fong Kwong Yam undergone a preliminary study of CuI as a potential UV sensing material. This suggests the possibility of employing CuI as a visible blind-UV photodetector. In terms of UV-sensing, CuI exhibited greatest responds under UVA ambient, followed by both UVB and UVC. This preliminary study indicated CuI as a potential UV sensing material, which can be improved upon in future.

❖ Copper iodide nanoparticles on poly (4-vinylpyridine): A new and efficient catalyst for the synthesis of 1,8-dioxooctahydroxanthenes under solvent-free conditions was studied by Jalal Albadi, Mosadegh Keshavarz Masoumeh Abedini and MoloudKhoshkhilagh, Department of chemistry,

Yasouj University. The catalyst can be recovered using simple method and runs without losing efficiency.

❖ Copper Iodide (CuI) for Multifunctional p-Type Transparent Semiconductors and Conductors researched by Ao Liu, Huihui Zhu, Myung Gil Kim, Junghwan Kim, Yong-Young Noh. CuI can form thin films with high transparency in the visible light region using various low-temperature deposition techniques. This progress report aims to provide a basic understanding of CuI-based materials and recent progress in the development of various devices.

❖ Study of the morphological Transformation of Copper Iodide nanostructures prepared by Sugar beet mediated route is done by Javid. Anwar, y. Jamil, B. Abbas and some more researchers belongs to physics department, University of Agriculture. Prepared sample was investigated by XRD, SEM, EDX, UV-Vis SPECTROGRAPHY.

❖ The properties of Copper Iodide thin films prepared by M. N Amalina, Y. Azilawati, N.A. Rashied and M. rusop at different doping concentration. They prepared CuI thin films using Mister Atomizer technique or called spray pyrolysis

❖ Overview on the methods of synthesize of nanoparticle is given by Nilesh Patel, Rajveer Bhaskar, Vishal Vyavhare, Rahul Dhadge, VaishnaviKhaire, Yogeshpatil, Department of quality assurance. Their review mainly focuses on approaches used for production of nanoparticles and different methods of synthesize of nanoparticles

❖ Copper (I) iodide nanoparticles on polyaniline as a green, recoverable and reusable catalyst for multicomponent click synthesis of 1,4-disubstituted-1H-1,2,3-triazoles by Shervin Saadat, Simin Nazan, Mozhgan Afshari, Maryam Shahabi, MosadeghKeshavarz using one pot procedure with polyaniline catalyst.

❖ Copper Iodide Nanoparticles-Catalyzed Cyanation of Aryl Halides Using Non-Toxic $K_4[Fe(CN)_6]$ in the Presence of 1,2-Bis(5-Tetrazolyl) Benzene as an Efficient Ligand was given by Mehdi Maham and Siavash Bahari. This is published in Journal of Chemical research. This method has advantage of high yields.

❖ A review on Characterization techniques of Nanomaterials was done by Sathish Boddolla and Satyanarayana Thodeti Assistant professors of physics made their review to describe the instruments and experimental set ups to measure the characterization of synthesized nanoparticles.

1.9 AIM OF THE EXPERIMENT:

- To synthesis CuI nanoparticle using Co-precipitation method
- To characterize the CuI nanoparticle using XRD
- To characterize the CuI nanoparticle using FTIR
- To characterize the CuI nanoparticle using UV spectroscopy

CHAPTER II

COPPER IODIDE

CO-PRECIPITATION METHOD:

DEFINITION:

It is the simultaneous precipitation of a normally soluble component with a macro-component from the same solution by the formation of mixed crystals, by adsorption, occlusion or mechanical entrapment.

Using this process, it is possible to prepare flowable powders without any additional agglomeration steps. One can tailor the process to get nano or micron size particles by adjusting the pH, the precipitating agent, temperature and solvents.

This process has been successfully used for the precipitation of ceramic oxide powders suitable for suspension plasma spraying and powder plasma spraying.

It is a wet chemical process, also called a solvent displacement method. Polymer phase can be synthetic or natural; polymer- solvent is ethanol, acetone, and hexane and Nano solvent polymer. Nanoparticles are produced by rapid diffusion of polymer –solvent into a non-solvent polymer phase by mixing the polymer solution at last.

Nanoparticles are produced by interfacial tension at two phases.

CHEMICAL PRECIPITATION ADVANTAGES:

- Permanent
- Immediate results
- Efficient
- Easily implemented
- Easy to monitor

Chemical precipitation offers many advantages as a treatment alternative. It is able to meet stringent discharge criteria. It has been used effectively for many years. The design of the treatment process can be customized and thus can be used in a variety of situations. Chemical precipitation is a long-term remedy that can address both acute and chronic risks to human and ecological receptors. It provides a relatively rapid effect in the reduction of contamination in downgradient surface water bodies. Advances in remote monitoring have increased the ability for chemical precipitation to be used in locations previously prohibitive

LIMITATIONS:

- High cost
- Not applicable for all cases
- Requires operation and maintenance (O&M)
- Requires power
- May generates a waste product

Disadvantages or limitations of chemical precipitation include the traditionally active nature of the process. Chemical reagents need to be procured, energy inputs and manual oversight are required, and a waste stream is generated. These can equate to a relatively high cost for treatment.

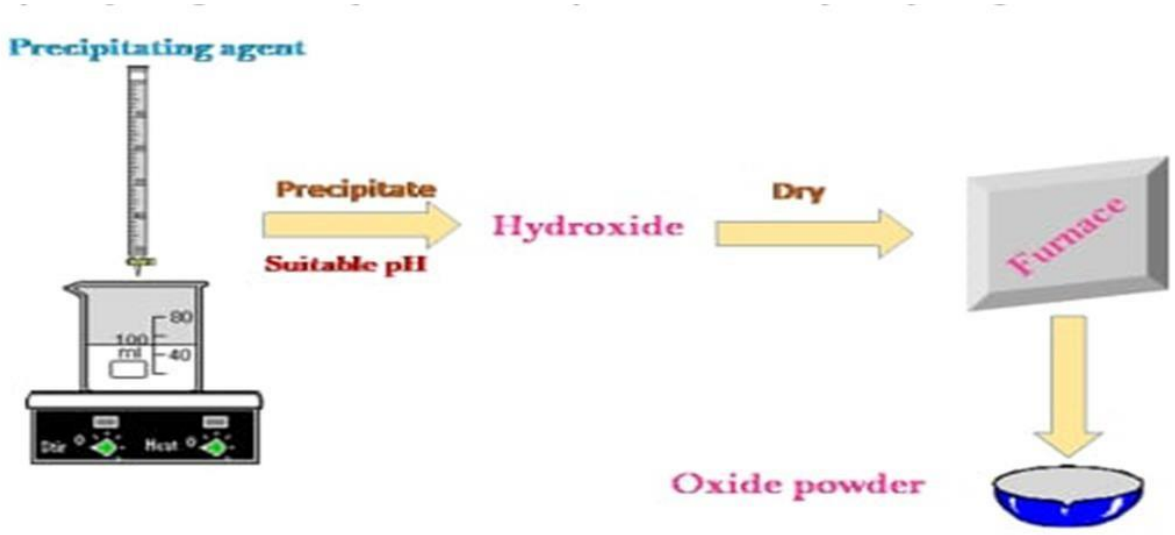

COPPER IODIDE (CuI):

IUPAC NAME: Copper (I) iodide

It is the inorganic compound with the formula CuI. It is also known as cuprous iodide. It is useful in a variety of applications ranging from organic synthesis to cloud seeding.

Copper(I)iodide is soluble in ammonia, thiosulphate, sodium and potassium iodide solutions and insoluble in water and dilute acids. The CuI NPs were reused and recycled without any loss of activity and product yield.

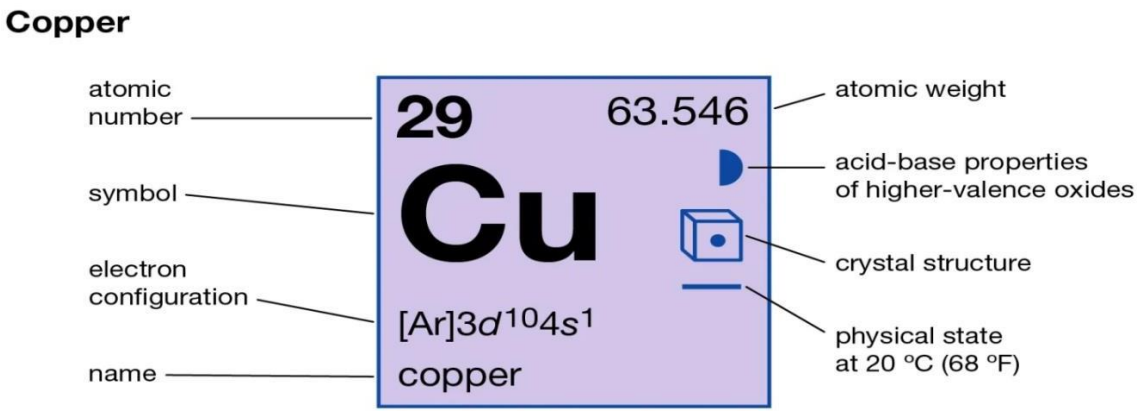

Cu is a soft, malleable, and ductile metal with very high thermal and electrical conductivity. Copper has a melting point of 1083.4 +/- 0.2°C, boiling point of 2567°C, specific gravity of 8.96 (20°C), with a valence of 1 or 2. Copper is reddish colored and takes a bright metallic luster. Copper is soft, but it is tough. It is easily mixed with other metals to form alloys such as bronze and bronze. Maybe 70% of the copper actually in use has been recycled at least once. The primary applications of copper are in electrical wiring, roofing, plumbing, and industrial machinery.

STRUCTURE OF CuI:

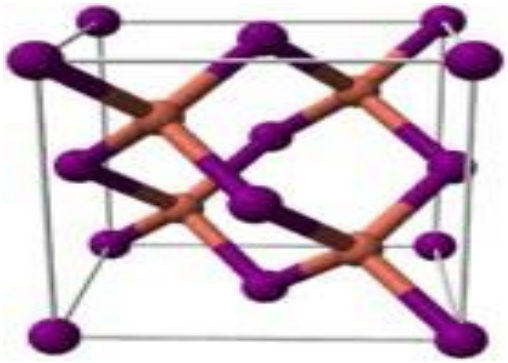

CRYSTAL STRUCTURE: Cubic close packed

COORDINATION GEOMETRY: Tetrahedral

IMAGE OF CuI:

PROPERTIES OF CuI:

The salient features of the copper iodide nanoparticles are: easy preparation, cost-effective, high stability, low loading and reusability of the catalyst. The prepared copper iodide nanoparticles were fully characterized by XRD, EDX, FT-IR, SEM and TEM analysis

Molecular Formula	CuI
Molar Mass	190.45

Density	5.62 g/mL at 25 °C (lit.)
Melting Point	605 °C (lit.)
Boling Point	1290 °C/1 atm (decomp)(lit.)
Flash Point	1290 °C
Water Solubility	INSOLUBLE
Solubility	Soluble in water (0.08 mg/ml at 20 °C). Insoluble in alcohol, and dilute acids.
Vapour Pressure	10 mm Hg (656 °C)
Appearance	Brown crystal
Specific Gravity	5.62
Colour	White to Pale Brown
Exposure Limit	ACGIH: TWA 1 mg/m3; TWA 0.01 ppm NIOSH: IDLH 100 mg/m3; TWA 1 mg/m3
Solubility Product Constant (Ksp)	pKsp: 11.9
Merck	14,2662
Storage Condition	Store below +30°C.

Sensitive	Air & Moisture Sensitive
Refractive Index	2.346
MDL	MFCD00010978

CHAPTER III

PREPARATION OF CuI

MATERIALS USED:

- ❖ Salt 1: Potassium Thiosulphate
- ❖ Salt 2: Copper chloride
- ❖ Salt 3: Potassium Iodide
- ❖ Distilled water
- ❖ Magnetic stirrer, burette, beaker
- ❖ Filter paper, Muffle furnace

PREPARATION:

- ❖ 0.1 M of Potassium Thiosulphate and 0.1 M of Copper chloride are mixed with 100 ml of distilled water each in SMF
- ❖ The solutions were stirred using magnetic stirrer
- ❖ Then these are mixed to form a combined single solution by dripping method
- ❖ By the time 0.1 M of potassium Iodide is mixed with 100 ml of distilled water
- ❖ This solution is dripped to mix with the combined solution
- ❖ The resultant solution is left to precipitate
- ❖ The precipitate was separated from the mother liquid which contained the side products by washing three times using distilled water
- ❖ The cleansed precipitate was filtered using filter paper and was allowed to dry naturally and also using oven maintained at 60^0c
- ❖ The dried product was then powdered and calcined at 200^0c for an hour in muffle furnace
- ❖ It was finely powdered and measured in different quantities, then sent for tests like XRD, UV-Vis spectroscopy and FITR

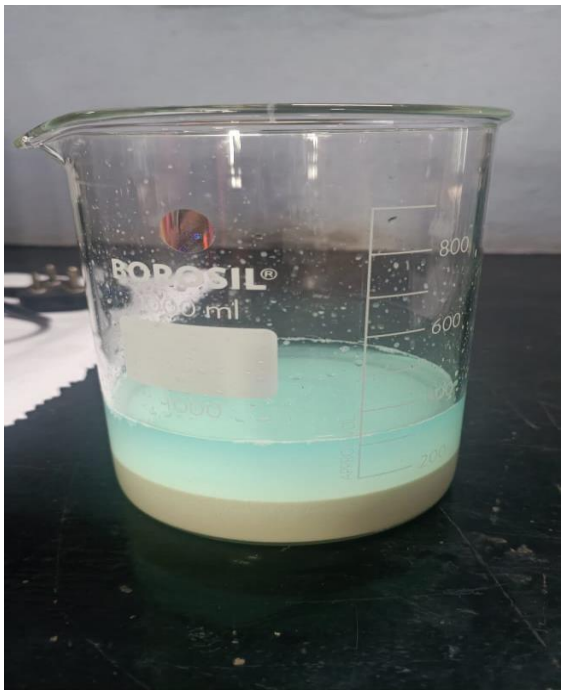
800
600

FLOWCHART:

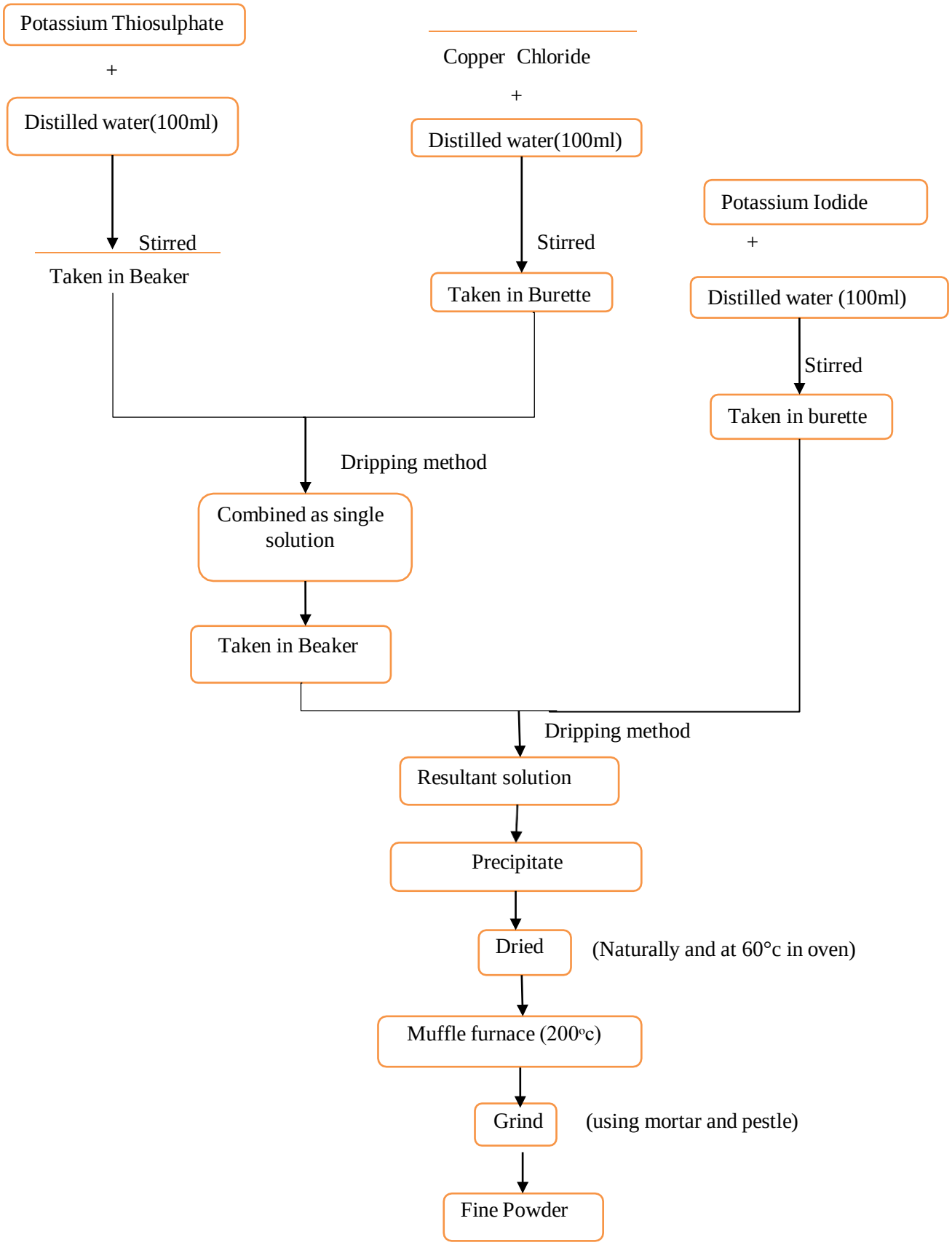
Potassium Thiosulphate
+
Distilled water(100ml)
Stirred
Taken in Beaker
Copper Chloride
+
Distilled water(100ml)
Stirred
Taken in Burette
Potassium Iodide
+
Distilled water (100ml)
Stirred
Taken in burette
Dripping method
Combined as single solution
Taken in Beaker
Dripping method
Resultant solution
Precipitate
Dried
(Naturally and at 60°c in oven)
Muffle furnace (200°c)
Grind
(using mortar and pestle)
Fine Powder

CHAPTER IV

CHARACTERISTIC TECHNIQUES

CHARACTERISTIC TECHNIQUES:

Methods such as electron microscopy, the various scanning microscopy methods, IR-, UV-, or FTIR-spectroscopy, NMR, EPR, or MS, X-ray diffraction and scattering are considered important due to two essential reasons:

- X-ray diffraction is virtually non-destructive, and
- X-ray photons with a wavelength in the nm range are the ideal sensor for the Nano cosmos.

XRD:

- X-ray diffraction offers a number of different dedicated methods to investigate nanostructures:
- X-ray Reflectometry (XRR) determines layer thickness, roughness, and density;
- High-Resolution X-ray Diffraction (HRXRD) helps to verify layer thickness, roughness, chemical composition, lattice spacing and mismatches, relaxation, etc.
- X-ray diffuse scattering to determine lateral and transversal correlations, distortions, density, and porosity; in-plane gracing incidence diffraction (IP-GID) to study lateral correlations of thinnest organic and inorganic layers, and depth profiling.
- Small Angle X-ray Scattering (SAXS) in transmission or gracing incidence SAXS (GISAXS) in reflection to determine the size, the shape, the distribution, orientation, and correlation of nanoparticles present in solids or solutions.
- Background X-ray diffraction (XRD) is a powerful method for the study of nanomaterials. The wavelength of X-rays is on the atomic

scale, so X-ray diffraction (XRD) is a primary tool for probing structure of Nano-materials. The intensities measured with XRD can provide quantitative, accurate information on the atomic arrangements at interfaces. With lab-based equipment, surface sensitivities down to a thickness of ~50Å are achievable, but synchrotron radiation allows the characterization of much thinner films and for many materials, monoatomic layers can be analyzed.

- ❖ XRD is non-contact and non-destructive, which makes it ideal for in situ studies.
- ❖ X-ray diffractograms of nanomaterials provide a wealth of information - from phase composition to crystallite size, from lattice strain to crystallographic orientation. The main use of powder diffraction is to identify components in a sample by a search/match procedure. Furthermore, the areas under the peak are related to the amount of each phase present in the sample.
- ❖ The powder diffraction method is ideally suited for characterization and identification of polycrystalline phases.

Experimental Arrangements:

A typical powder XRD instrumentation consist of four main components such as

- X-ray source,
- Specimen stage,
- Receiving optics and
- X-ray detector.

The source and detector with its associated optics lie on the circumference of focusing circle and the sample stage at the center of the circle. Bragg's law is

the basis of XRD analysis. The angle between the plane of the specimen and the X-ray source is Theta, known as Bragg's angle and the angle between the projection of X- ray and the detector is 2Thetta.

The peak depends on the wavelength of the anode material of the X-ray tube. By choosing the right anode and energy of accelerated electrons, a known wavelength and therefore a known energy of X-rays will be generated. Copper X-ray tubes are most commonly used for X-ray diffraction of inorganic materials. For practical applications of X-ray diffraction, we typically want to use x-rays of a single wavelength, i.e. monochromatic radiation to improve experimental radiation is used for analytical work while allθresults. In general, K, etc.) are removed by means of a nickel filter.

The Bragg's law is as follows:

$$2d \sin \theta = n \lambda$$

The first step of X-ray diffraction pattern involves the indexing (assigning miller indices to each peak) of XRD peaks. The most common wavelength used in XRD is 1.54 Å ($Cu K_{\alpha}$).

The Scherrer formula

$$D = \frac{K \lambda}{\beta \cos\theta}$$

Where

D is the average particle size

λ is wave length of the radiation and

β is the full width half maximum of the diffraction peak

K is the Scherrer constant.

FTIR:

Fourier transform infrared spectroscopy (FTIR) is a technique based on the measurement of the absorption of electromagnetic radiation with wavelengths within the mid-infrared region (4000–400 cm^{-1}). FTIR is an easy, simple, fast, suitable, non-invasive and cost-effective method.

FTIR spectrometer consists of a source, interferometer, sample compartment, detector, amplifier, A/D converter, and a computer.

HOW DOES FTIR WORKS?

A molecule's covalent bonds will selectively absorb radiation of specific wavelengths, which changes vibrational energy in bonds. The type of vibration induced by the infrared radiation depends on the atoms in the bond. The spectrum is recorded on a graph with wave number (cm^{-1}) recorded on the X-axis and transmittance recorded on the Y-axis.

WHY FTIR IS PREFERRED METHOD?

- Doesn't destroy the sample
- Faster than older techniques
- More sensitive and precise

WHAT INFORMATION CAN FTIR PROVIDE?

- Identify unknown materials
- Determine the quality of a sample
- Determine the amount of components in a mixture

The example of absorption spectrum graph is given below:

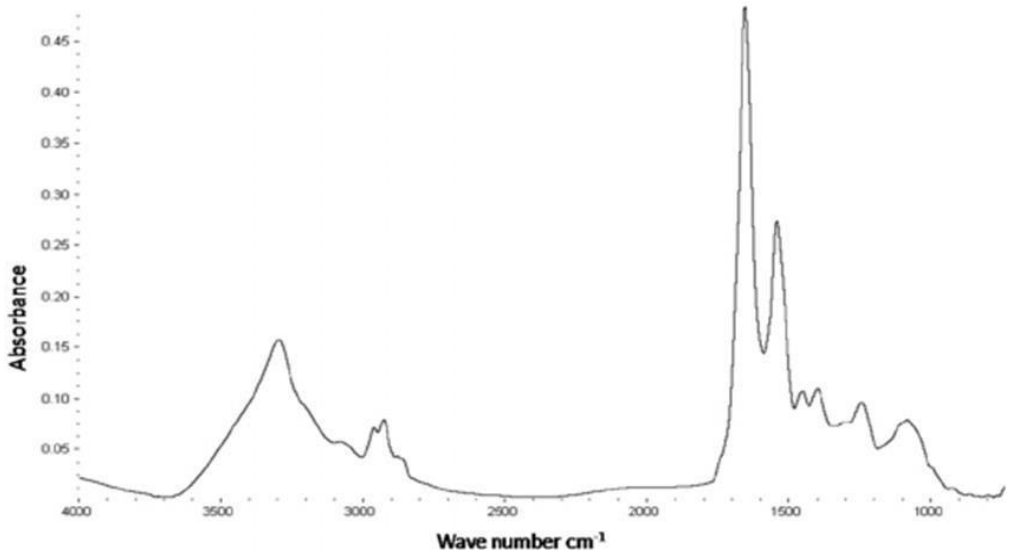

UV-Vis Spectroscopy:

UV-Vis spectroscopy is an analytical technique that measures the amount of discrete wavelengths of UV or visible light that are absorbed by or transmitted through a sample in comparison to a reference or blank sample. A Method that is versatile, reliable, and economical, can be used for the characterization of nanoparticles even at very low concentrations.

Absorption spectroscopy uses electromagnetic radiation between 190 and 800 nm and is divided into the ultraviolet (190-400 nm) and visible (400-800 nm) regions. It measures the intensity of light reflected from a sample and compares it to the intensity of light reflected from a reference material.

Nanoparticles that have optical properties that are sensitive to size, shape, concentration, agglomeration state and refractive index near the NP surface, which makes UV-Vis spectroscopy an important tool to identify, characterize and investigate these materials, and evaluate the stability of NP colloidal solutions.

HOW DOES A UV-Vis SPECTROSCOPY WORK?

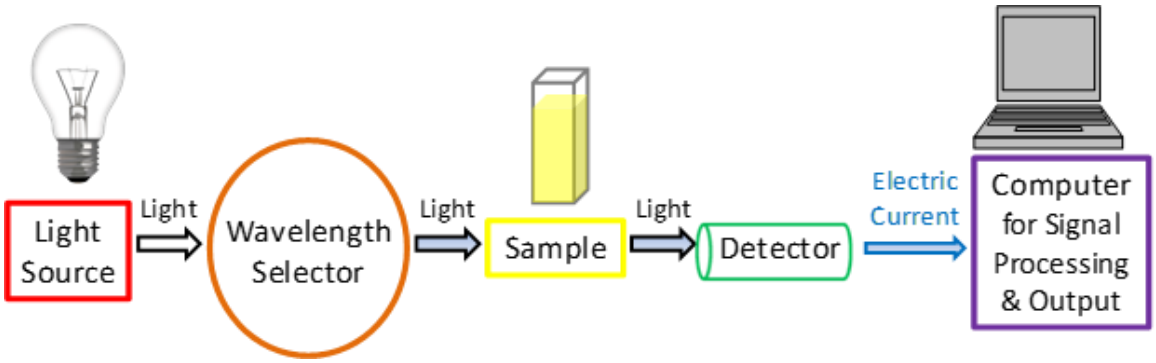

WHAT INFORMATION CAN UV-Vis PROVIDE?

- To identify the molecules in a sample
- Determining the concentration of a compound in a sample
- Characterizing the rate of a chemical reaction
- Determine purity or concentration of biological samples

CHAPTER V

RESULTS

RESULTS:

XRD analysis:

Figure (1) shows that XRD patterns for nanoparticles of CuI.

When X-rays was allowed to incident on a crystalline sample, they are diffracted in a pattern as dictated by the characteristic of the crystal structure. The Bragg's law imposes the condition for constructive interference to obtain XRD patterns. The XRD patterns show that the peaks for nanoparticles CuI matched well with the standard fcc structure of CuI and are in good agreement with the reported standards (JCPDS card no. 76-0207). The 2θ values are 25.5, 29.5, 42.2, 50, 61.2, 67.4, and 77.1. The average particle size was calculated to be 11.51 nm using Scherrer formula.

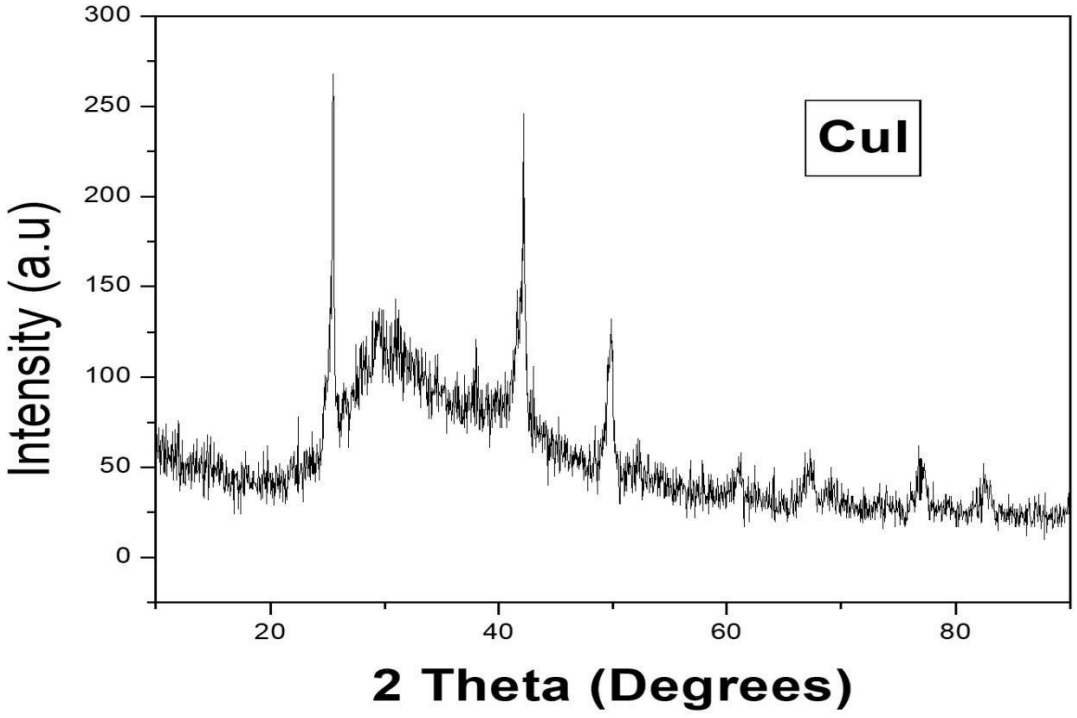

(Figure 1)

Table 1:

Sample	Observed 2Ɵ (deg)	FWHM (radian)	Crystallite size (nm)	Average crystallite size (nm)
CuI	25.5	0.4450	19.13	11.51
	29.5	0.5146	16.68	
	42.2	0.7365	12.09	
	50	0.8722	10.50	
	61.2	1.0676	9.03	
	67.4	1.1757	8.49	
	69.4	1.2106	8.34	
	77.1	1.3449	7.89	

FTIR Technique:

FTIR Technique is one of the most essential and extensively used spectroscopic techniques to identify the functional group, to determine the internal structure of the molecules and to understand the nature of the chemical environment in the given compound.

Figure (2) shows that FTIR spectrum nanoparticles for CuI.

The spectrum shows a broad band around 3000 cm^{-1} due to intermolecular hydrogen bonding present in the water molecules.

The peaks at 616 and 449 cm^{-1} are the two characteristic peaks of CuI stretching which confirms the formation of CuI nanoparticles. The peak at 1100 cm^{-1} corresponds C-O stretching.

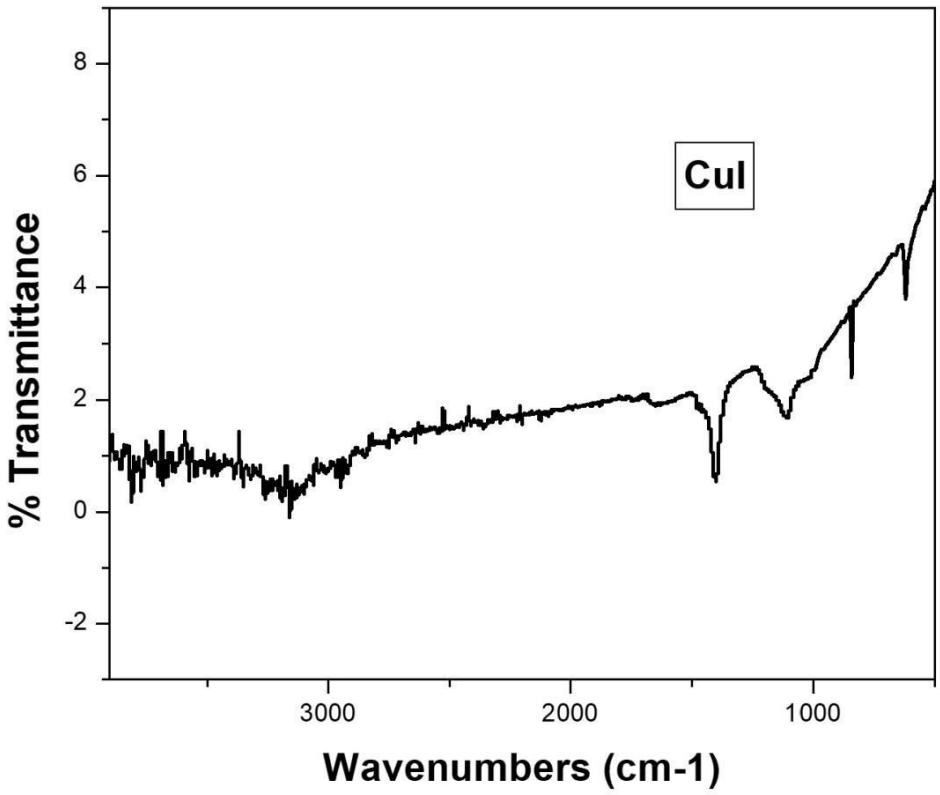

(Figure 2)

UV-Visible spectroscopy:

Figure 3 shows the absorbance spectra of as-prepared CuI spectrum. It is clear that high absorption in the UV region depicted a major peak at the UV region at 398 nm (3.1eV). This is attributed to the exciton band gap recombination of γ-CuI. The UV absorbance peak reveal that this material is wide band gap with direct transition.

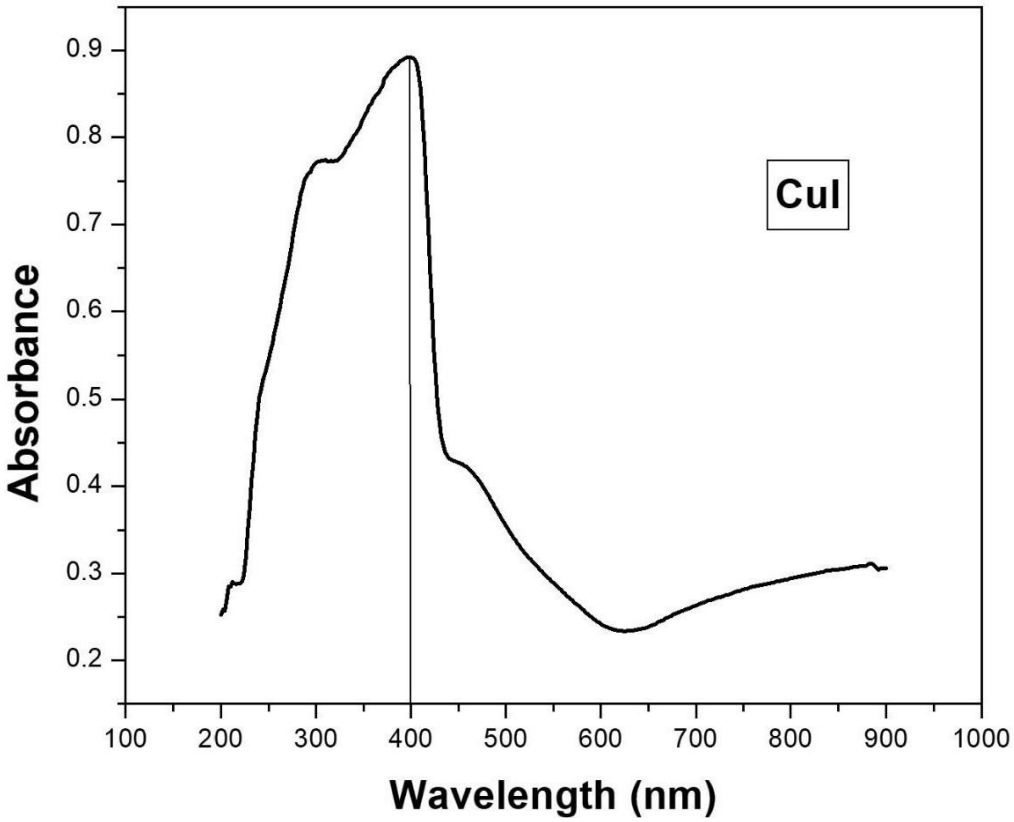
CuI
Absorbance
Wavelength (nm)
0.9
0.8
0.7
0.6
0.5
0.4
0.3
0.2
100
200
300
400
500
600
700
800
900
1000

(Figure 3)

CHAPTER VI

CONCLUSION

SUMMARY:

The CuI nanoparticles were prepared by Co-precipitation method. The structural and optical properties were studied. The CuI structural features were determined with the help of XRD analysis.

The XRD diffraction pattern of CuI displayed intense peaks and 2θ values that were in agreement with the standard value of CuI (JCPDS card.no 76-0207). The structure of the sample is confirmed and the average size of the particle is 11.51 nm.

The optical properties of CuI were studied using UV-Vis spectroscopy. The peak observed at 398 nm indicates the presence of CuI. The band gap was found to be 3.12 eV.

The FT-IR shows broadband peaks at 616 and 449 cm^{-1} are the two characteristic peaks of CuI stretching.

FUTURE SCOPE:

- CuI Nanoparticles can be used as versatile heterogeneous catalysts for important organic transformations. As a proof of concept, CuI Nanoparticles were successfully applied as heterogeneous catalysts for the synthesis of secondary amines, amides and triazoles**.**
- The polymer stabilized CuI nanoparticles have also been applied as a catalyst for the electrochemical detection of formic acid.
- Copper (I) iodide (CuI) is a very efficient inorganic p-type material and has a potential application in polymer solar cells (PSCs).
- CuI Nanoparticles will be a novel promising hole transporting material for highly efficient and stable PSCs. So, in future we have planned to extend our work in constructing CuI Nanoparticles-based devices with

enhanced stability.

- The γ -CuI has potential applications in light emitting diodes due to a large excitation binding energy which causes a high intensity of violet emission. Copper nanoparticles have been used as a low-priced catalyst in industry and catalysis of many organic transformations.
- Thus field of nanoscience and notably the CuI Nanoparticle would have a sensible future. This shows the growth impact in Nanoscience field.

BIBLIOGRAPHY:

1. Kauffman, G. B.; Fang, L. Y. "Purification of Copper (I) Iodide" Inorganic Syntheses, 1983, volume 22, pages 101-103. ISBN 0-471-88887-7
2. Mohd Rafie Johan, Kok si wen, Norliza Hawari, Nurul Azri Khalisah Aznam, Synthesis and characterization of copper iodide and nanoparticles via chemical route, International Journal of Electrochemical Science,2012.
3. Nozomi Shionoiri, Tetsuya Sato, Yoshie Fujimori, Tsuruo Nakayama, Michiko Nemoto, Tadashi Matsunaga, Tsuyoshi Tanaka, Investigation of the antiviral properties of copper iodide nanoparticles against feline calicivirus, Journal of Bioscience and Bioengineering, May 2012, volume 113, Pages 580-586
4. Hammad R. Humud, Saba J. Kaden, Dawood Majed khudhair, Structural and optical properties of copper iodide nanoparticles synthesized by electro explosion wire, 2017.
5. Javad Safaei-Ghomi, Sahar Rohani, Abolfazl Ziarati, The XRD pattern of copper iodide nanoparticles, March 2012.
6. Sushmita, Monika Patel, Deepika thakur, Akhilesh K. Verma, Copper iodide nanoparticles: an efficient catalyst for the synthesis of alkynyl esters, 2023
7. Stefanos Mourdikoudis, Roger M. Pallares, and Nguyen T.K Thanh, Characterization techniques for nanoparticles: comparison and complementarity upon studying nanoparticle properties, Royal Society of Chemistry, 2018.
8. Ravi Sharma, D.P. Bisen, Usha Shukla and B.G. Sharma, X-ray

diffraction: a powerful method of characterizing nanomaterials, Recent Research in Science and Technology 2012, Pages 77-79, ISSN: 2076-5061.

9. Sathish Boddolla, Satyanarayana Thodeti, A review on Characterization techniques of Nanomaterials, International Journal of Engineering, Science and Mathematics, Vol. 7 Issue1, January 2018, ISSN: 2320-0294.
10. Siwach OP, Sen P. Synthesis and study of fluorescence properties of Cu nanoparticles. Journal of Nanoparticle Research 2008; 10:107-114.
11. Nilesh Patil, Rajveer Bhaskar, Vishal Vyavhare, Rahul Dhadge, Vaishnavi Khaire, Yogesh Patil, Overview on methods of synthesis of Nanoparticles, International Journal of Current Pharmaceutical Research, Vol 13, Issue2, 2021, ISSN: 0975-7066.
12. Namita Rajput, Methods of Preparation of Nanoparticles – A Review, International Journal of Advances in Engineering & Technology, Jan., 2015, ISSN: 22311963.
13. Sovan Lal Pal, Utpal Jana, P. K. Manna, G. P. Mohanta, R. Manavalan, Nanoparticle: An overview of preparation and characterization, Journal of Applied Pharmaceutical Science, 2011; 228-234
14. Manoranjan Kumar, Vinod Bhatt, Onkar S. Nayal, Sushila Sharma, Vishal Kumar Maheshwar S. Thakur, Neeraj Kumar, Rajaram Bal, Bikram Singh and Upendra Sharma, CuI nanoparticles as recyclable heterogeneous catalysts for C–N bond formation reactions, Journal of Catalysis Science and Technology, Issue 13, 2017.
15. Javad Safaei-Ghomi, Mohammad Ali Ghasemzadeh, Ahmad Kakavand-Qalenoe, CuI-nanoparticles-catalyzed one-pot synthesis of benzo[*b*]furans via three-component coupling of aldehydes, amines and

alkyne, Journal of Saudi Chemical Society, vol 20, Issue 5, 2016; 502-509.

16. Hong Tao Li & Li Xia Gu, Preparation and characterization of cuprous iodide nanoparticles, Inorganic chemistry, 2007; 85-89.
17. Zehra edis, Samir haj bloukh, Copper iodide nanoparticles and their antimicrobial activities, Journal of Nanomedicine & Biotherapeutic Discovery, 2020.
18. Safaei-Ghomi, Javad, Ziarati, Abolfazl, Teymuri, Raheleh, CuI Nanoparticles as New, Efficient and Reusable Catalyst for the One-pot Synthesis of 1,4-Dihydropyridines, Bulletin of Korean Chemical Society, Vol 33, Issue 8,2012; 2679-2682.
19. Zarrin Ghasemi, Salman Shojaeia and Aziz Shahrisaa, Copper iodide nanoparticles supported on magnetic amino methylpyridine functionalized cellulose: a new heterogeneous and recyclable nanomagnetic catalyst for facile access to N-sulfonyl amidines under solvent free conditions, Journal of Royal Society of Chemistry, 2016.
20. Yohei Takeda, Dulamjav Jamsransuren, Tomokazu Nagao, Yoko Fukui, Sachiko Matsuda, and Haruko Ogawa, Journal of Applied and Environmental Microbiology,2021.
21. K.M. Archana, Revathy Rajagopal, Veena Gayathri Krishnaswamy, and S. Aishwarya, Application of green synthesized copper iodide particles on cotton fabric-protective face mask material against COVID-19 pandemic, Journal of Materials Research and Technology, 2021.
22. Ao Liu, Huihui Zhu, Myung-Gil Kim, Junghwan Kim, Yong-Young Noh, Engineering Copper Iodide (CuI) for Multifunctional p-Type Transparent Semiconductors and Conductors, Journal of Advanced

Science, vol 8, Issue 14, 2021.

23. Revathy Rajagopal, Stella Maris College, Green Synthesis of Copper iodide nanoparticles using black soyabean seed extract and its anti-bacterial activity, National Conference on Nanomaterial Research,2014.
24. Dipranjan Laha, Debalina Bhattacharya, Arindam Pramanik, Chitta Ranjan Santra, Panchanan Pramanik and Parimal Karmakar, Evaluation of copper iodide and copper phosphate nanoparticles for their potential cytotoxic effect, Toxicology Research, 2012.
25. Ann Candice Fernandez, Archana KM, Revathy Rajagopal, Green synthesis, characterization, catalytic and antibacterial studies of copper iodide nanoparticles synthesized using Brassica oleracea var. capitata f. rubra extract, Chemical data collection, vol 29, 2020.
26. Jincheng Huang, Duyou Lua, Tanmay Mandal, Catalytic application of copper iodide nanoparticles in organic synthesis, International Journal for Rapid Communication of Synthetic Organic Chemistry Volume 51, Issue 13, 2021.
27. Hammad R Humud, Saba J Kadhem and Dawood Majed Khudhai, Structural and Optical Properties of Copper Iodide Nanoparticles Synthesized by Electro - Explosion of Wire, Journal of Chemical and Pharmaceutical Research, 2017, 31-36.
28. N O Alexeeva, S E Gango, N I Puchkov, V G Solovyev and A V Cvetkov, Electrical properties of copper iodide nanoparticles embedded into porous alumina matrix, Journal of Physics, International Conference Physics, 2017.
29. Fatemeh Ebrahimpour-Malamir, Tayebeh Hosseinnejad, Razieh Mirsafaei, Majid M. Heravi**,** Synthesis, characterization and

computational study of CuI nanoparticles immobilized on modified poly (styrene-co-maleic anhydride) as a green, efficient and recyclable heterogeneous catalyst in the synthesis of 1,4-disubstituted 1,2,3-triazoles via click reaction**,** Applied Organometallic chemistry Volume 32, Issue 1,2017.

EFFECT OF CADMIUM DOPING CONCENTRATION ON THE STRUCTURAL AND MORPHOLOGICAL PROPERTIES OF ZnO NANOPARTICLES

Project report submitted to the Department of Physics

ST. MARY'S COLLEGE (AUTONOMOUS)
THOOTHUKUDI
Affiliated to MANONMANIUM SUNDARANAR UNIVERSITY, TIRUNELVELI
In partial fulfillment of requirements for the award of
BACHELOR'S DEGREE IN PHYSICS
BY

A. EVANGELIN - 20AUPH05
M. MAHALAKSHMI - 20AUPH13
A. MARIA ANTONY BRISKILLA - 20AUPH14
S. MEENAKSHI - 20AUPH20
A. MELCIYA ANCILIN - 20AUPH21
R. RICZY CHILS - 20AUPH26

Under the guidance of

MS.A. LUCAS REXCELINE

DEPARTMENT OF PHYSICS
St. Mary's College (Autonomous), Thoothukudi-1
(Re-Accredited with "A+" grade)

(2022-2023)

CERTIFICATE

This is to certify that this project work entitled, "**EFFECT OF CADMIUM DOPING CONCENTRATION ON THE STRUCTURAL AND MORPHOLOGICAL PROPERTIES OF ZnO NANOPARTICLES**" is submitted to ST. MARY'S COLLEGE (AUTONOMOUS), THOOTHUKUDI in partial fulfilment for the award of Bachelor's Degree in Physics and is a record of work done during the year 2022-2023 by the following students.

A. EVANGELIN	**- 20AUPH05**
M. MAHALAKSHMI	**- 20AUPH13**
A. MARIA ANTONY BRISKILLA	**- 20AUPH14**
S. MEENAKSHI	**- 20AUPH20**
A. MELCIYA ANCILIN	**- 20AUPH21**
R. RICZY CHILS	**-20AUPH26**

A. Lucas Reuchine
GUIDE 3/4/23

HEAD OF THE DEPARTMENT
HEAD
Department of Physics,
St. Mary's College (Autonomous),
Thoothukudi - 628 001.

13/4/23
EXAMINER

PRINCIPAL
St. Mary's College (Autonomous)
Thoothukudi - 628 001.

DECLARATION

We hereby declare that the project entitled, "**EFFECT OF CADMIUM DOPING CONCENTRATION ON THE STRUCTURAL AND MORPHOLOGICAL PROPERTIES OF ZnO NANOPARTICLES**" submitted to St. Mary's College (Autonomous), Thoothukudi, affiliated to Manonmaniam Sundaranar University, for the Bachelor's Degree in Physics is our original work and that, it has not previously formed the basis for the award of any Degree, Diploma or similar title.

A. EVANGELIN - **20AUPH05**

M. MAHALAKSHMI - **20AUPH13**

A. MARIA ANTONY BRISKILLA - **20AUPH14**

S. MEENAKSHI - **20AUPH20**

A. MELCIYA ANCILIN - **20AUPH21**

R. RICZY CHILS - **20AUPH26**

Station: Thoothukudi

Date: 03.04.2023

ACKNOWLEDGEMENT

In the development of this project, thanks must flow outward as the sparks fly upward. Invaluable guidance without which, this project would not have seen the light of this day. A large number of people have devoted their time, energy and talent at our disposal and we salute them all.

First of all, we would like to thank God Almighty for his sunny disposition and skill in pulling everything together. We are infinitely indebted to our college principal **Dr. Sr. A.S.J. LUCIA ROSE M.Sc., M.Phil., Ph.D., PGDCA** for providing this opportunity and we are extremely thankful for all the help encouragement and invaluable moral support provided to us throughout the project work.

We wish to express our gratitude to our **Head of the department Dr.Sr. Jessie Fernando M. Sc., M.Phil., Ph. D.,** for her encouragement in carrying out this project work.

We are ineffably indebted to **Ms. A. Lucas Rexceline M.Sc., M.Ed., M.Phil., Associate Professor of Physics** for her conscientious guidance and encouragement to accomplish this project successfully.

We would like to extend our gratitude to department of Physics, St. Mary's College (Autonomous), Thoothukudi for providing us with Hot air oven and muffle furnace used for the preparation of nanoparticles.

We also thank the **MARIAN STAR CENTER**, for providing the latest equipment to carry on our project successfully, under the STAR COLLEGE SCHEME, sponsored by DBT, Chennai.

And also, we thank **Mr. VINCENT, St. JOSEPH'S COLLEGE, TRICHY** for carrying out the characterization studies and providing us with the result promptly.

We wish to accord our sincere gratitude to our non-teaching staff members who helped us to carry out our project work in the lab smoothly.

"A little progress each day adds up to big results."

We also thank our parents and friends from the depth of our hearts for their profound encouragement and timely help.

ABSTRACT

Over recent years, increasing attention has been focused on the production of novel nanoscale materials. The metal oxides are extremely important technological materials for use in electronic and photonic devices and as catalysts in chemical industries. In the present investigation, sol gel method is used to prepare pure, and cadmium doped ZnO nanoparticles with two different concentrations. Their structural and morphological properties are studied from XRD pattern. The absence of impurity peaks reveals that the Cd doped ZnO nanoparticles to exhibit high crystalline quality. As Cd is incorporated, the size of the particle decreases which indicates the crystallinity of the sample can be improved by doping. From SEM analysis, it is concluded that the formation of nano rods. As Cd is incorporated, the shape of the powder sample exhibit spherical shape.

CONTENT PAGE NO

CHAPTER 1

INTRODUCTION

Over recent years, increasing attention has been focused on the production of novel nanoscale materials. The metal oxides are extremely important technological materials for use in electronic and photonic devices and as catalysts in chemical industries. Nanotechnology is now considered to be a proven state-of-the-art technology with numerous branches embedded in industrial fields such as chemical, pharmaceutical, mechanical, and food processing industries. Nanotechnology also plays an interesting role in the areas of computing, power generation, optics, drug delivery, and environmental sciences. One of the most commonly used transition metal oxide for a wide range of application is zinc oxide. Zinc oxide nanoparticles are very prosperous metal with small dimension, high specific area and good chemical activity. Due to these advantages, Zinc oxide nanoparticles have extensively attracted interests in many applications especially in catalysts, gas sensors and medical field. In this present work, sol gel method is used to produce pure and cadmium doped Zinc oxide nanoparticles and the effect of cadmium concentration on their structural properties are studied.

1.1. NANO TECHNOLOGY

Nanotechnology is the latest field that manipulates matter on an atomic or molecular scale. The earliest widespread description of nanotechnology referred to the particular technological goal of precisely manipulating atoms and molecules for fabrication of macroscale products, also now referred to as molecular nanotechnology. Nanoscience is the study of structures and molecules on the scales of nanometers ranging between 1 and 100 nm, and the technology that utilizes it in practical applications such as electronic devices, gas sensors etc. is called nanotechnology [1].

1.2. NANOPARTICLE

Idealized model of a crystalline nanoparticle of platinum, about 2 nm in diameter, showing individual atoms. Nanoparticles occur widely in nature and are objects of study in many sciences such as chemistry, physics, geology, and biology. Being at the transition between bulk materials a nanoparticle or ultrafine particle is usually

defined as a particle of matter that is between 1 and 100 nanometres (nm) in diameter. **[2,3]** The term is sometimes used for larger particles, up to 500 nm, or fibers and tubes that are less than 100 nm in only two directions.**[4]** At the lowest range, metal particles smaller than 1 nm are usually called atom clusters instead.

Nanoparticles are usually distinguished from microparticles (1-1000 μm), "fine particles" (sized between 100 and 2500 nm), and "coarse particles" (ranging from 2500 to 10,000 nm), because their smaller size drives very different physical or chemical properties, like colloidal properties and ultrafast optical effects**[5]** or electric properties. Being more subject to the Brownian motion, they usually do not sediment, like colloidal particles that conversely are usually understood to range from 1 to 1000 nm. Being much smaller than the wavelengths of visible light (400-700 nm), nanoparticles cannot be seen with ordinary optical microscope, requiring the use of electron microscopes or microscopes with laser. For the same reason, dispersions of nanoparticles in transparent media can be transparent,**[6]** whereas suspensions of larger particles usually scatter some or all visible light incident on them. Nanoparticles also easily pass through common filters, such as common ceramic candles,**[7]** so that separation from liquids requires special nanofiltration techniques.

The properties of nanoparticles often differ markedly from those of larger particles of the same substance. Since the typical diameter of an atom is between 0.15 and 0.6 nm, a large fraction of the nanoparticle's material lies within a few atomic diameters of its surface. Therefore, the properties of that surface layer may dominate over those of the bulk material. This effect is particularly strong for nanoparticles dispersed in a medium of different composition since the interactions between the two materials at their interface also becomes significant. **[8]**

Being at the transition between bulk materials and atomic or molecular structures, they often exhibit phenomena that are not observed at either scale. They are an important component of atmospheric pollution, and key ingredients in many industrialized products such as paints, plastic, metals, ceramics and magnetic products. The production of nanoparticles with specific properties is a branch of nanotechnology.

In general, the small size of nanoparticles leads to a lower concentration of point defects compared to their bulk counterparts,**[9]** but they do support a variety

of dislocations that can be visualized using high-resolution electron microscopes.**[10]** However, nanoparticles exhibit different dislocation mechanics, which, together with their unique surface structures, results in mechanical properties that are different from the bulk material. **[11,12,13]**

Non-spherical nanoparticles (e.g., prisms, cubes, rods etc.) exhibit shape-dependent and size-dependent (both chemical and physical) properties (anisotropy). **[14,15].** Non-spherical nanoparticles of gold (Au), silver (Ag), and platinum (Pt) due to their fascinating optical properties are finding diverse applications. Non-spherical geometries of nanoprisms give rise to high effective cross-sections and deeper colors of the colloidal solutions. The possibility of shifting the resonance wavelengths by tuning the particle geometry allows using them in the fields of molecular labeling, biomolecular assays, trace metal detection, or nanotechnical applications. Anisotropic nanoparticles display a specific absorption behavior and stochastic particle orientation under unpolarized light, showing a distinct resonance mode for each excitable axis. **[16]**

CHAPTER 2

LITERATURE REVIEW

Vinodkumar Etacheri et.al. (2012). Magnesium-doped ZnO (ZMO) nanoparticles were synthesized through an oxalate coprecipitation method. Crystallization of ZMO upon thermal decomposition of the oxalate precursors was investigated using differential scanning calorimetry (DSC) and X-ray diffraction (XRD) techniques. XRD studies point toward a significant c-axis compression and reduced crystallite sizes for ZMO samples in contrast to undoped ZnO, which was further confirmed by HRSEM studies. X-ray photoelectron spectroscopy (XPS), UV/vis spectroscopy and photoluminescence (PL) spectroscopy were employed to establish the electronic and optical properties of these nanoparticles. (XPS) studies confirmed the substitution of Zn2+ by Mg2+, crystallization of MgO secondary phase, and increased Zn−O bond strengths in Mg-doped ZnO samples. Textural properties of these ZMO samples obtained at various calcination temperatures were superior in comparison to the undoped ZnO. In addition to this, ZMO samples exhibited a blue-shift in the near band edge photoluminescence (PL) emission, decrease of PL intensities and superior sunlight-induced photocatalytic decomposition of methylene blue in contrast to undoped ZnO. The most active photocatalyst 0.1-MgZnO obtained after calcination at 600 °C showed a 2-fold increase in photocatalytic activity compared to the undoped ZnO. Band gap widening, superior textural properties and efficient electron−hole separation were identified as the factors responsible for the enhanced sunlight-driven photocatalytic activities of Mg-doped ZnO nanoparticles. **[17]**

Viswanatha et al. (2012). Mg-doped ZnO have considerable interests owing to their unique optical, thermal and structural properties. ZnO and Mg doped ZnO nanoparticles with different doping concentration were prepared by precipitation method. The effect of Mg doping on the crystal structure, morphology and optical properties of the nanoparticles was also investigated. In this paper, we report the Synthesis of Mg-doped ZnO nanoparticles successfully with diameters ranging from 60 to 90nm via precipitation method. The surface morphology of synthesized material was investigated by using scanning electron microscope (SEM). The structure and phases of Mg-ZnO were analyzed by powder X-ray diffraction (XRD)

method and the optical properties were measured by using UV-V's spectrophotometer and photoluminescence spectroscopy. **[18]**

Pradeev Raj et al. (2018). In this research, a facile co-precipitation method was used to synthesize pure and Mg-doped ZnO nanoparticles (NPs). The structure, morphology, chemical composition, and optical and antibacterial activity of the synthesized nanoparticles (NPs) were studied with respect to pure and Mg-doped ZnO concentrations (0–7.5 molar (M) %). X-ray diffraction pattern confirmed the presence of crystalline, hexagonal wurtzite phase of ZnO. Scanning electron microscope (SEM) images revealed that pure and Mg-doped ZnO NPs were in the nanoscale regime with hexagonal crystalline morphology around 30–110 nm. Optical characterization of the sample revealed that the band gap energy (Eg) decreased from 3.36 to 3.04 eV with an increase in Mg2+ doping concentration. Optical absorption spectrum of ZnO redshifted as the Mg concentration varied from 2.5 to 7.5 M. Photoluminescence (PL) spectra showed UV emission peak around 400 nm. Enhanced visible emission between 430 and 600 nm with Mg2+ doping indicated the defect density in ZnO by occupying Zn2+ vacancies with Mg2+ ions. Photocatalytic studies revealed that 7.5% Mg-doped ZnO NPs exhibited maximum degradation (78%) for Rhodamine B (RhB) dye under UV-Vis irradiation. Antibacterial studies were conducted using Gram-positive and Gram-negative bacteria. The results demonstrated that doping with Mg ions inside the ZnO matrix had enhanced the antibacterial activity against all types of bacteria and its performance was improved with successive increment in Mg ion concentration inside ZnO NPs. **[19]**

Samuel Adesoye et.al. (2022). Semiconductors have great potential as surface-enhanced Raman scattering (SERS) substrates due to their excellent physiochemical properties. However, they provide low signal enhancements relative to their plasmonic counterparts, which necessitates innovation in their synthesis and application. Substitutional atomic doping is proposed to improve SERS enhancement by controlling electronic properties, such as the band gap. In this work, zinc oxide (ZnO) nanoparticles were synthesized by co-precipitation and doped with magnesium (Mg) at concentrations ranging from 2–10%. Nanoparticle morphology and size were obtained by scanning electron microscopy (SEM). Elemental composition and chemical states were determined using X-ray photoelectron spectroscopy (XPS). Optical properties were obtained with a UV-vis spectrophotometer, while a Raman spectrometer was used to acquire Raman signal

enhancements. Stability was assessed by UV-vis spectroscopy, while cytotoxicity was evaluated by the 3-(4,5-dimethylthiazol-2-yl)-2,5-diphenyltetrazolium bromide (MTT) assay. The results showed that the absorption edge of Mg-doped ZnO nanoparticles was red-shifted compared to pure ZnO nanoparticles. The band gap decreased (3.3–3.01 eV) with increasing Mg doping, while the highest Raman enhancement was observed at 2% doping. No significant cytotoxic effects were observed at low concentrations (3–12 μg/mL). Overall, this study provides evidence for the tunability of ZnO substrates and may serve as a platform for applications in molecular biosensing. **[20]**

Kangathara et al. (2022). In this study, we reported the synthesis of pure ZnO and Mg-doped ZnO (Mg-ZnO) nanoparticles by simple co-precipitation method and studied the ethanol sensing activity of the synthesized nanostructures. XRD analysis illustrates that the synthesized ZnO and Mg-doped ZnO nanoparticles (NPs) possess hexagonal wurtzite structure and the average crystallite size is calculated to be 29 nm and 33 nm, respectively. The FT-IR spectra of pure and Mg-doped ZnO NPs confirm that the presence of bands appeared near 400 cm-1 for Zn-O and the bands at 622 cm-1 can be attributed to Mg-O stretching modes. The band gap energy estimated from the absorption spectra for ZnO and Mg-ZnO NPs, respectively, at 3.26 eV and 3.32 eV, displays the considerable optical property. Further, we observed that the UV-Vis spectroscopic data exhibits high absorbance in the UV range for the prepared samples. The SEM images clearly display the needle-like morphology of the synthesized samples. Dynamic light scattering analysis shows average particle size of 110 nm. The ethanol sensing measurements were carried out with 100 ppm concentration, and the linear responses from ZnO and Mg-ZnO NPs-based sensors are detected in the working temperature of 350° C. The obtained results demonstrated that the synthesized Mg-ZnO nanostructures have improved conductivity with larger active surface area for the most promising application in the ethanol sensing activity. **[21]**

Charlesbaba et al. (2016). Pure and cadmium (Cd2+) doped zinc oxide (ZnO) were prepared by programmable microcontroller assisted spin coating unit using organometallic precursor. The pure and doped ZnO thin films were deposited on well glass substrate at 1500 rpm under alkaline condition. 400°C sintered films were characterized for their structural, morphological, optical and electrical properties using X-ray diffraction method, scanning electron microscopy, UV-visible absorption method and DC measurements respectively. Hexagonal wurtzite phase

with multiple faceted growths was witnessed for pristine film. Without alteration in the phase but dopant induced small variation in the position of prominent peaks were shown by Cd doped ZnO thin films. The dopant induced island growth and increasing roughness were clearly unveiled via SEM analysis. Variation in the structure and shape of the optical absorption peak reveal the varying crystallite size in accordance with dopant concentration. The electrical measurements showed that the doping process enhance the conducting property of the films. On comparison 6% Cd doped ZnO films exhibit good conductivity than other films. **[22]**

Arun Jose et al (2013). Cadmium doped Zinc oxide nanopowder was synthesized by simple and inexpensive combustion technique using zinc nitrate and glycine. We found that in the combustion process nitrate ions acts as an oxidant. The powder XRD analysis confirms the crystallinity of the synthesized sample with crystallite size of 50nm for the various doping concentration of 1%,3%,5%. The absorbance near UV region decreases with increase in dopant concentration., the PL intensity increases with increase in Cd dopant. **[23]**

Poornima (2019) . Nanocrystalline Zinc Oxide and Cadmium doped Zinc Oxide were prepared successfully at room temperature with various dopant percentage of cadmium. The as prepared analyzed samples were coated on a glass substrate by dip coating method for various time intervals The as deposited undoped and doped Zinc Oxide films were analyzed by XRD, FTIR, UV-Vis spectrometry, SEM and cyclic voltometry-ray diffraction reveals the standard Zinc Oxide crystal structure. FTIR confirm the metal oxide bond in the molecular structure. Optical absorption analysis of the samples shows red shift in the absorption band spectrum depending on dopant percentage. SEM image indicates the spherical structure. **[24]**

Jianfeng Li et al (2019). In this work, electron transport layers (ETLs)with high charge transfer ability were fabricated by doping ZnO nanoparticles with different concentrations of cadmium. The performance for an inverted polymer solar cell based on PTB7-Th: PC71BM with 5% cadmium doping of zinc oxide nanoparticles (CZO) ETL is better than pure ZnO, which can enhance the short-circuit current (JSC), from 16.30 mA/cm2 to 17.15mA/cm2, the fill factor (FF) from 64.45% to 69.38%, power conversion efficiency (PCE) from 8.09% to 9.28%. It's consequence of performance stems from curbing interfacial charge recombination and effective charge extraction. Meanwhile, taking a series of characterization methods, such as atomic force microscopy (AFM), the space charge limited current (SCLC), transmittance, the charge dissociation probabilities (P (E, T)), photo-electrochemical

impedance spectroscopy (EIS). The results indicate that the electrical conductivity and transmittance of the films are improved by incorporation of Cd in the ZnO film, restrained surface charge recombination and enhanced the electron-transport capability. Therefore, the ETL of Cd-doped will be an ideal candidate for future optoelectronic devices. **[25]**

Balamurugan et al (2019). The Cd: ZnO nanoparticles were effectively prepared through simple chemical method by varying the doping (5,10,15,20%) concentration. The obtained pure and Cd doped ZnO nanoparticles were characterized to know their structural, morphological, optical properties. A cubic crystal structure was observed from the XRD and their crystallite sizes were approximately in around 15 nm. A spherical shaped morphology was observed from the SEM analysis. A blue-shifted optical absorption was observed from UV spectrum and their calculated bandgap energy value was approximately 3.6 eV. An improved emission nature was observed from the PL emission spectrum. **[26]**

Yu-Chih et al. (2012). Investigates the effect of Ti content on the optical and structural properties of the Ti-doped ZnO (TixZn1-xO) nanoparticles by x-ray diffraction, scanning electron microscopy, photoluminescence and Raman scattering measurements. A dependence of luminescent properties and crystal structure upon Ti content has been found. The band-edge-luminescence (BEL) intensity of Ti0.10Zn0.90O at room temperature as nearly 1.7 times higher than that of ZnO. The enhanced BEL intensity is attributed to a decrease in the oxygen-vacancy density. However, the lower BEL intensity of Ti0.15Zn0.85O than Ti0.10Zn0.90O is attributed to an increase in the probability of nonradiative recombination. In addition, the intensity of the x-ray diffraction peaks remarkably decreases with increasing Ti content, suggesting weakened crystallinity. **[27]**

Raji et al. (2018). Studied the absorption bands of ZnO, studied on the experiment preparation of Ti – doped ZnO (TixZn1-xO x= 0.00, 0.05, 0.10, 0.15) nanoparticles have been synthesized through co – precipitation approach. X-ray diffraction (XRD), scanning electron Microscopy (SEM), photoluminescence (PL), UV-Visible spectroscopy, and Vibrating Sample Magnetometer (VSM) have been used to characterize the samples. X-Ray Diffraction (XRD) analysis manifested the hexagonal wurtzite structure. The crystallite size decreased from 37 nm to 29 nm as dopant concentration is increased. Fourier transform infrared analysis show with few within the intensities. SEM investigation showed the irregular shape and agglomeration of the particles. Ti, Zn, and O composition were determined From

EDX analysis and confirmed the purity of the samples.PL spectra showed a near band edge Emission and visible emission. Vibrating sample magnetometer (VSM) demonstrated pure and doped samples exhibited ferromagnetism behavior at room temperature. **[28]**

Darmadi et al. (2020). In this study, we used the co-precipitation method to synthesize Ti-doped ZnO nanoparticles having different Ti contents. We then used energy dispersive X-ray spectroscopy to perform an elemental analysis, which revealed that the Ti content varied in its atomic Percentages from 5 at. %, 7 at. %, and 12 at. % to 16 at.%. We characterized the structural properties of the prepared samples using X-ray diffraction (XRD) spectroscopy and found Ti-Doped ZnO to have an anatase structure in which the lattice parameters a = b and c decrease from 3.251 and 5.213 Å to 3.254 and 5.203 Å, respectively, when the Ti content increased from 5 at. % to 16 at.%. We also found the grain size of Fe-doped TiO2 to decrease from 12 nm to 10 nm with increasing Ti content. We characterized the molecular vibration of the samples using Fourier transform–infrared spectroscopy (FT-IR) and the optical properties using UV-Vis diffuse reflectance spectroscopy. The results show the band-gap energy of Ti-doped ZnOto decrease from 3.20 eV to 3.12 eV. We tested the photocatalytic activity of Ti-doped ZnO in the degradation of methylene blue from the aqueous solution under UV light irradiation and found the photo catalyst Ti-doped ZnO to have good degradation ability, with a degradation Percentage of approximately 80%. **[29]**

Oratai jongprateep et al. (2018). On the experiment ZnO and TiO2 have been widely accepted as prominent photocatalysts. Enhancement of their photocatalytic activities can be achieved through particle refinement and doping. Solution combustion technique is a simple and cost-effective method capable of producing fine ceramic powders with homogeneous chemical compositions. It is, therefore, employed in this research project as the technique to synthesize nanometer-sized Ti-doped ZnO powders.

The research also aimed at examining a relationship among doping contents, chemical Composition, particle sizes, and photocatalytic performance of the synthesized powder. Compositional analysis revealed that the solubility limit of Ti in zinc oxide was within the range of 3 at% Ti. Within the solubility limit, photocatalytic activity was enhanced with the titanium doping. Reduced photocatalytic performance, however, was observed in the powders with titanium contents beyond the solubility limit. The results also indicated that doping

concentration did not have a significant effect on particle size and Morphology. Equiaxial particles, with the average particle sizes ranging from 46.4 to 48.4 Nm, were observed from the SEM micrographs. **[30]**

Vignesh et al. (2017). This study the Titanium doped Zinc oxide Nanoparticles were successfully synthesized by exposing microwave for 3min with 800W power. 1 mole of Ti concentration was doped into ZnO. Detailed crystal and local atomic structure of synthesized samples were characterized via X-ray Diffraction. Obtained Ti doped ZnO nanoparticles degraded with increasing Ti content. The grain size of the Ti doped ZnO is also determined. These Studies clearly suggest that microwave synthesis make fast and homogeneous reactions, to synthesis highly crystalline nano sized Ti doped ZnO nanoparticles. Solar cell is one of the best applications in future. **[31]**

Zhan Hong ma et al. (2020). Pure and Ni-doped ZnO nanorod array films were prepared by the hydrothermal method. The effects of Ni doping on the phase composition, microstructure, and optical and electro-chemical properties of ZnO were investigated. The main crystalline phase of the powders before and after Ni doping is wurtzite ZnO. The luminescent peaks are significantly reduced after Ni doping. The light transmission and is the strongest when the doping concentration is 2 %. The light absorption spectrum confirms that the band gap decreased first and then decreased with the increase of Ni2+ doping concentration. According to the M–S (Mott - Schottky) plots, the Ni-doped ZnO is an n-type semiconductor. The current density initially increases with the increased Ni doping amount, and then decreases. First-principles calculation results of nickel-doped zinc oxide show that the energy level of impurities is formed after nickel ions replace zinc ions, which causes the con-duction band is shifted down and the band gap is reduced. The impurity energy level causes a slight upward shift in the valence band, which increases the band gap. The calculated results are consistent with the experimental results. **[32]**

Madhava et.al (2018). Weak ferromagnetic behavior was obtained in a systematic way at room temperature by doping of ZnO with nickel (Zn1-xNixO, where x = 0.00, 0.05, 0.15 and 0.20). The obtained results were correlated with conductivity and impedance studies. Diamagnetic to ferromagnetic change was observed with increased concentration of Nickel. X-ray diffraction analysis confirmed wurtzite ZnO structure of prepared nanopowders while microstrain was increased with nickel concentration. Incorporation of nickel in ZnO structure was confirmed using EDAX Analysis, while FTIR spectroscopy provided further information on functional

groups. Transmission electron Microscopy images showed that the particle sizes are in the range of 12–20 nm, and scanning electron microscopy analyses that grain size decreases with increase in nickel concentration. Photo luminescence studies Confirmed the presence of VO And Zni Defects in the prepared samples. It was concluded that the defect induced Strain, grain boundaries and lower particle sizes are the reasons for weak ferromagnetic behavior of the Investigated samples. **[33]**

Zahra Manzoor et al. (2020). Metal organic chemical vapor deposition (MOCVD) growth of nickel-doped zinc oxide (Ni-doped ZnO) thin films on sapphire was investigated. The structural and optical properties were studied. The samples were grown at two substrate temperatures (i.e., 450 and 550 °C) and at three chamber pressures (22, 30 and 100 Torr). The Ni-doped ZnO samples showed the (002) hexagonal crystal structure with signs of secondary phases in X-ray diffraction (XRD) measurements. however, different XRD peak intensities were observed for these samples at different growth conditions with the same Ni flow rate injection to the reaction chamber. The samples grown at different growth conditions had different optical absorption spectra. Results prove that the growth at a low pressure and temperatures close to the decomposition temperature of the precursors resulted in an optimum dopant incorporation, sharp absorption band edges, and good Crystalline quality. **[34]**

Mary et al. (2022). On the experiment ZnO and TiO2 have been widely accepted as prominent photocatalysts. Enhancement of their photocatalytic activities can be achieved through particle refinement and doping. Solution combustion technique is a simple and cost-effective method capable of producing fine ceramic powders with homogeneous chemical compositions. It is, therefore, employed in this research project as the technique to synthesize nanometer-sized Ti-doped ZnO powders.

The research also aimed at examining a relationship among doping contents, chemical Composition, particle sizes, and photocatalytic performance of the synthesized powder. Compositional analysis revealed that the solubility limit of Ti in zinc oxide was within the range of 3 at% Ti. Within the solubility limit, photocatalytic activity was enhanced with the titanium doping. Reduced photocatalytic performance, however, was observed in the powders with titanium contents beyond the solubility limit. The results also Indicated that doping concentration did not have a significant effect on particle size and Morphology. Equiaxial particles, with the average particle sizes ranging from 46.4 to 48.4 Nm, were observed from the SEM micrograph. **[35]**

Fernanda et al. (2015). We report for the first time a rapid preparation of Zn12xCoxNixO nanoparticles via a versatile and environmentally friendly route, microwave-assisted hydrothermal (MAH) method. The Co, Ni co-doped ZnO nanoparticles present an effect on photoluminescence and electrochemical properties, exhibiting excellent electrocatalytic performance compared to undoped ZnO sample. Photoluminescence spectroscopy measurements indicated the reduction of the green–orange–red visible emission region after adding Co and Ni ions, revealing the formation of alternative pathways for the generated recombination. The presence of these metallic ions into ZnO creates different defects, contributing to a local structural Disorder, as revealed by Raman spectra. Electrochemical experiments revealed that the electrocatalytic oxidation of dopamine on ZnO attached to multi-walled carbon nanotubes improved significantly in the Co, Ni co-doped ZnO samples when compared to pure ZnO.**[36]**

Albel nibret et al. (2015). Report the synthesis of CrN co-doped ZnO for the first time. Zinc oxide (ZnO) nanoparticles were synthesized by direct precipitation method via the reaction between zinc nitrate [Zn (NO3)2 .6H2O] and ammonium carbonate [(NH4)2CO3] in aqueous solutions with proper concentration. Modified Photocatalysts were synthesized by the incipient wetness impregnation method (chromium-doped ZnO) and by solid state reactions using ZnO and urea as precursors (nitrogen-doped ZnO). Chromium-nitrogen co-doped ZnO nanomaterials were prepared from the already prepared N-doped ZnO nanomaterials via one step impregnation method.The as-synthesized photocatalysts were investigated by XRD, BET, SEM-EDX, FTIR, and UV–Vis Techniques Phegradation of thymol blue using as-synthesized photocatalysts was studied under Visible as well as UV irradiations. Highest photocatalytic degradation efficiency of chromium-nitrogen co-doped Zinc oxide could be attributed to the lower rate of recombination of the photo-generated electrons and holes as Well as to its lower band gap energy as the result of the co-doping. Photocatalytic degradation is found to follow Pseudo first order kinetics. **[37]**

Alexei Alexandrov et al. (2020). Colloidal quantum dots and other semiconductor nanocrystals are essential components of next-generation lighting and display devices. Due to their easily tunable and narrow emission band and near unity fluorescence quantum yield, they allow cost-efficient fabrication of bright, pure-color and wide-gamut light emitting diodes (LEDs) and displays. A critical improvement in the quantum dot LED (QLED) technology was achieved when zinc

oxide nanoparticles (NPs) were first introduced as an electron transport layer (ETL) material, which tremendously enhanced the device brightness and current efficiency due to the high mobility of electrons in ZnO and favorable alignment of its energy Bands. During the next decade, the strategy of ZnO NP doping allowed the fabrication of QLEDs with a brightness of about 200000cd/m2 and current efficiency over 60cd/A. On the other hand, the known ZnO doping approaches rely on a very fine tuning of the energy levels of the ZnO NP conduction band minimum hence, selection of the appropriate dopant that would ensure the best device characteristics is often ambiguous. Here we address this problem via detailed comparison of QLEDs whose ETLs are Formed by a set of ZnO NPs doped with Al, Ga, Mg, or Li. Although magnesium-doped ZnO NPs are the most common ETL material used in recently designed QLEDs, our experiments have shown that Their aluminum-doped counterparts ensure better device performance in terms of brightness, current Efficiency and turn-on voltage. These findings allow us to suggest ZnO NPs doped with Al as the best ETL material to be used in future QLEDS. **[38]**

Paul Chalkar et al. (2012). Thin films of germanium-doped zinc oxide have been deposited by atomic layer deposition. The zinc Oxide matrix was grown from cyclic pulses of diethylzinc and water vapour over the temperature range of 100–350ubstrate temperature. Tetramethoxy germanium (IV) was employed as a novel Germanium-doping source, which could be incorporated up to 17 at%. At 2.1 at% germanium doping at a deposition temperature of 250C, the maximum carrier concentration of 2.14×10^20 cm3 coincides with a carrier mobility of approximately 5 cm2 V1 s1. No evidence for the formation of nanometre-Scale germanium clustering or segregation was observed in the X-ray diffraction patterns or high-Resolution transmission electron micrographs of these films. The near band edge photoluminescence Shifts to higher energy with increasing germanium incorporation either by the Burstein–Moss Mechanism or by alloy formation. **[39]**

CHAPTER 3

MATERIAL IMPORTANCE

3.1. Aim of the present work

In the present investigation, sol gel method is used to prepare pure and cadmium doped ZnO nanoparticles with two different concentrations. Their structural and morphological properties are studied using the following tools:

- To synthesis pure and cd(cadmium) doped ZnO nanoparticles by sol gel process
- To determine the size of the pure and cd(cadmium) doped ZnO nanoparticles using XRD method
- To study the morphology of the pure and cd (cadmium) doped ZnO nanoparticles through SEM analysis

3.2. Material importance of ZnO

Wurtzite ZnO has a hexagonal structure (space group C6mc) with lattice parameters a= 0.3296 and c= 0.52065 nm. The structure of ZnO can be simply described as a number of alternating planes composed of tetrahedrally coordinated O2- and Zn2+ ions, stacked alternately along c-axis as shown in Figure 3.1**[40].** The tetrahedral coordination in ZnO results in non-central symmetric structure and consequently piezoelectricity. More important characteristic of ZnO is its polar surfaces. The most common polar surface is the basal plane. The oppositely charged ions produce positively charged Zn-(0001) and negatively charged O-(000-1) surfaces resulted in a normal dipole moment and spontaneous polarization along the c-axis with a divergence in surface energy. To maintain a stable structure, the polar surfaces generally have facets or exhibit massive surface reconstructions, but ZnO± (0001) are exceptions: they are atomically flat, stable and without reconstruction.**[41]**

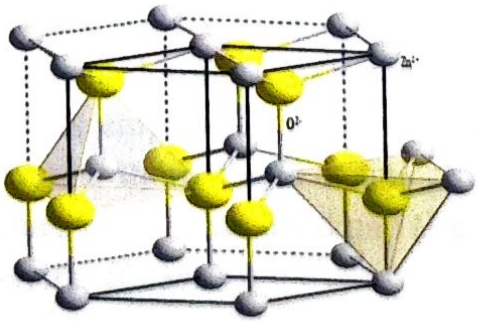

Figure 3. 1: Wurtzite structure of ZnO. [40]

Efforts to understand the superior stability of the ZnO± (0001) polar surfaces are at the forefront of research in today's surface physics. [55,56]. The other two most commonly observed facets for ZnO are {2-1-10} and {01-10}, which have non-polar surfaces and lower energy than the {0001} facets.

3.3. Applications of ZnO

Zinc oxide has diverse properties, both physical and chemical. It is widely used in many areas. ZnO plays an important role in a wide range of applications, from pharmaceuticals to agriculture, tyres to ceramics, and from paints to chemicals **[42]**.

- ZnO nanoparticles play some potential role in the CNS (central nervous system) and perhaps during development processes of diseases through mediating neuronal excitability or even release of neurotransmitters. Some studies have indicated that ZnO affected functions of different cells or tissues, biocompatibility, and neural tissue **[43]**.
- Zinc oxide nanoparticles have prospective potential to boost the yield and growth of food crops. Seeds were treated with different concentrations of zinc oxide nanoparticles enhanced seed germination, seedling vigor, and plant growth and these zinc oxide nanoparticles also proved to be effective in increasing stem and root growth in seeds **[44]**.
- Global production of zinc oxide amounts to about 105 tons per year, and a major portion is consumed by the rubber industry to manufacture various different cross-linked rubber products **[45]**.
- Due to its antibacterial, disinfecting and drying properties **[46,47]**, zinc oxide is widely used in the production of various kinds of medicines. It was formerly used as an orally administered medicine for epilepsy, and later for diarrhoea.
- ZnO nanoparticles are widely used to fabricate efficient gas sensors for the detection of varies hazardous and toxic gases.
- ZnO nanoparticles are employed as in chemical sensors due to their extensive range of stability under thermal and chemical variations.
- Its wurtzite structure has a wide band gap (Eg =3.37eV at 300K) and a large exciton binding energy(60MeV).

- ZnO has relatively higher and stable exciton binding energy of 60 MeV at 300K, almost three times larger than its competitor GaN which has an exciton binding energy of 25MeV.
- ZnO is a well-known II-VI compound semiconductor metal oxide due to its attractive physical and chemical properties.
- ZnO is widely applied for making photocatalysts, LED, gas sensors, ultraviolet lasers, photodetectors, solar cells.

3.4. Properties of ZnO

Table 3.1. Properties of ZnO

Molecular formula	ZnO
Molar mass	81,408 g/mol
Appearance	White solid
Density	5.606 g/cm^3
Melting point	1974°C
Boiling point	2360°C
Solubility	0.16 mg/100mol
Band gap	3.3eV

ZnO is a wide bandgap n –type semiconductor with an energy gap of 3.37eV which has been considered as a promising materials for optical, electronic and catalytic applications. Some of the important properties of ZnO are shown in table 3.1.

CHAPTER 4

Preparation of Pure and Cd doped ZnO nanoparticles

4.1. Introduction

The conventional approach for synthesis of nanoparticles involves chemical or physical attrition from bulk into objects of desired sizes and shapes and is referred as the "top down approach". Inverse to the top-down approach is a process universal in nature, involving the assembly of materials from molecular levels to form micro or macro sized shapes and structures, often referred as "Bottom up" process or "self assembly".

4.2. Sol Gel process

The sol–gel method was first described by the chemist Edelman **[48]** in the mid-nineteenth century. The soil is a colloidal suspension of oligomers ("oligomer= monomer molecular complex" whose diameter is several nanometers). Thereafter, this "soil" may be developed by chemical reactions, i.e. polycondensation or polyesterifcation, forming alcohol molecules in the bridges until gel formation. This freezing process offers many advantages for producing large materials with homogeneity and purity at lower temperatures than conventional methods. Thus, the gel obtained is subjected to the drying process, and the resulting product is transformed into xerogel, followed by a heat treatment that will eventually form powder **[49,50]**. The sol–gel method does not involve melting or sintering powders to produce ceramic but uses a solution containing reactive precursors such as alkoxides or metal salts. The precursors for the preparation of a colloid consist of a metal or metalloid element surrounded by various ligands. Metal alkoxides (R-O-M) are similar to alcohols (ROH) with a metal atom M, replacing hydrogen H in the hydroxyl group. They are the class of chemical precursors most commonly used in sol–gel synthesis because they are subject to hydrolysis depending on the amount of water and the catalyst present.

4.3. Material preparation

In this present work, pure ZnO nanoparticles are prepared and doped with cadmium at two different concentrations such as 0.01M and 0.03M by sol gel method. This method is suitable to control the size of the oxide nanoparticles.

4.3.1. Synthesis of pure ZnO nanoparticles

In the present work, 1M of $ZnCl_2$ is dissolved in 100ml of distilled water. The beaker is washed well with ethanol. In another beaker 1M of NaOH is dissolved in 100ml of distilled water, this solution is mixed with the solution of $ZnCl_2$ beaker by magnetic stirrer and stirred thoroughly for 3 hours, 50ml of ethanol and 50ml of distilled water is added again and stirred for another 30 minutes. The beaker is kept undisturbed for an hour. The sample is washed with ethanol and water five times. The sample obtained is white in colour and is filtered, the filtered sample heated in hot air oven at 150°C for 5hours, the dried sample is kept in the muffle furnace at 650°C for 5hours, the precipitate thus obtained is finely powered. Thus, the nanoparticle of pure ZnO is obtained.

4.3.2. Synthesis of cd doped ZnO nanoparticles

In the present work, 1M of $ZnCl_2$ is dissolved in 100ml of distilled water. The beaker is washed well with ethanol. In another beaker 1M of NaOH is dissolved in 100ml of distilled water, this solution is mixed with the solution of $ZnCl_2$ beaker by magnetic stirrer and stirred thoroughly for 1hour.In another beaker 0.01M % of cadmium acetate is dissolved in 100ml of distilled water. This solution is added slowly to the zinc chloride and NaOH solution. Wash the solution with ethanol and distilled water five times. The sample obtained is white in colour and is filtered, the filtered sample heated in hot air oven at 150°C for 5hours, the dried sample is kept in the muffle furnace at 650°C for 5 hours, the precipitate thus obtained is finely powered. Thus, the nanoparticle of 0.01M% Cd doped ZnO nanoparticles are obtained. In the same way, as explained above 0.03M% of Cd doped ZnO nanoparticles are obtained.

CHAPTER 5

CHARACTERIZATION TECHNIQUES

5.1. Introduction

The nanostructures can be characterized using various techniques such as XRD, SEM, TEM, AFM, UV, PL, Raman spectroscopy etc. The pure and Cd doped ZnO nanoparticles are subjected to XRD and SEM in the present work.

5.2. X- ray powder diffraction

X-Ray diffraction is a versatile technique used to investigate a wide range of structural aspects in crystalline samples. The attainable information ranges from microscopic features, such as the arrangement of the crystal components, to macroscopic information, such as the mean shape and size of crystals. This information can be obtained by analyzing the full width at half maximum (FWHM) of the Bragg reflections. Since every Bragg peak is associated with a unique crystallographic direction, the FWHM is influenced by the number of atoms contributing to the scattering events and this number is directly connected to the size of the crystal planes generating the specific reflection. Different sizes for different crystallographic directions are associated to a specific shape (i.e., morphology) of the crystallites, which can therefore be refined against the XRD pattern. For a defined crystallographic direction, the mean value of the crystal size can be estimated by using the Scherrer equation (Equation (1)), often erroneously referred to as Debye–Scherrer equation.**[51]** This equation considers the ideal condition of a perfectly parallel, infinitely narrow and monochromatic X-ray beam incident on a monodisperse powder of cube-shaped crystallites.**[52]** The equation is $K\lambda = D_{hkl} B_{hkl} \cos\theta$ (1) where D_{hkl} is the crystallite size in the direction perpendicular to the lattice planes, hkl are the Miller indices of the planes belonging to the peak that is being analyzed, K is a numerical factor commonly referred to as the crystallite-shape factor,**[53]** λ is the wavelength of the X-rays, B_{hkl} is the FWHM of the diffraction peak in radians, and θ is the Bragg angle. Given the strong assumptions regarding the instrumental ideality, the extracted mean size value always needs to be corrected for instrumental broadening effects. Standard phases with known crystal size and narrow size distribution are commonly used to calculate the instrumental broadening, or $FWHM_{instr}$ whose contribution needs to be subtracted from the

FWHM used in the Scherrer equation. Although this equation constitutes a valuable approach to estimating the mean crystallite size of a polycrystalline sample, the user must be aware of some important issues. First, when reflections related to different crystallographic directions are used for extracting a unique value of crystallite size, any information regarding the crystal shape is lost as the final size value is averaged over all the crystallographic directions. Second, other structural features of the sample contribute to the peak broadening besides crystal size, such as lattice strain, defects or the nanoparticle size itself, **[54–57]** resulting in overestimated FWHM values and consequent underestimated crystal size. Lastly, but most importantly, the information available by XRD experiments arises from the structural properties of crystal domains and not necessarily from the entire particle **[58].**

5.3. Scanning electron microscopy

Scanning electron microscope enables imaging the sample surface by detecting secondary electrons emitted from the sample upon interaction with the impinging electron beam **[59]**. In SEM, lower beam energies are utilized for sample imaging as compared to TEM characterization, which results in a limited penetration depth of the beam and, hence, in being sensitive solely to the specimen surface. However, this superficial interaction also implies that SEM characterization can be used for the analysis of the morphology of "thick" (>100 nm) samples, which is not possible with TEM. **[60-62]** The moderate electron energies employed for SEM analysis limit the resolution to typically >2–3 nm, however at the same time drastically decrease the possibility of beam-induced sample damage compared to measurements and features lower acquisition and maintenance costs than TEM. SEM instruments typically also enable investigating the composition of the sample surface by measuring the amount of elastically backscattered electrons, which depends on the interaction between the focused electrons and the sample material, or by detecting x-ray emission due to e-beam ionization. **[60,61]**

CHAPTER 6

RESULT AND DISCUSSION

6.1. Characterization using XRD

The structural characterization of the pure ZnO and Cd doped ZnO nanoparticles with two different concentrations such as 0.01M and 0.03M are carried out by the XRD method. The x-ray diffraction experiments are carried out with the XPERT-PRO diffraction system using the CuK_{α} radiation of wavelength 1.5406Å. The type of the scan used is continuous and range from 10° to 80°. The average grain size is calculated using the Debye Scherrer formula,

$$D=K\lambda/\beta\cos\theta$$

λ - X-ray wavelength

β -line broadening at half the maximum intensity (FWHM)

θ- Bragg angle

The dislocation density is found out using the formula,

$$\delta=1/D^2 \text{ (lines/m}^2\text{)}$$

The XRD pattern for the pure ZnO nanoparticles with the high intensity peaks observed at $2\theta=36.31^0$ along the (1 0 1) hkl plane, $2\theta=31.83^0$ along the (1 0 0) hkl plane are presented in Fig.6.1.

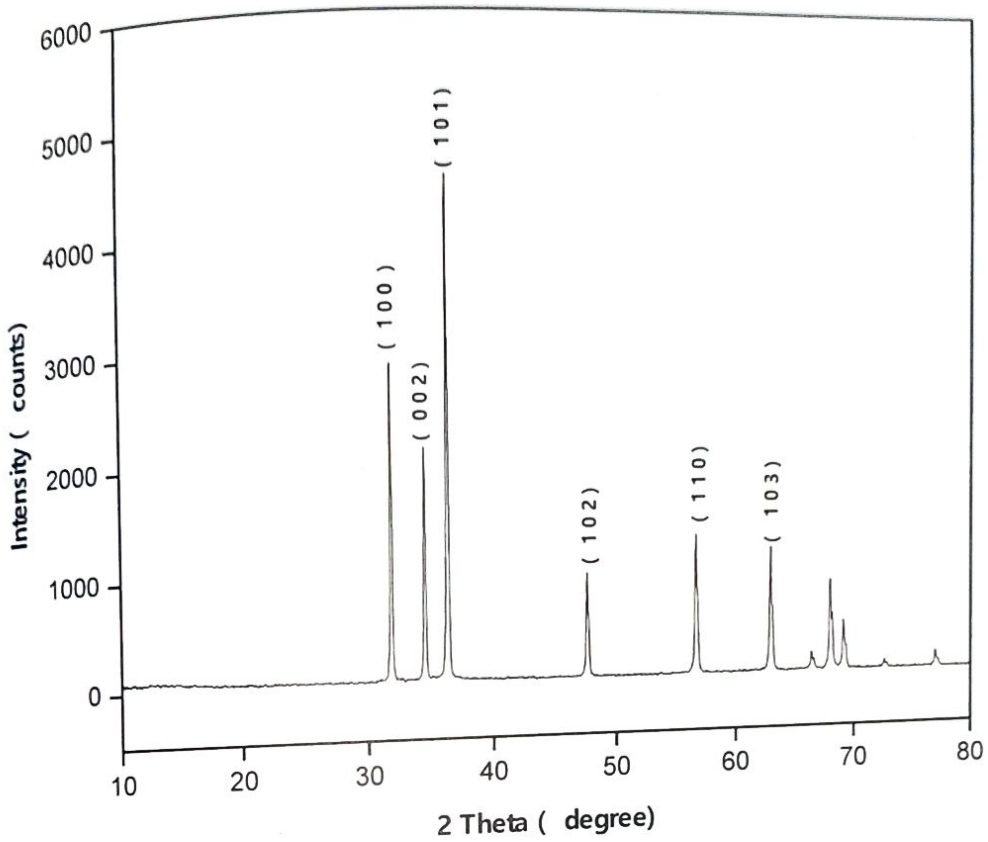

Fig.6.1. XRD pattern of pure ZnO nanoparticles

The d- spacing values obtained from XRD data of the pure ZnO nanoparticles are identified with the JCPDS File no.36-1451 with hexagonal structure and their respective hkl and relative intensity values are presented in Table 6.1.

Table 6.1. Comparison of standard and observed d- spacing values of ZnO nanoparticles

S. No	2θ (degree)	Observed d-spacing (Å)	JCPDS d-spacing (Å)	hkl	Relative intensity (%)
1.	31.8344	2.8111	2.8143	1 0 0	63.70
2.	34.4953	2.6001	2.6033	0 0 2	45.71
3.	36.3137	2.4739	2.4759	1 0 1	100.00
4.	47.5802	1.9111	1.9111	1 0 2	20.72
5.	56.6183	1.6256	1.6247	1 1 0	26.80
6.	62.8942	1.4764	1.4771	1 0 3	23.82
7.	66.3999	1.4067	1.4071	2 0 0	3.67
8.	67.9709	1.3780	1.3781	1 1 2	18.53
9.	69.1083	1.3581	1.3582	2 0 1	9.92
10.	72.6116	1.3009	1.3017	0 0 4	1.55
11.	76.9839	1.2376	1.2380	2 0 2	1.32

The XRD pattern for the 0.01M Cd (cadmium) doped ZnO nanoparticles with the high intensity peaks observed at $2\theta=36.28^0$ along the (1 0 1) hkl plane, $2\theta=31.80^0$ along the (1 0 0) hkl plane are presented in Fig.6.2

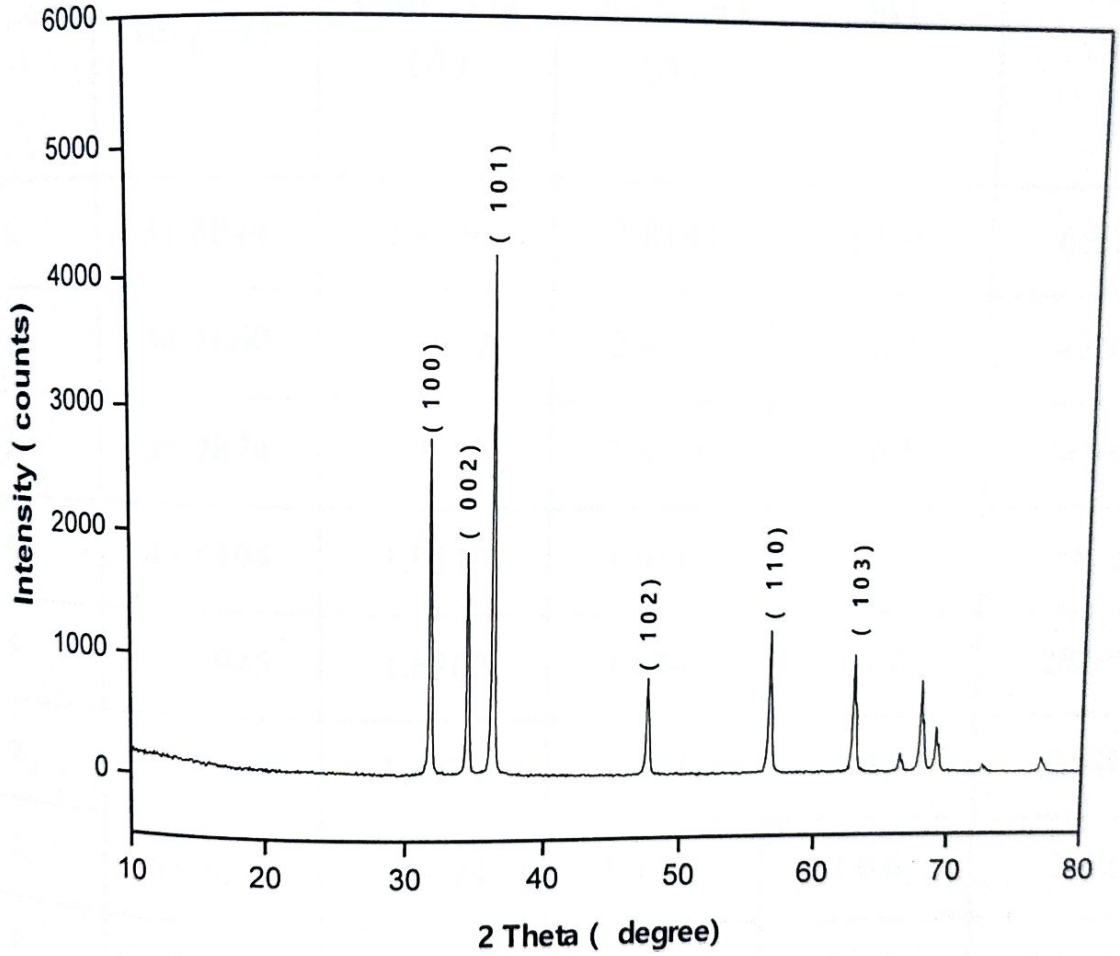

Fig.6.2. XRD pattern of 0.01M Cd (cadmium) doped ZnO nanoparticles

The d- spacing values obtained from XRD data of the 0.01M Cd(cadmium) doped ZnO nanoparticles are identified with the JCPDS File no.36-1451 with hexagonal

structure and their respective hkl and relative intensity values are presented in Table 6.2.

Table 6.2. Comparison of standard and observed d- spacing values of 0.01M Cd doped ZnO nanoparticles

S. No	2θ (degree)	Observed d-spacing (Å)	JCPDS d-spacing (Å)	hkl	Relative intensity (%)
1.	31.8044	2.8136	2.8143	1 0 0	65.18
2.	34.4660	2.6022	2.6033	0 0 2	42.83
3.	36.2874	2.4757	2.4759	1 0 1	100.00
4.	47.5594	1.9119	1.9111	1 0 2	19.26
5.	56.5945	1.6262	1.6247	1 1 0	28.29
6.	62.8606	1.4771	1.4771	1 0 3	22.81
7.	66.3634	1.4074	1.4071	2 0 0	3.44
8.	67.9454	1.3784	1.3781	1 1 2	18.00
9.	69.0786	1.3586	1.3582	2 0 1	8.98
10.	72.5769	1.3015	1.3017	0 0 4	1.54
11.	76.9626	1.2379	1.2380	2 0 2	2.86

The XRD pattern for the 0.03M Cd (cadmium) doped ZnO nanoparticles with the high intensity peaks observed at $2\theta=36.26^0$ along the (1 0 1) hkl plane, $2\theta=31.78^0$ along the (1 0 0) hkl plane are presented in Fig.6.3

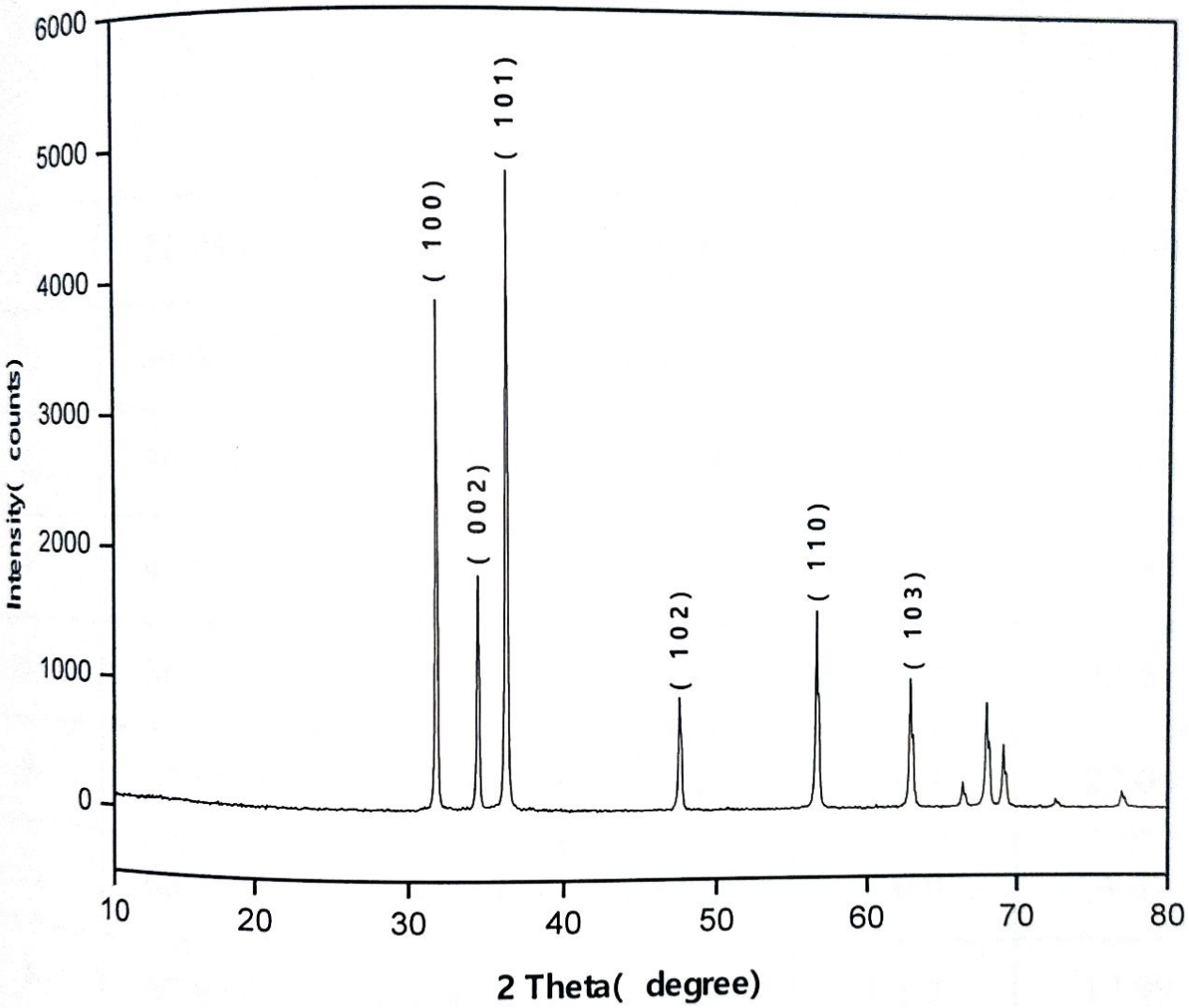

Fig.6.3 XRD pattern of 0.03M Cd (cadmium) doped ZnO nanoparticles

The d- spacing values obtained from XRD data of the 0.03M d doped ZnO nanoparticles are identified with the JCPDS File no.36-1451 with hexagonal

structure and their respective hkl and relative intensity values are presented in Table 6.3.

Table 6.3 Comparison of standard and observed d- spacing values of 0.03M Cd doped ZnO nanoparticles

S. No	2θ (degree)	Observed d-spacing (Å)	JCPDS d-spacing (Å)	hkl	Relative intensity (%)
1.	31.7865	2.81522	2.8143	1 0 0	73.50
2.	34.4387	2.60424	2.6033	0 0 2	39.41
3.	36.2684	2.47696	2.4759	1 0 1	100.00
4.	47.5312	1.91301	1.9111	1 0 2	19.53
5.	56.5755	1.62545	1.6247	1 1 0	32.51
6.	62.8408	1.47761	1.4771	1 0 3	22.04
7.	66.3595	1.40754	1.4071	2 0 0	4.37
8.	67.9272	1.37882	1.3781	1 1 2	17.99
9.	69.0678	1.35881	1.3582	2 0 1	10.63
10.	72.9550	1.30065	1.3017	0 0 4	0.93
11.	76.9550	1.23801	1.2380	2 0 2	2.78

From the experimental data, the average grain size estimated from the Debye Scherrer formula and dislocation density of pure and Cd doped ZnO are presented in table 6.4.

Table 6.4. Average grain size and dislocation density of pure and Cd doped ZnO nanoparticles

S. No	Sample	Average grain size (nm)	Dislocation density(lines/m^2) x 10^{15}
1.	Pure ZnO Calcined at 650°	57	0.486139
2.	0.01M % Cadmium doped ZnO	52	0.403024
3.	0.03M %Cadmium doped ZnO	49	0.324270

All the samples exhibit hexagonal structure as confirmed from the JCPDS File no. 36-1451. XRD results attributed in the present study are in good agreement with the standard values. The absence of impurity peaks reveals that the Cd doped ZnO nanoparticles exhibits high crystalline quality. The average grain size of the pure ZnO nanoparticle is 57 nm. As the Cadmium dopant is incorporated at 0.01M, the average grain size decreases to 52 nm. As the Cadmium concentration is increased to 0.03M, the average size of the particle is further reduced to 49 nm.

6.2. Characterization using SEM

The morphology of pure and Cd doped ZnO nanoparticles have been investigated. The SEM images are as shown in Fig.6.4 – Fig.6.6.

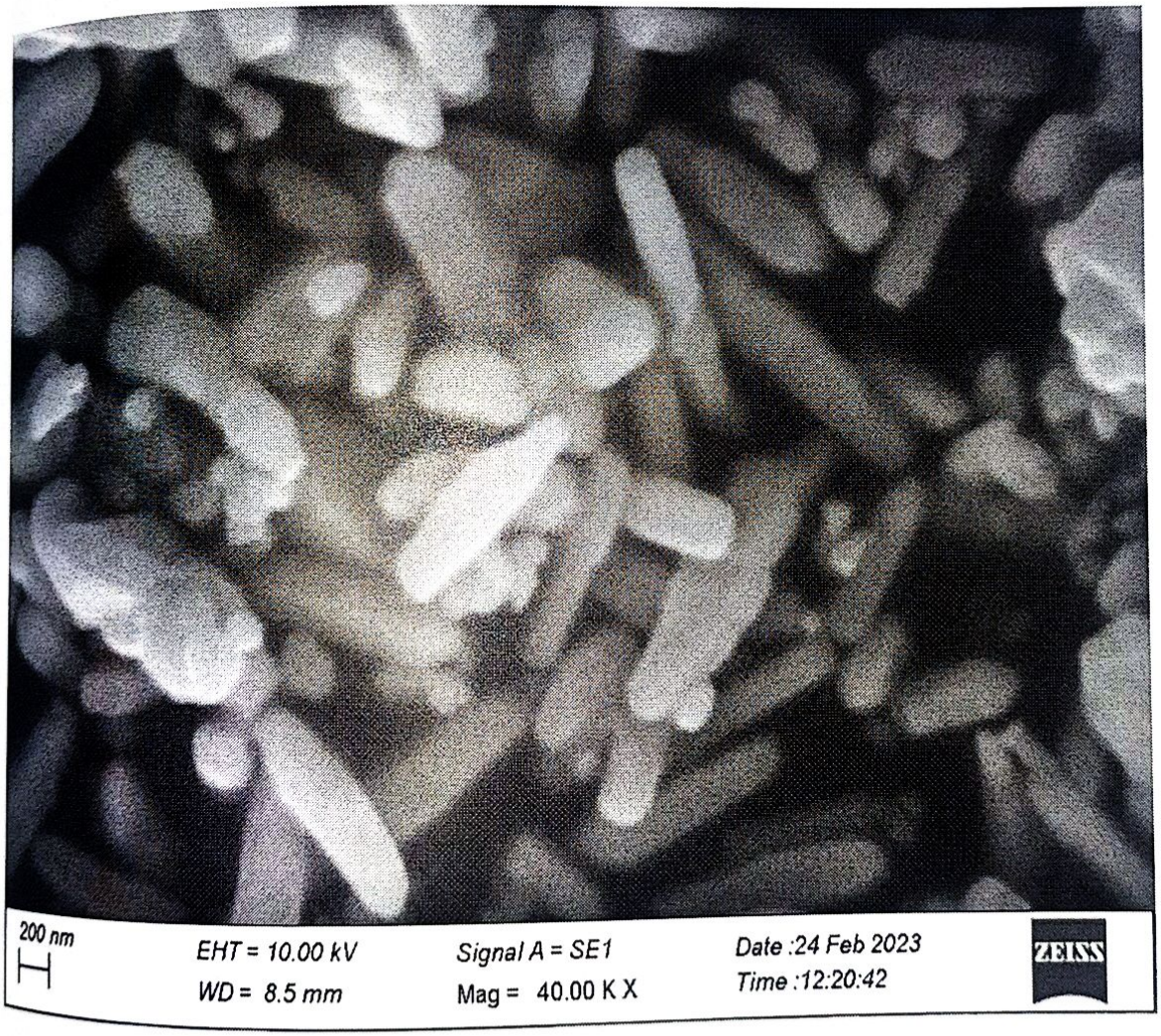

Fig. 6.4. SEM image of pure ZnO nanoparticles

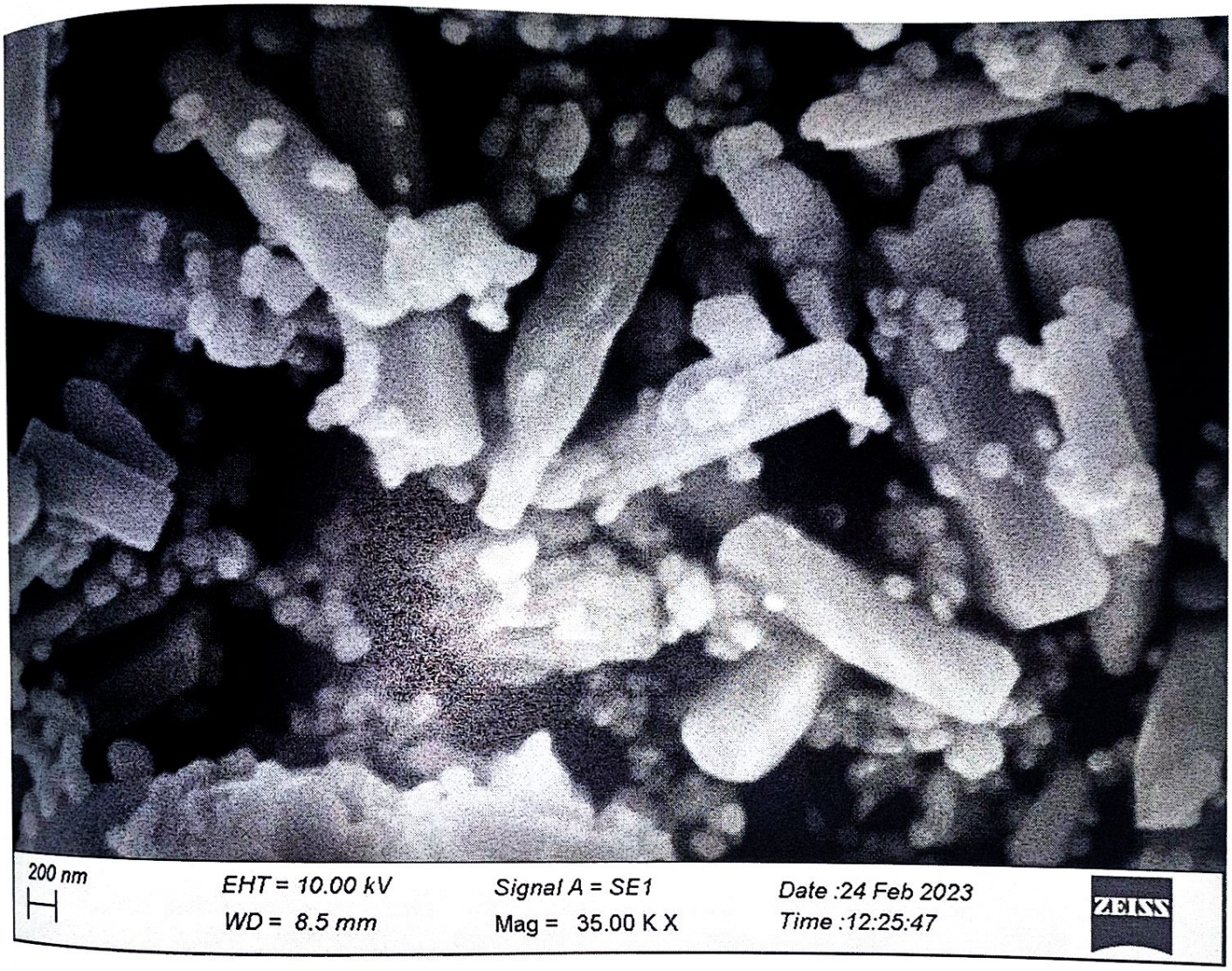

Fig. 6.5 SEM image of 0.01M Cd doped ZnO nanoparticles

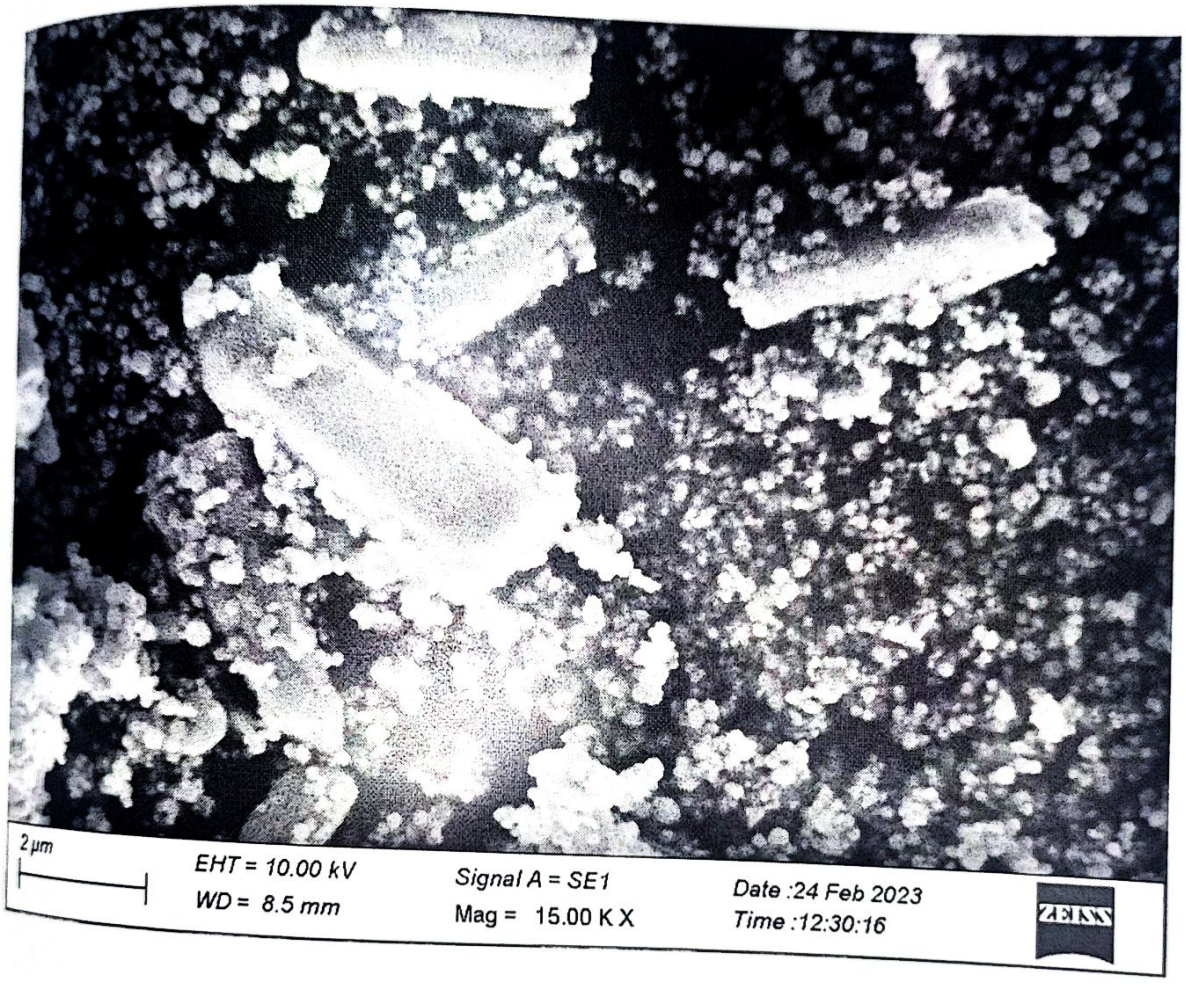

Fig 6.6. SEM image of 0.03M Cd doped ZnO nanoparticles

The surface SEM image of pure ZnO nanoparticles (Fig.6.4) show rod like structures. The fine particle size results in a large surface area that in turn, enhances the catalytic property of the nanoparticles. The SEM images of 0.01M Cd doped ZnO nanoparticles exhibit (Fig.6.5) a combination of rod structures with spherical shape. This spherical shape may be attributed to the incorporation of Cd ions. The SEM image of 0.03M Cd doped nanoparticles show a combination of spherical shape with some rod structures. As the Cd concentration is increased, the shape of the particles is changed from rod to spherical structure.

CHAPTER 7

SUMMARY AND CONCLUSION

In the present investigation, pure and Cd doped nanoparticles are prepared by sol gel method with two different concentrations. This process has advantages of rapid preparation, easy control of particle size and shape. From XRD studies, it is found that all the samples exhibit hexagonal structure as confirmed from the JCPDS File no. 36-1451. The absence of impurity peaks reveals that the Cd doped ZnO nanoparticles to exhibit high crystalline quality. The average size of the particle is 57 nm. As Cd is incorporated, the size of the particle decreases which indicates the crystallinity of the sample can be improved by doping From SEM analysis, it is concluded that the formation of nano rods. As Cd is incorporated the shape of the powder exhibits spherical shape. As the Cd concentration increases, the spherical shape dominates It is still needed for synthesizing high quality and ultrafine nanoparticles with required characteristics in terms of their size, shape, morphology, optical and magnetic properties and so on. So, the ZnO nanoparticles can be synthesized using different methods with varying reaction parameters to suit potential applications in future.

CHAPTER 8

REFERENCE

1. Standard Mansoori G., Fauzi Soelaiman T. Nanotechnology—An Introduction for the s Community. J. ASTM Int. 2005; 2:1–22.

2. U.S. Environmental Protection Agency (): "Module 3: Characteristics of Particles Particle Size Categories".

3. Vert, M.; Doi, Y.; Hellwich, K. H.; Hess, M.; Hodge, P.; Kubisa, P.; Rinaudo, M.; Schué, F. O. (2012). "Terminology for biorelated polymers and applications (IUPAC Recommendations 2012)". Pure and Applied Chemistry. **84** (2): 377 410.

4. Vert, Michel; Doi, Yoshiharu; Hellwich, Karl-Heinz; Hess, Michael; Hodge, Philip; Kubisa, Przemyslaw; Rinaudo, Marguerite; Schué, François (11 January 2012). "Terminology for biorelated polymers and applications (IUPAC Recommendations 2012)". Pure and Applied Chemistry. **84** (2): 377–410.

5. Torres-Torres, C; López-Suárez, A; Can-Uc, B; Rangel-Rojo, R; Tamayo-Rivera, L; Oliver, A (24 July 2015). "Collective optical Kerr effect exhibited by an integrated configuration of silicon quantum dots and gold nanoparticles embedded in ion-implanted silica". Nanotechnology. **26** (29): 295701.

6. Chae, Seung Yong; Park, Myun Kyu; Lee, Sang Kyung; Kim, Taek Young; Kim, Sang Kyu; Lee, Wan In (August 2003). "Preparation of Size-Controlled TiO 2 Nanoparticles and Derivation of Optically Transparent Photocatalytic Films". Chemistry of Materials. **15** (17): 3326–3331.

7. Jacques Simonis, Jean; Koetzee Basson, Albertus (2011). "Evaluation of a low-cost ceramic micro-porous filter for elimination of common disease microorganisms". Physics and Chemistry of the Earth, Parts A/B/C. **36** (14–15): 1129–1134.

8. Silvera Batista, C. A.; Larson, R. G.; Kotov, N. A. (9 October 2015). "Nonadditivity of nanoparticle interactions". *Science*. **350** (6257): 1242477

9. Cai, Wei; Nix, William D. (September 2016). Imperfections in Crystalline Solids. *Cambridge Core*. Retrieved 21 May 2020.

10. Chen, Chien-Chun; Zhu, Chun; White, Edward R.; Chiu, Chin-Yi; Scott, M. C.; Regan, B. C.; Marks, Laurence D.; Huang, Yu; Miao, Jianwei (April 2013). "Three-dimensional imaging of dislocations in a nanoparticle at atomic resolution". Nature. **496** (7443): 74–77.

11. Guo, Dan; Xie, Guoxin; Luo, Jianbin (8 January 2014). "Mechanical properties of nanoparticles: basics and applications". Journal of Physics D: Applied Physics. **47** (1): 013001.

12. Khan, Ibrahim; Saeed, Khalid; Khan, Idrees (November 2019). "Nanoparticles: Properties, applications and toxicities". Arabian Journal of Chemistry. **12** (7): 908–931.

13. Carlton, C.E.; Rabenberg, L.; Ferreira, P.J. (September 2008). "On the nucleation of partial dislocations in nanoparticles". Philosophical Magazine Letters. **88** (9–10): 715–724.

14. "Anisotropic Nanostructures". Mirkin. Retrieved 22 August 2021.

15. Sajanlal, Panikkanvalappil R.; Sreeprasad, Theruvakkattil S.; Samal, Akshaya K.; Pradeep, Thalappil (16 February 2011). "Anisotropic nanomaterials: structure, growth, assembly, and functions". Nano Reviews. **2**: 5883.

16. Knauer, Andrea; Koehler, J. Michael (2016). "Explanation of the size dependent in-plane optical resonance of triangular silver nanoprisms". Physical Chemistry Chemical Physics. 18 (23): 15943-15949.

17. Vinodkumar Etacheri, Roshith Roshan, and Vishwanathan Kumar, (2012) "Efficient Sunlight-Driven Photocatalysis", Article in ACS Applied Materials & Interfaces May (2012).

18. R. Vishwanatha, Y. Arthoba Nayaka, C.C. Vidyasagar, T.G. Venkatesh (2012), "Structural and Optical properties of Mg doped ZnO nanoparticles". Journal of Chemical and Pharmaceutical Research,2012,4(4):1983-1989.

19. Pradeev raj ,Sadaiyandi, A. Kennedy, Suresh Sagadevan, Zaira Zaman Chowdhury5, (2018) "Enhanced Photocatalytic Evaluation and Antibacterial Analysis".

20. Samuel Adesoye ,Saqer Al Abdullah , Kyle Nowlin and Kristen Dellinger (2022), "Tunable Band Gaps for Surface-Enhanced Raman Scattering (SERS)-Based Sensing"

21. Kangathara Sabari ,L. Saravanan ,and S. Elangovan ,(2022)"Synthesis, Characterization, and Comparison of Pure Zinc Oxide"Research article.

22. Charlesbaba ,kopalakrishnan.K,Elango.M (2016) "spin coated cadmium doped zinc oxide thin films"

23. Arun jose , Allwin Joseph ,Arun Mathew ,Mary linut (2013) " preparation and characterization of cadmium doped zinc oxide by Combustion method"International journal of science and research.

24. Poornima (2019) "Coated on glass substrate by dip coating method"International journal of scientific research and review

25. Jianfeng Li , Meiling ren,jicheng quing , yufei wang,zezhou liang(2019) "Electron transport layer to achieve high performance polymer solar cells through improve conductivity and light transmittance".

26. Balamurugan ,sateesh Kumar, Syed khadar(2019) "Simple chemical method"journal of applied science and computation.

27. Yu-Chih, Yow-Jon Lin b, n, Hsing-Cheng Chang c, Ya-Hui Chen d, Chia-Jyi Liu a, Yi-Yan Zou a (2012)" Effects of Ti content on the optical and structural properties of the Ti-dopedZnO nanoparticles"(Journal of luminescence)

28. Raji, Balachandra Kumar "Structural, optical and magnetic properties of zinc oxide"(2018).

29. Darmadi,. A Taufik and R Saleh (2020) " nanoparticles synthesized by co-precipitation method " Department of Physics, Faculty of Mathematics and Natural Science, journal of physics.

30. Orrattajong prateep, Pathitta, Rachatpuranasampruthi, Kornkamon (2018) "Synthesis of nanoparticulate Ti-doped ZnO by solution combustion technique", journal of metals, meterial and minerals.

31. Vignesh, Kanikairaj, Department of Physics, St. Joseph's College (Autonomous), Tiruchirappalli-620 002, India (2017) "Microwave synthesis", International journal of scientific research and technology.

32. Zhan Hong ma, Fengzhang Ren, Zhouya Yang (2020) "Experimental and theoretical investigation" optik, volume 241.

33. Madhava P. Dasari, Umadevi Godavarti, Vishwanath Mote (2018), "Structural, morphological, magnetic and electrical properties of Ni-doped ZnO nanoparticles synthesized by co-precipitation method". Processing and Applications of Ceramics 12 [2] (2018) 100-110.

34. Zahra Manzoor, Vishal Saravade, Alexis Margaret Corda, IaFerguson, and Na Lu (2020) "Metal organic chemical vapor deposition at different reaction chamber conditions".

35. Mary V. Manonmonia, A. M. R. Balan, P. S. Karthik, S. P. Malliappane Department of Chemistry, Annamalai University, Chidambaram, (2022) "Aloe vera extract for enhanced photocatalytic and antibacterial activities".

36. Fernanda et al. (2015)," Optical and electrochemical properties"

37. Alebel Nibret, O.P. Yadav, Isabel Diaz and Abi M. Taddesse (2015), "Cr-N CO-doped ZnO Nanoparticles: Synthesis, Characterization and Photocatalytic activity for degradation of thymol blue". Chemical society of Ethiopia 2015, 29(2), 247-258.

38. Alexei Alexandrov, Mariya Zvaigzyne, Dmitri Lypenko, Igor Nabiev, Pavel Samokhvalov (2020), "Al-, Ga-, Mg-, or Li-doped zinc oxide nanoparticles as electron transport layers for quantum dot light-emitting diodes". Scientific reports 2020, 10:7496.

39. Paul Chalker, Karl Dawson, Peter J. King, Simon Romani (2012), "Atomic layer deposition of germanium-doped zinc oxide films with tuneable ultraviolet emission". Journal of Materials Chemistry 2012, 10.1039/C2JM31391J.

40. Zinc Oxide-Wikipedia

41. Meyer B, Marx D. Density functional study of the structure and stability of ZnO surfaces. Phys Rev B.2003; 67:035403

42. A. K. Radzimska and T. Jesionowski //Materials 7 (2014) 2833

43. M.J. Osmond and M. J. McCall //Nanotoxicology 4 (2010) 15

44. T.N.V.K.V. Prasad, P. Sudhakar and Y. Sreenivasulu // Journal of Plant Nutrition 35 (2012) 905.

45. Das, A.; Wang, D.Y.; Leuteritz, A.; Subramaniam, K.; Greenwell, H.C.; Wagenknecht, U.; Heinrich, G. Preparation of zinc oxide free, transparent rubber nanocomposites using a layered double hydroxide filler. J. Mater. Chem. 2011, 21, 7194–7200.

46. Liu, H.; Yang, D.; Yang, H.; Zhang, H.; Zhang, W.; Fang, Y.; Liu, Z.; Tian, L.; Lin, B.; Yan, J.; et al. Comparative study of respiratory tract immune toxicity induced by three sterilization nanoparticles: Silver, zinc oxide and oxide. J. Hazard. Mater. 2013, 248, 478–486.

47. Mirhosseini, M.; Firouzabadi, F. Antibacterial activity of zinc oxide nanoparticle suspensions on food-borne pathogens. Int. J. Dairy Technol. 2012, 65, 1–5.

48. Ebelmen, J. J. (1844). Comptes rendus de l'Académie des Sciences. 19, 398

49. Seabra, A., & Durán, N. (2015)." Nanotoxicology of metal oxide nanoparticles. Metals", 5(2), 934–975.

50. Mondal, K. (2017). Recent advances in the synthesis of metal oxide nanofibers and their environmental remediation applications. Inventions, 2(2), 9.

51. U. Holzwarth, N. Gibson, Nat. Nanotechnol. 2011, 6, 534.

52. P. Scherrer, Nachr. Akad. Wiss. Goettingen, Math-Phys. Kl. 1918, 1918, 98.

53. H. Klug, L. Alexander, X-Ray Diffraction Procedures: For Polycrystalline and Amorphous Materials, 2nd ed., John Wiley & Sons, New York 1974.

54. S. Britto, S. Joseph, P. Vishnu Kamath, J. Chem. Sci. 2010, 122, 751.

55. P. Muhammed Shafi, A. Chandra Bose, AIP Adv. 2015, 5, 057137.

56. A. V. Vorontsov, S. V. Tsybulya, Ind. Eng. Chem. Res. 2018, 57, 2526.

57. I. Robinson, J. Phys. Soc. Jpn. 2013, 82, 021012.

58. A. Cervellino, R. Frison, N. Masciocchi, A. Guagliardi, in X-Ray and Neutron Techniques for Nanomaterials Characterization (Ed: C. Kumar), Springer, Berlin 2016, pp. 545–608.

59. J. P. Patterson, Y. Xu, M.-A. Moradi, N. A. J. M. Sommerdijk, H. Friedrich, Acc. Chem. Res. 2017, 50, 1495.

60. J. Goldstein, D. E. Newbury, J. R. Michael, N. W. M. Ritchie, J. H. J. Scott, D. C. Joy, Scanning Electron Microscopy and X-Ray Microanalysis, Springer-Verlag, New York 2018.

61. S. Rades, V.-D. Hodoroaba, T. Salge, T. Wirth, M. P. Lobera, R. H. Labrador, K. Natte, T. Behnke, T. Gross, W. E. S. Unger, RSC Adv. 2014, 4, 49577.

62. E. Buhr, N. Senftleben, T. Klein, D. Bergmann, D. Gnieser, C. G. Frase, H. Bosse, Meas. Sci. Technol. 2009, 20, 084025.

A SYSTEMATIC STUDY OF DESIGNING MINUS FILTER USING TiO_2 AND SiO_2

PROJECT REPORT

Submitted to

Department of Physics

St. Mary's College (Autonomous), Thoothukudi

Affiliated to

Manonmaniam Sundaranar University, Tirunelveli

In Partial fulfilment of the requirements

for the award of

BACHELOR'S DEGREE IN PHYSICS

Under the Supervision and Guidance of

Dr. M. Sheeba M.Sc., B.Ed., M.Phil., SET, Ph.D.,

DEPARTMENT OF PHYSICS

ST. MARY'S COLLEGE (Autonomous), THOOTHUKUDI.

(Reaccredited with 'A+' Grade by NAAC)

2022-2023

CERTIFICATE

This is to certify that this project work entitled **A SYSTEMATIC STUDY O DESIGNING MINUS FILTER USING TiO_2 AND SiO_2** is submitted St. Mary's College (Autonomous), Thoothukudi in partial fulfilment for the awa of Bachelor's degree in PHYSICS and is a record of work done during the ye 2022-2023 by the following students

GEETHAPRIYA. R	**20AUPH06**
JENIFER ANITRA. A	**20AUPH09**
PREETHA. P. M	**20AUPH25**
SANKARAESWARI. R	**20AUPH27**
SIMONA. D	**20AUPH33**
VARSHA. A	**20AUPH39**

M. Jenifer

GUIDE

Jessie Jacob

HEAD OF THE DEPARTMENT

HEAD
Department of Physics,
St. Mary's College (Autonomous),
Thoothukudi - 628 001.

13/4/23

EXAMINER

Lucia Rose

PRINCIPLE

St. Mary's College (Autonomous)
Thoothukudi - 628 001.

DECLARATION

We hereby declare that the project entitled **A SYSTEMATIC STUDY OF DESIGNING MINUS FILTER USING TiO_2 AND SiO_2** is submitted to St. Mary's College (Autonomous), Thoothukudi affiliated to Manonmaniam Sundaranar Universtiy for the Bachelor's Degree of Science in Physics is our original work and that, it has not previously formed the basis for the award of any Degree, Diploma or similar title.

GEETHAPRIYA. R	**20AUPH06**
JENIFER ANITRA. A	**20AUPH09**
PREETHA. P. M	**20AUPH25**
SANKARAESWARI. R	**20AUPH27**
SIMONA. D	**20AUPH33**
VARSHA. A	**20AUPH39**

ACKNOWLEDGEMENT

We wish to god almighty place on record our sincere and special thanks to our principle, **Dr. Sr. A.S.J. LUCIA ROSE M.Sc., M.Phil., PGDCA., Ph.D.,** who provided necessary facilities in the institution for carrying out our project work.

We would like to record our sincere thanks for the valuable suggestions made by our Head of the Department, **Dr. Sr. JESSIE FERNANDO M.Sc., M.Phil., Ph.D.,** in the completion of our project.

We express our sincere gratitude to our guide **Dr. M. SHEEBA M.Sc., B.Ed., M.Phil., SET, Ph.D.,** whose words of experience and advice have revitalized us to do our project successfully.

We are thankful to all our department staff members for giving useful ideas. We are also thankful to our parents and one and all that have helped us directly and indirectly to bring out this project successfully.

CONTENTS PAGE. NO

CHAPTER-IV

OPTICAL COATING MATERIALS

CHAPTER-V

SUMMARY, CONCLUSION & FUTURE SCOPE

BIBLIOGRAPHY

CHAPTER-I

INTRODUCTION

1.1. Light

Light, electromagnetic radiation that can be detected by the human eye. Electromagnetic radiation occurs over an extremely wide range of wavelengths, from gamma rays with wavelengths less than about 1×10^{-11} metre to radio waves measured in metres. Within that broad spectrum the wavelengths visible to humans occupy a very narrow band, from about 700 nm for red light down to about 400 nm for violet light. The spectral regions adjacent to the visible band are often referred to as light also, infrared at the one end and ultraviolet at the other. The speed of light in a vacuum is a fundamental physical constant, the currently accepted value of which is exactly 299,792,458 metres per second, or about 186,282 miles per second [1].

Fig 1.1: Light

1.2. Thinfilm Coatings

Then thinfilm is layer of material that has a thickness in range of a nanometre to several micrometers. Creating thinfilms using different deposition methods is the basis of many industries. As a simple example, consider a mirror that reflects light with a layer of metal which deposited behind the glass [2].

Fig 1.2: Thinfilm Coatings

1.3. Optical Coating

An optical coating is a thin layer of group of layers of a coating material that is applied to an optical device. There are different types of optical coatings that serve a variety of purposes for equipment used to inspect objects for corrosion and other physical characteristics. Optical coatings are frequently used to reduce or increase reflectivity, filter out certain light wavelengths or split light beams. [3]

Fig: 1.3: Optical Coating

1.4. Single Layer Coating

Simplest form of coating comprising a single layer of low index dielectric material which minimizes the reflection coefficient of the incident solar radiation thus increasing the transmission coefficient of the coverglass [4].

1.5. Minus Filter

Minus filters are optical filters that selectively reject a wavelength band and transmit at both shorter and longer wavelengths. Such filters have various scientific and technological uses, including protection from laser radiation, laser-based fluorescence instrumentation, and Raman spectroscopy.

Using a Rugate filter with continuously modulated refractive indices is a promising method to design a minus filter. It offers various advantages in optical performance, including extremely broad pass-bands and perfectly suppressed ripples by apodization. Even though the theoretical aspects of this filter type and the achievable extraordinary spectral characteristics are clarified, the realization and sufficient reproduction of gradient –index filters is still a challenging problem.

Two- material multilayers are the simplest way to design the minus filter. A quarter-wave HL stack has been suggested as a model for the construction of such filters. [6]

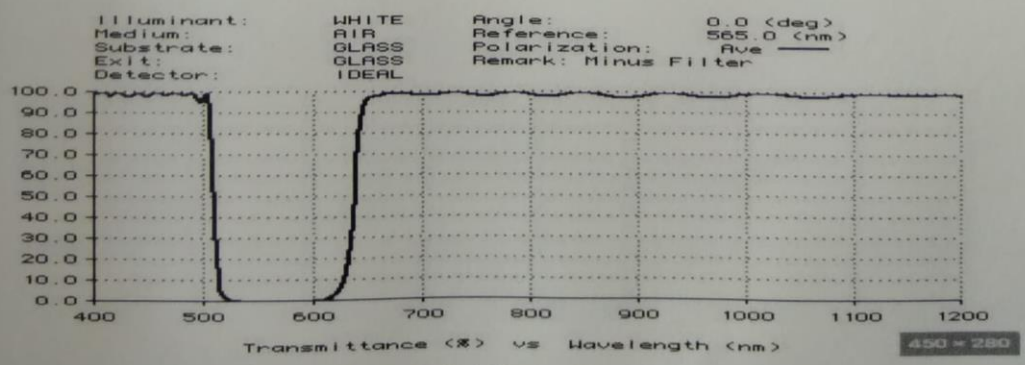

Fig: 1.5: Minus Filter

1.6. Aim of the Project

In this project, glass based minus filter for green colour display is designed and investigated theoretically which consist of zero-k dielectric thinfilms in visible region. Through analytical calculation, the major findings depend on the calculated reflectance and transmittance with the optical Transverse Matrix theory. The reflectance curves in the visible region has been simulated and plotted in Open Filters software. In order to effectively suppress the side lobes of the passband, the conventional stack in optimized by using OpenFilters software. The present work was aimed at

1. Designing of minus filter for green colour display.
2. Formulate and synthesis of minus filter in visible region using Open Filters.
3. Suppressing of the side lobes by optimization.
4. Comparing and analyzing the parameters such as number of layers, physical thickness and reflectance of the chosen materials.
5. Estimate the equations which are used to apply any number of materials having different refractive indices.

CHAPTER-II

FUNDAMENTALS OF OPTICS

2.1. Reflection

Bouncing back of light rays after hitting any surface is called reflection of light. If the surface is smooth and shiny, the light will reflect at the same angle at which it hits the surface. This is called regular reflection and produces good images. If the surface is rough and uneven, then some light rays may get absorbed, while others may reflect at varied angles, called as irregular reflection.[7]

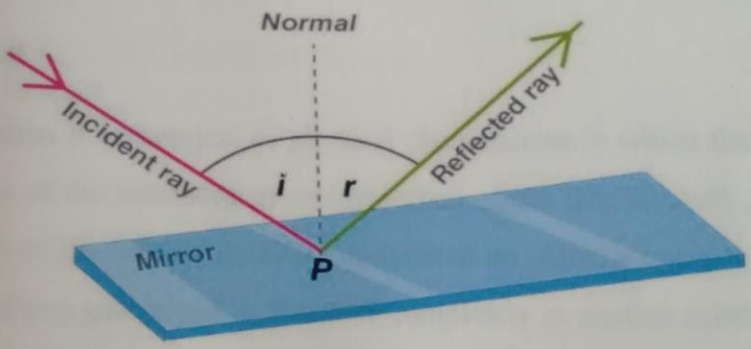

Fig: 2.1: Reflection

2.2. Transmittance

Transmittance is the transmission-mode analog to the reflectance. That is, transmittance is a dimensionless number defined by the ratio of the radiant flux Φ_t. Transmitted to the incidence radiant fluxΦ_i,

$$\tau(\lambda)=\frac{\Phi_t}{\Phi_i}(\lambda) \qquad (2.1)$$

Like the reflectance, conservation of energy dictates that the transmittance for nonfluorescent materials has values in the interval 0-1, inclusive. The diffuse transmittance for real nonfluorescent materials is always less than unity [8].

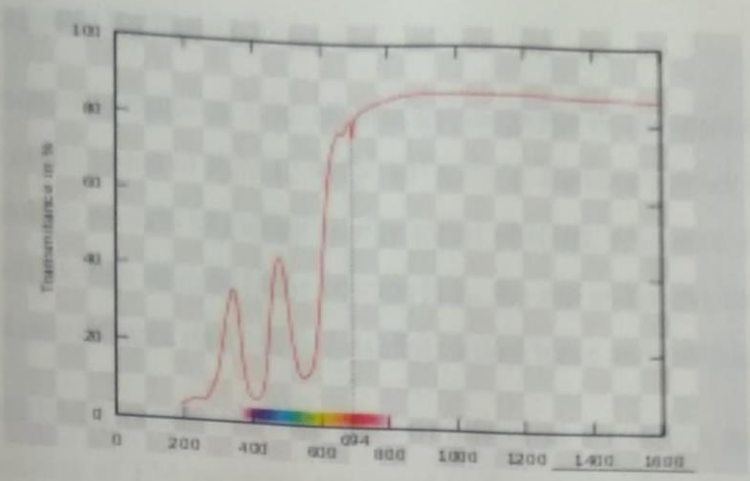

Fig: 2.2: Transmittance

2.3. Absorption

Absorption is a chemical or physical phenomenon in which the molecules atoms and ions of the substance getting absorbed enters into the bulk phase (gas, liquid or solid) of the material in which it is taken up. Absorption is the condition in which something gets mixed or absorbed completely in another substance. In the process of absorption, a substance captures and transforms energy. The absorbent distributes the material it captures evenly through the surface [9].

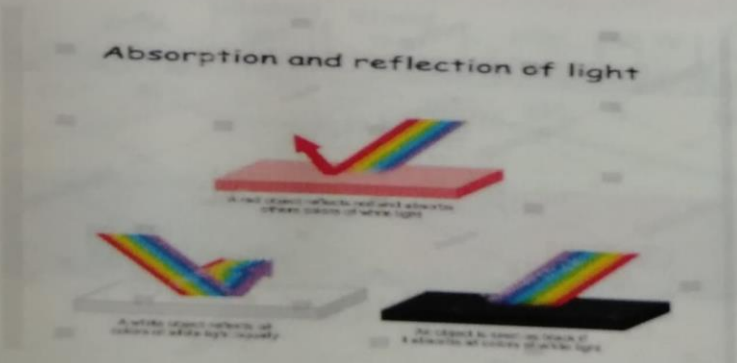

Fig: 2.3: Absorption

2.4. Electromagnetic Radiation

Electromagnetic radiation is an electric and magnetic disturbance travelling through space at the speed of light (2.998×10^{8} m/s). It contains neither mass nor charge but travels in packets of radiant energy called photons, or quanta. Examples of EM radiation include sources in the cosmos (e.g., the sun and stars), radioactive elements, and manufactured devices. EM exhibits a dual wave and particle nature.

Electromagnetic radiation travels in a waveform at a constant speed. The wave characteristics of EM radiation are found in the relationship of velocity to wavelength (the straight line distance of a single cycle) and frequency (cycles per second, or hertz, Hz), expressed in the formula

$$E = h\upsilon$$

$$E = \frac{hc}{\lambda} \qquad (2.2)$$

Where c = velocity, λ = wavelength, and v = frequency [10].

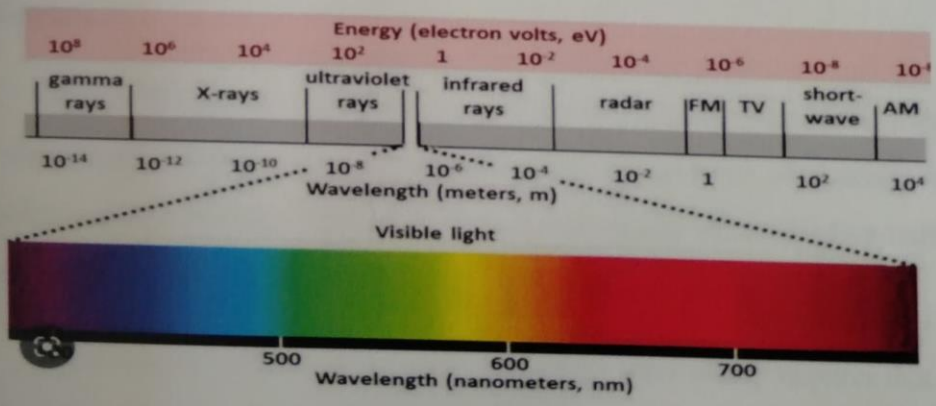

Fig: 2.4 Electromagnetic Radiations

CHAPTER - III

DESIGNING METHODOLOGY

3.1. Theory

The treatment of multilayer film theory used will deal with the resultant electric and magnetic fields and their boundary conditions in the various region. We will dealing with two types of wave function those differentiating between positive and negative going wave $[\vec{E}^{+}(z)$ and $\vec{E}^{-}(z)]$ and those which do not $[\vec{E}(z)$ and $\vec{H}(z)]$. For example $\vec{E}^{+}(z_1)$ represents the resultant of all waves $z=z_1$ travelling in the positive direction and $\vec{E}$ (z_2) represents the resultant of all waves at $z=z_2$ travelling in the both directions. Equation between the first types of wave functions in the massive media on the both sides of the multilayer will lead to the transfer matrix and formulas for the reflectance and transmittance of the multilayer. Equations between the second types of wave functions will lead to the characteristic matrix of a multilayer which only depends on the optical parameters of the multilayer and not on the optical characteristics of the massive media surrounding it.

Consider the linearly polarized wave impinging on a thinfilm (assumed to be non-absorbing, homogeneous and isotropic and of uniform thickness) with refractive index n between two massive transparent media with refractive indices n_0 and n_s. E is assumed to be perpendicular to the incidence plane.

The boundary condition to the electromagnetic wave theory requires that the tangential components of both the electric $(\vec{E})$ and magnetic $(\vec{H})$ filed vectors to be continuous across the boundaries. At boundary $z= z_1$.

$$E(z_1) = E^{+}(z_1-\delta) + E^{-}(z_1-\delta) = E^{+}(Z_1+\delta) + E^{-}(Z_1+\delta) \qquad (3.1)$$

Also,

$$Z_0H(z_1) = [E^+(z_1 - \delta) - E^-(z_1 - \delta)]\, n_0 \cos\alpha_0$$

$$= [E^+(z_1+\delta) - E^-(z_1+\delta)]\, n \cos\alpha \qquad (3.2)$$

Where $Z_0 = \sqrt{\mu_0/\varepsilon_0}$ is the impedance of free space (377Ω in mks units)

α_0= incidence angle (defined as the angle between the propagation vector $\vec{K}$ and the normal to the film surface)

α= angle of wave propagation in the film as determined from Snell's law ($n_0 \sin\alpha_0 = n \sin\alpha$)

Use is made of the fact that the vectors $\vec{E}$ and $\vec{H}$ in nonmagnetic media are related by the refractive index and the unit propagation vector $\vec{K}$

$$\vec{Z_0 H} = n\, \vec{K} \times \vec{E} \qquad (3.3)$$

A wave which traverses the film once undergoes a shift in phase of

$$\varphi = \frac{2\pi\, nd\cos\alpha}{\lambda} \qquad (3.4)$$

$$E(z_1) = E(z_2)\cos\varphi + Z_0H(z_2)\frac{i\sin\varphi}{n} \qquad (3.5)$$

and

$$Z_0H_{(z_1)} = E(z_2)\, i\sin\varphi + Z_0H(z_2)\cos\varphi \qquad (3.6)$$

By adhering to the following convention:

$n \Rightarrow n_s = n\cos\alpha$ for s or perpendicular polarization

$n \Rightarrow n_p = n/\cos\alpha$ for p or parallel polarization (3.7)

$n \Rightarrow n$ for normal light incidence

n now can mean the refractive index as measured with a refractometer or the "effective index" as defined in Eqn. (3.5)

3.2. Characteristic Matrix of a Single Film

In matrix notation, Eqn.3.5 and 3.6 can be written in the following form:

$$\begin{bmatrix} E(z_1) \\ Z0H(z_1) \end{bmatrix} = \begin{bmatrix} \cos\varphi & i\sin\varphi/n \\ in\sin\varphi & \cos\varphi \end{bmatrix} \begin{bmatrix} E(z_2) \\ Z0H(z_2) \end{bmatrix} \quad (3.8)$$

The matrix,

$$M = \begin{bmatrix} \cos\varphi & i\sin\varphi/n \\ in\sin\varphi & \cos\varphi \end{bmatrix} \quad (3.9)$$

It is called the characteristics matrix of the film. It contains only parameters of the film.

3.3. Characteristic Matrix of a Sequence of Layers

The characteristic matrix (Eqn. 3.9) relater the fields at the boundary $Z=Z_2$. It follows, therefore, that if two overlaying film were deposited on the substrate, there would be three boundaries ($Z=z_1$, $Z=z_2$ and $Z=z$) and now

$$\begin{bmatrix} E(z_2) \\ Z0H(z_2) \end{bmatrix} = M_2 \begin{bmatrix} E(z_3) \\ Z0H(z_3) \end{bmatrix}$$

Premultiplying both M_1, we obtain

$$\begin{bmatrix} E(z_1) \\ Z0H(z_1) \end{bmatrix} = M_1 M_2 \begin{bmatrix} E(z_3) \\ Z0H(z_3) \end{bmatrix}$$

In general, if M is the number of layers then the first ($Z=Z_1$) and lost ($Z = Z_{m+1}$) boundary are related by

$$\begin{bmatrix} E(z_1) \\ Z_0H(z_1) \end{bmatrix} = M_1 M_2 \ldots \ldots \ldots M_m \begin{bmatrix} E(z_{m+1}) \\ Z_0H(z_{m+1}) \end{bmatrix} \quad (3.10)$$

We see that the characteristics of the sequence of layers is the resultant of the product of the individual characteristics matrices

$$M = M_1 M_2 M_3 \ldots \ldots \ldots \ldots M_m \quad (3.11)$$

The characteristics matrix of a single layer (Eqn. 3.9) has real elements in the principal diagonal and purely imaginary elements elsewhere, Let us now multiply two matrices A and B of this type

$$\begin{bmatrix} A_{11} & iA_{12} \\ iA_{21} & A_{22} \end{bmatrix} \begin{bmatrix} B_{11} & iB_{12} \\ iB_{21} & B_{22} \end{bmatrix} = \begin{bmatrix} A_{11}B_{11} - A_{12}B_{21} & i(A_{11}B_{12} + A_{12}B_{22}) \\ i(A_{21}B_{11} - A_{22}B_{21}) & -A_{21}B_{12} + A_{22}B_{22} \end{bmatrix}$$

$$= \begin{bmatrix} M_{11} & iM_{12} \\ iM_{21} & M_{22} \end{bmatrix} \quad (3.12)$$

We see that the product matrix M is of the same type as A and B. We can conclude that the characteristic matrix of a sequence or layer also how real elements on the principal diagonal and purely imaginary elements elsewhere.

The most significant feature of this result is the fact that one can represent any sequence of layers by a 2 by 2 matrix completely independent of the parameters of the surrounding media.

3.4. Determinant of the Characteristic Matrix

The determinant of the characteristic matrix of a single layer (Eqn. 3.9) is

$$\det(M) = \cos\varphi \cos\varphi + \sin\varphi \sin\varphi = 1$$

We ask now what is the value of the characteristic matrix of a sequence of layers. Since the multiplication of matrices is performed the same way as the multiplication of determinants, it follows that for square matrices A and B with an equal number of rows.

$$\det(AB) = \det(A)\det(B)$$

we apply this result to Eqn. 3.11 we find

$$\det(M) = \det(M_1)\det(M_2)\det(M_3) \ldots\ldots\ldots\ldots \det(M_m)$$

$$= M_{11}M_{22}+M_{12}M_{21}= 1 \qquad (3.13)$$

Or

In other words: The determinant of the characteristic matrix of a sequence of layers always equals 1.

3.5. Transfer Matrix, Reflectance and Transmittance

In Eqn. 3.10 and 3.11 we established a relationship between the electromagnetic wave functions E and H at the first ($Z=z_1$) and the last ($Z=z_{m+1}$) interface of a multilayer, only inside the multilayer did we have to distinguish between the positive - and negative – going waves. Consequently, no information about the massive media on both sides of multilayer is necessary.

This is different when we want to calculate the reflectance and transmittance of a multilayer relative to specific massive media. We used the following relationship between the electromagnetic wave functions E and H and E^+ and E^-

$$\begin{bmatrix} E \\ ZH \end{bmatrix} = \begin{bmatrix} 1 & 1 \\ n & -n \end{bmatrix} \begin{bmatrix} E^+ \\ E^- \end{bmatrix} \tag{3.14}$$

Applying Eqn. 3.14 to Eqn3.10 and 3.11 we obtain

$$\begin{bmatrix} E^+(z_1-\delta) \\ E^-(z_1-\delta) \end{bmatrix} = \begin{bmatrix} 1 & 1 \\ n & -n \end{bmatrix}^{-1} \begin{bmatrix} M_{11} & iM_{12} \\ iM_{21} & M_{22} \end{bmatrix} \begin{bmatrix} 1 & 1 \\ n & -n \end{bmatrix} \begin{bmatrix} E^+(z_{m+1}+\delta) \\ E^-(z_{m+1}+\delta) \end{bmatrix} \tag{3.15}$$

Or

$$\begin{bmatrix} E^+(z_1-\delta) \\ E^-(z_1-\delta) \end{bmatrix} = \begin{bmatrix} Q_{11} & Q_{12} \\ Q_{21} & Q_{22} \end{bmatrix} \begin{bmatrix} E^+(z_{m+1}+\delta) \\ E^-(z_{m+1}+\delta) \end{bmatrix} \tag{3.16}$$

With

$$Q_{11} = \frac{M_{11} + i\,M_{21}/n_0 + in_s\,M_{12} + n_s\,M_{22}/n_0}{2}$$

$$Q_{12} = \frac{M_{11} + i\,M_{21}/n_0 - in_s\,M_{12} - n_s\,M_{22}/n_0}{2}$$

$$Q_{21} = \frac{M_{11} - iM_{21}/n_0 - in_s\,M_{12} - n_s M_{22}/n_0}{2}$$

$$Q_{22} = \frac{M_{11} - iM_{21}/n_0 - in_s M_{12} + n_s\,M_{22}/n_0}{2}$$

From microwave filter theory we adopt the name transfer matrix for this Q matrix. In the exit medium ($z_1 > z_{m+1}$) there is no negative going wave. We can consequently set $E^-(z_{m+1}+\delta) = 0$. This leads to

$$E^{+}(z_1 - \delta) = Q_{11}E^{+}(z_{m+1} + \delta)$$

$$E^{-}(z_1 - \delta) = Q_{21}E^{+}(z_{m+1} + \delta)$$

It is much as the

Amplitude reflectance

$$\vec{R} = \frac{E^{-}(z1-\delta)}{E^{+}(z1-\delta)} = \frac{Q_{21}}{Q_{11}} \tag{3.17}$$

and the

Amplitude transmittance

$$\vec{T} = \frac{E^{+}(z_{m+1}-\delta)}{E^{+}(z_1-\delta)} \tag{3.18}$$

We can derive out of Eq.3.16

$$\vec{R} = \frac{n_0 M_{11} + i n_0 n_s M_{12} - i M_{21} - n_s M_{22}}{n_0 M_{11} + i n_0 n_s M_{12} + i M_{21} + n_s M_{22}} \tag{3.19}$$

and

$$\vec{T} = \frac{2n_0}{n_0 M_{11} + i n_0 n_s M_{12} + i M_{21} + n_s M_{22}} \tag{3.20}$$

Amplitude reflectance R and transmittance T are connected with energy reflectance R and transmittance T through the pointing vector. We have

$$\vec{R} = \overrightarrow{R}\ \overrightarrow{R^*} \text{ and } T = \frac{n_s}{n_0}\ \vec{T}\ \overrightarrow{T^*} = 1 - R \tag{3.21}$$

Where $\vec{R}$ and $\vec{T}$ are the conjugate complex values of $\vec{R}$ and $\vec{T}$. We consequently can derive from Eqn. 3.19, 3.20, and 3.21

$$T = 1 - R = \frac{4n_0\ n_s}{(n_0 M_{11} + n_s M_{22})^2 + (n_0 n_s M_{12} + M_{21})^2} \tag{3.22}$$

$$= \frac{4}{(2+(\frac{n_0}{n_s})M^2{}_{11}+n_0 n_s M^2{}_{12}+\frac{M^2{}_{21}}{n_0 n_s}+(\frac{n_s}{n_0})M^2{}_{22})}$$

3.6. Description of Designs

A dielectric multilayer design is fully described by the (real) refractive indices and thickness of its individual layers and the refractive indices of the two bounding massive media (incidence and exit medium or surrounding medium and substrate). The angle of incidence α_0 and the wavelength λ specify how and where it is used.

For the thickness description the optical thickness is generally preferred, but in its usual definition but as quarterwave optical thickness (QWOT), since quarter films play such a dominant role in thin film optics. QWOT is defined as the wavelength at which a film is 0.25 wavelengths thick.

$$\emptyset = \pi \text{QWOT}/2\lambda \text{ or QWOT} = 4nd\cos\alpha$$

How do we now write the formula for the design? The indices of refraction of the massive media appear in front (incident medium, most of the time the surrounding medium) and behind (exit medium, most of the time the substrate). The description of the actual multilayer separated by vertical lines is placed in-between. Capital letters stand for layers 0.25 wavelengths thick at a design wavelength λ_0. Individual or groups of layers with different thickness are assigned as

$$\text{Fractional thickness} = \text{QWOT}/\lambda_0$$

[e.g., H/2, 1.05(ABABABBA)] Periodic multilayers are described by placing the layers making up the base period between parentheses and indicating the number of repetitions by a power.

$$\text{ABABABAB} = (\text{AB})^4$$

With this convention a particular design can be described in many different ways. For example, the design.

$$1.0\,|\,(AB)^6 1.1\ \mathrm{A}\ 1.2(BA)^6\,|\,1.52$$

Design with half-wave thick layers invites different theoretical treatment depending on the way they are written. For example,

$$1.52\,|\mathrm{HLHLHHLHLHLHLHLHHLHLHLHLHLHHLHLH}|\ 1.52$$

Can also be written as

$$1.52\,|(\mathrm{HL})^2\,\mathrm{H}\,(\mathrm{HL})^5\,\mathrm{H}\,(\mathrm{HL})^5\,\mathrm{H}\,(\mathrm{HL})^2\,\mathrm{H}|\,1.52$$

Or as

$$1.52\,|\,(\mathrm{HLHLH})\,(\mathrm{HLHLHLHLHLH})^2\,(\mathrm{HLHLH})\,|\,1.52$$

The reflectance and transmittance are best given as functions of the relative wave number λ_0/λ. This way the symmetries if the sine and cosine functions of the characteristic matrix are preserved. The use of QWOT as a thickness unit and λ_0/λ as an independent variable for reflectance and transmittance plots often causes sum conceptual problems. When a design is developed to a wavelength specifications rather than to a wave number specifications one has to remember that a long – wavelength – pass filter is a short frequency – pass filter and that, relative to the wavenumber presentation, features at shorter wavelengths are compressed and at longer wavelengths stretched.

CHAPTER-IV

OPTICAL COATING MATERIALS

4.1. The Selection of Dielectrics

The term of dielectric was coined by William whewell (from diat electric) in response to a request from Michael Faraday. A perfect dielectric is a material with zero electrical conductivity.

Dielectrics are materials that don't allow current to flow. They are more often called insulators because they are the exact opposite of conductors .They are the most commonly used for energy storage in capacitors and to construct radio frequency transmission lines. Here the dielectric thinfilm in selected since the absorbtion in negligible and it is easy to work for producing reflection or transmission with high reflection and low transmission or low reflection and high transmission. A dielectric thinfilm which is high in permittivity and breakdown strength, small in leakage current and long in service life has to be obtained. The range of coating materials and substrates are limited for most applications. Also the most difficult problems is that almost complete lack of the coating materials are transparent to all range of electromagnetic spectrum.

In this project, we have used two dielectric materials namely SiO_2 and TiO_2 with refractive indices of 1.486 and 2.360 [11].

4.1.1. SiO_2 (Silicon dioxide)

Silicon dioxide, also known as silica, is an oxide of silicon with the chemical formula SiO_2, most commonly found in nature as quartz and in various living organisms. In many parts of the world, silica is the major constituent of sand.

SiO_2 is the low-index, low absorption material used in combination with high-index oxide layer coatings that operate in the UV (200nm) to IR (3nm) regions [12].

Applications of SiO_2

It is used in antireflection coatings for near-UV laser optics, all-dielectric mirrors, beam-dividers, bandpass filters and polarizer. Silica can be used in combination with specific high-index layers, for example Hafnia, Zirconia and Tantala, to form multilayer structures with high damage thresholds for specialised UV laser applications . Silica films sometimes are useful in promoting adherence between two dissimilar materials especially oxide compositions. Silica films are amorphous and never obtain the equivalent density, hardness or impermeability of the crystal form [13].

4.1.2. TiO_2 (Titanium dioxide)

Titanium dioxide -also known as Titanium (IV) oxide or Titania is the naturally occuring compound created, when Titanium reacts with Oxygen in the air. As an Oxide, Titanium is found in minerals in the earth's crust. It also found with other elements, including Calcium and Iron. It is well work in the UV around 350nm visual detection ends at 510 nm.

It is a powder that's also used as a white pigment in a variety of products such as sunscreens, paints and plastics. The pigment grade is also known as Titanium white, pigment white 6 or Cl 77891; it is the whitest and brightest of all known pigments [14].

Applications of TiO_2

TiO_2 has been used in optical coatings for the visible region for many years. TiO_2 has two particularly desirable qualities. It provides the highest index film material for the visible region and it is hard and stable in combination with other Oxides coating examples using TiO_2 has the high index material include beam splitters, cold mirrors and heat-reflecting mirrors, and AR on glass and polymer substrates. When paired with SiO_2 films, multilayer combinations totaling in excess of 50 layers have been deposited that show excellent durability and low mechanical stress because the tensile stress of Titania layers is balanced by the compressive stress of the Silica layer [15].

4.2. The Selection of Substrates

Substrates are the basic materials over which thinfilms are coated on. It is made up of various materials including glass, quartz, plastics and transparent conductive substractive. Substrate selection is a viral parameter for optical coating. For this project work, BK7 glass substrate has been chosen.

4.2.1. BK7 Glass

BK7 is a high quality optical glass that is used whenever the additional benefits of Fused Silica are not required. Since BK7 performs well in all chemical tests, and no additional or special handling is required, cost of manufacturing are reduced. It is relatively hard material with extremely low bubble and inclusion content.

It also has an excellent physical and chemical properties for applications in visible and near IR. It is one of the most common glasses used to produce high

quality optics mainly for visible spectrum, The refractive index of BK7 glass substrate is 1.52 [16].

4.3. Simulation Software

In the design of the thinfilm multilayer, it is necessary to find the layer structure which will give a specified performance in advance. This process is much more difficult than straight forward calculation of the properties of a given multilayer. There is no analytical solution to the general problem. The conventional method of design is to arrive at a possible structure for a filter, using several popular techniques such as vector method, Simth's method, the Simth's chart etc. Though there are several useful techniques, the thinfilm filter design is still difficult and tedious to carry out by hand. Therefore the modern design is completed with the computer aided analysis. Providing a starting design, adjustments to the proposed design may be made, then recomputed, until a satisfactory solution is found. The successful application of refinement techniques depends largely on a starting solution; methods of completely automatic synthesis of designs without any starting point are seldom used. Because the number of parameters can potentially be involved, The possibilities without starting design or virtually infinite.

4.3.1. Features of OpenFilters

The design of optical filters relies on powerful computer assisted methods. Many software is available for designing multilayer coating. For the proposed research work, OpenFilter software is used for refining the designed multilayer coating. Stephane Larouche decided to release in-house software, called OpenFilters, under the GNU General Public Licence, an open-source licence. It is programmed in python and C++, and the graphical user interface is implemented

with WX Python. It allows creation of multilayer and graded-index filters and calculation of reflection, transmission, absorption, phase, group delay dispersion, colour, ellipsometric variables, admittance diagram, circle diagram, electric field distribution and generation of reflection, transmission and ellipsometric monitoring curve. It also provides the refinement; needle, step and Fourier transform methods [17].

4.4. Formulation and Synthesis of Green Colour Minus Filter

At this stage, minus filter for green colour display is hypothetically modelled which consist of dielectric materials TiO_2 and SiO_2 in the visible region of the EM spectrum from 400 to 750 nm using BK7 as a glass substrate. Normal incidence of light on the stack from the upper medium is assumed, with the light propagating from left to right [18]. For the formulation and synthesis of minus filter, the stack (3H3L) has chosen. The optical physical thickness of the layers is equal to $\lambda o/4$ at certain designed wavelength of 533 nm.

Let us discuss and compare the reflectance, number of stack, and thickness of the stack on BK7 glass substrate.

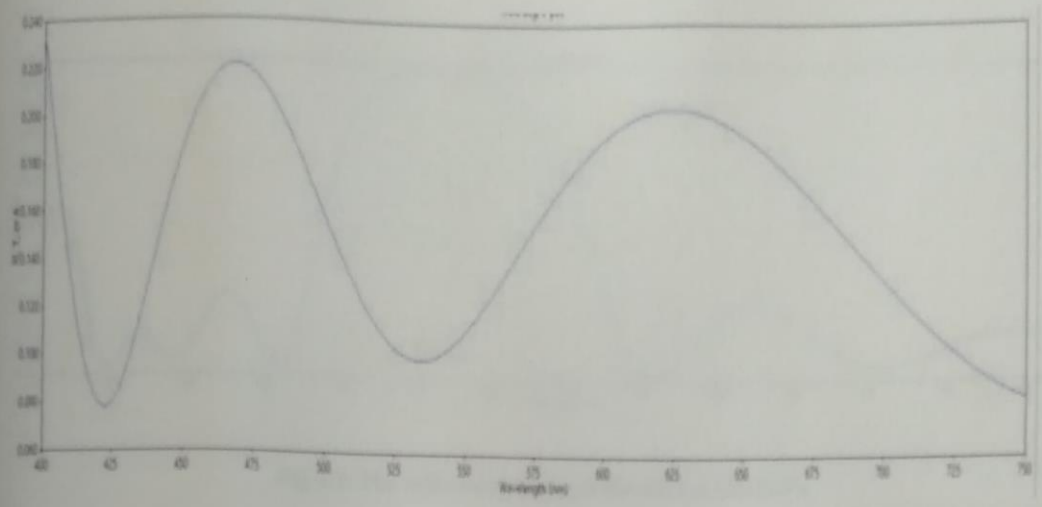

Fig 4.1: The reflectance curve of the stack a|(3H3L)^1|s

Initially, the stack layer is chosen as a$|(3H3L)^1|$s. The thickness and the number of front layers obtained is 438.33 nm and 2. The reflectance is obtained as 9.90%. Fig 4.1 shows that the reflectance curve of the initial stack.

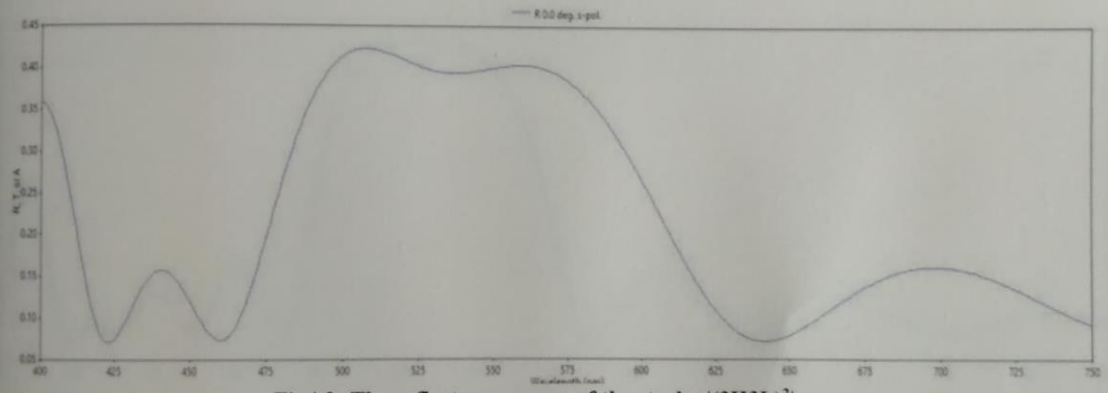

Fig4.2: The reflectance curve of the stack a|(3H3L)^2|s

Next, the stack layer is increased to a$|(3H3L)^2|$s. Here, the number of layers and thickness obtained is 4 and 876.66 nm. The maxmum reflectance of 39.40%`is obtained which is plotted in the fig 4.2.

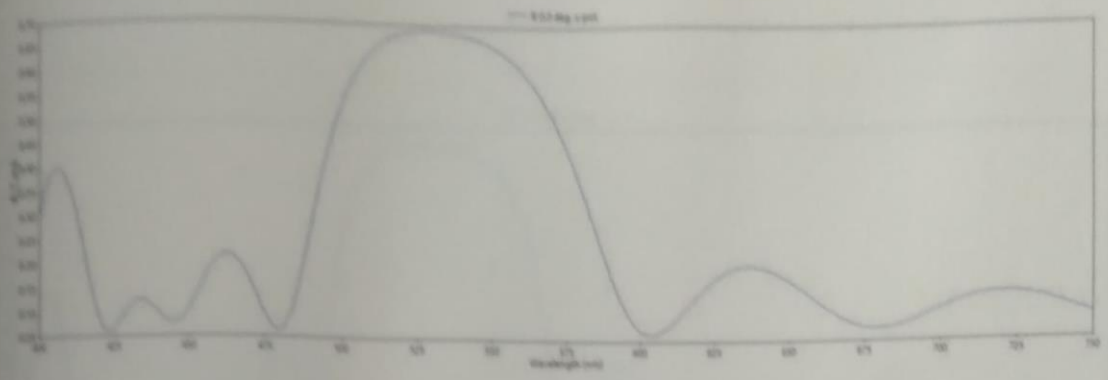

Fig 4.3: The reflectance curve of the stack a| $(3H3L)^3$|s

After that, the stack layer chosen as a|$(3H3L)^3$|s. The reflectance curve of the mentioned stack is shown in fig 4.3. The number of layers and thickness of the chosen stack is 6 and 1314.99 nm. The maximum reflectance is produced by this stack is 68.81%.

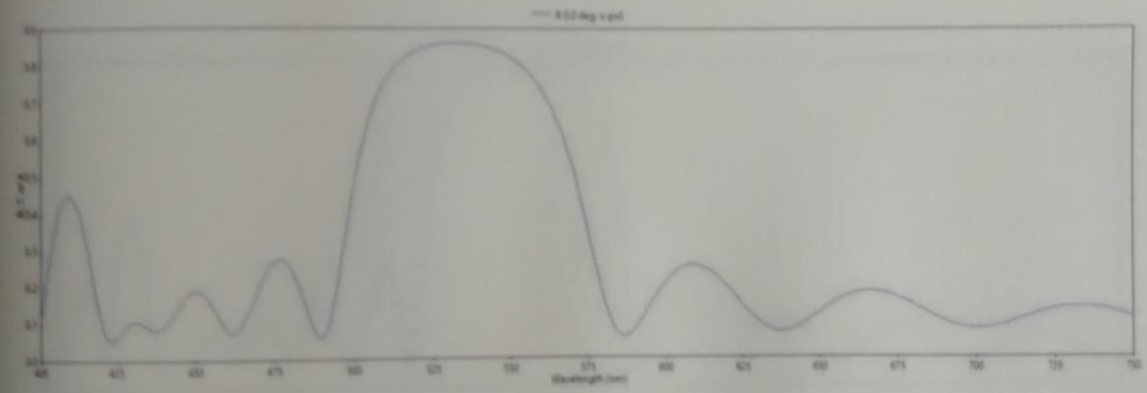

Fig 4.4: the reflectance curve of the stack a|$(3H3L)^4$|s

Next, the reflectance curve of a|$(3H3L)^4$|s is shown in fig 4.4. The maximum reflectance light of 86.12% is reflected by this stack. The thickness and the number of layers are 1753.32 nm & 8 respectively.

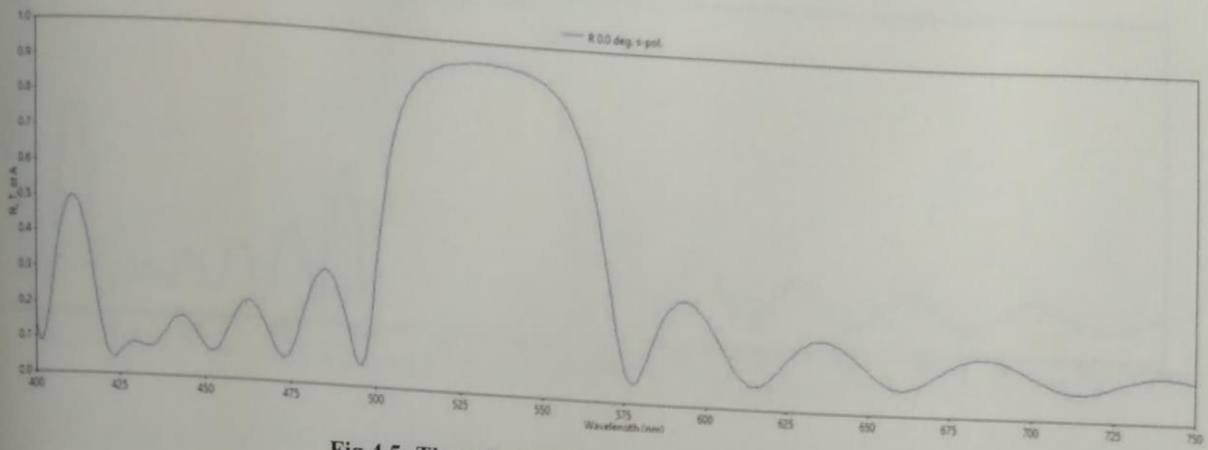

Fig 4.5: The reflectance curve of the stack a|(3H3L)^5|s

Later on, the stack a$|(3H3L)^5|$s is preferred in this stack, the number of layers and thickness obtained is 10 and 2191.65 nm. The reflectance obtained is 94.22% which is shown in the fig 4.5.

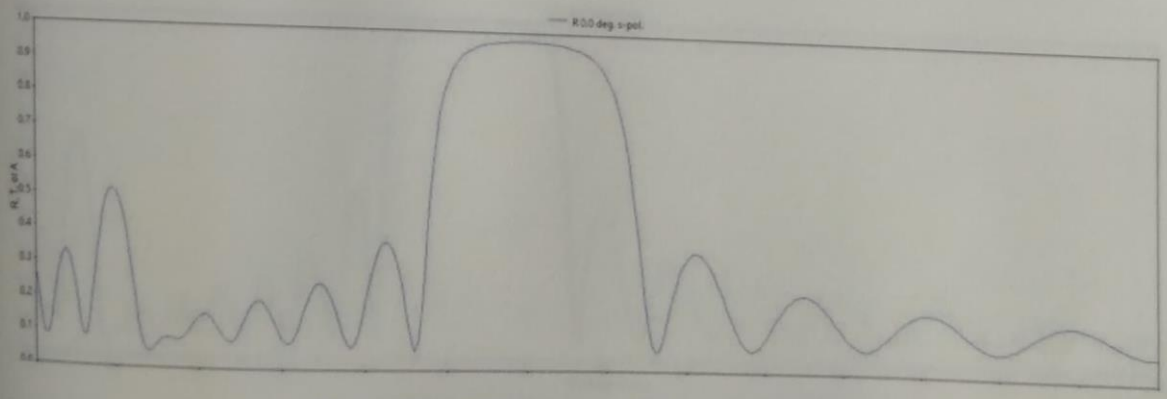

Fig 4.6: The reflectance curve of the stack a/(3H3L)^6|s

Afterwards, the stack layer is designated is a$|(3H3L)^6|$s. The number of layers and front thickness obtained is 12 and 2629.98 nm. The 97.66% of reflectance is obtained which is shown in the above fig 4.6.

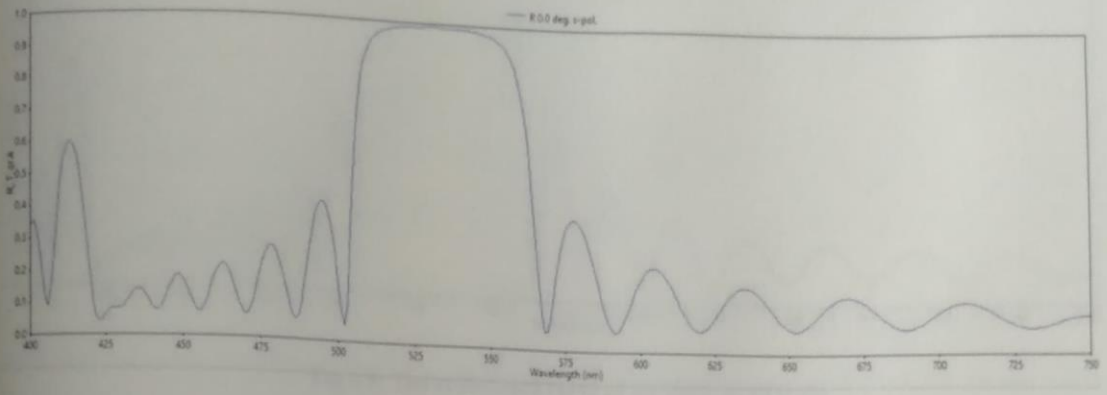

Fig 4.7: The reflectance curve of the stack a|(3H3L)^7|s

Later, the stack layer preferred as a$|(3H3L)^7|$s. Here, the number of layers and thickness is increased to 14 and 3068.31 nm. The above fig 4.7 represents the reflectance curve of a$|(3H3L)^{7}|$s. The maximum reflectance obtained is 99.06%.

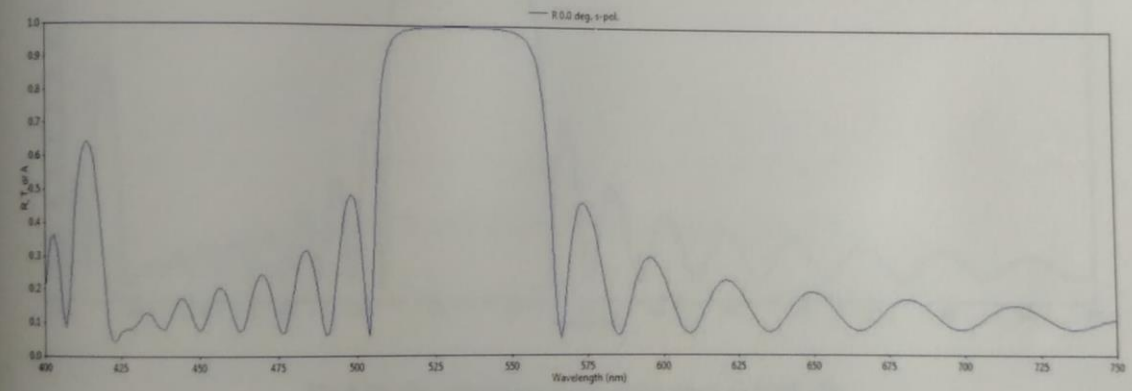

Fig 4.8: The reflectance curve of the stack a|(3H3L)^8|s

Subsequently, the stack layer is favored as a$|(3H3L)^8|$s. In the elevated stack, the number of layers and thickness raised to 16 and 3506.64 nm. The maximum reflectance of 99.62% is obtained which is shown in the fig 4.8.

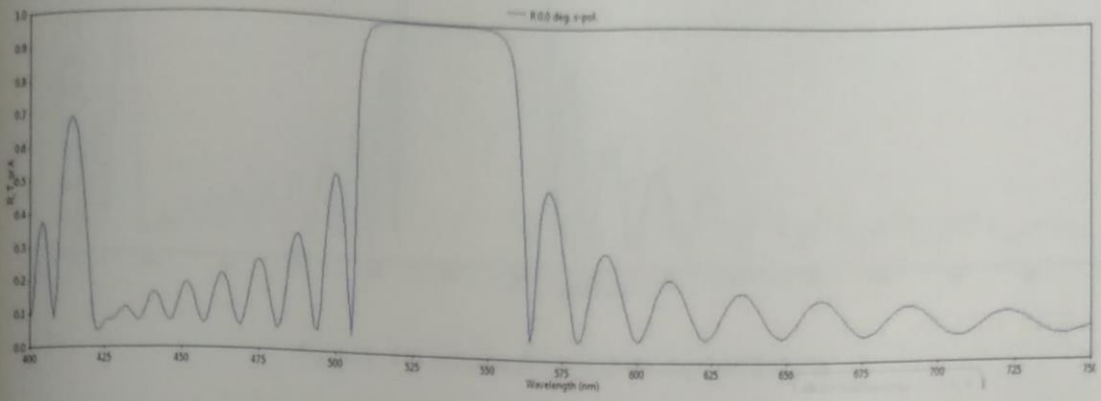

Fig 4.9: The reflectance curve of the stack a|(3H3L)^9|s

The above fig 4.9 plotted for the stack a$|(3H3L)^9|$s.The front thickness and number of layers acquired is 3944.97 nm and 18. 99.84% of reflectance is received from this stack.

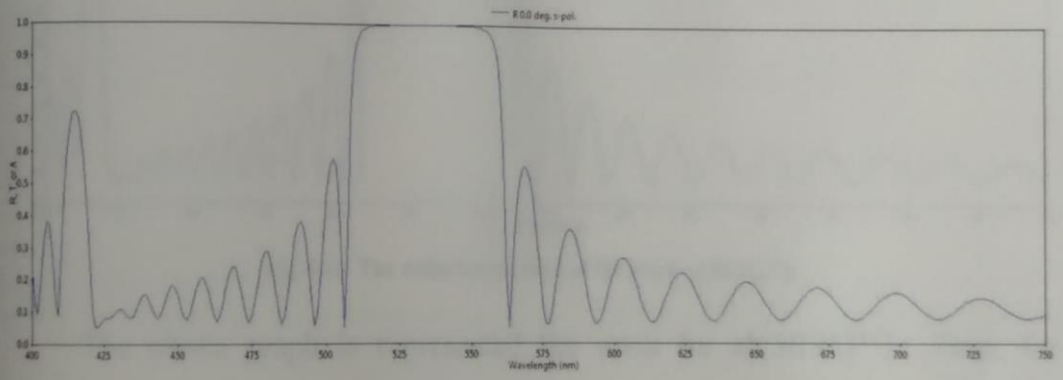

Fig 4.10: the reflectance curve of the stack a|(3H3L)^{10}|s

Stack layer used in the above graph is a$|(3H3L)^{10}|$s. Then the front thickness and the number of layers of this stack is 4383.30 nm and 20. The maximum reflectance obtained in this stack is 99.93% which is shown in the fig 4.10.

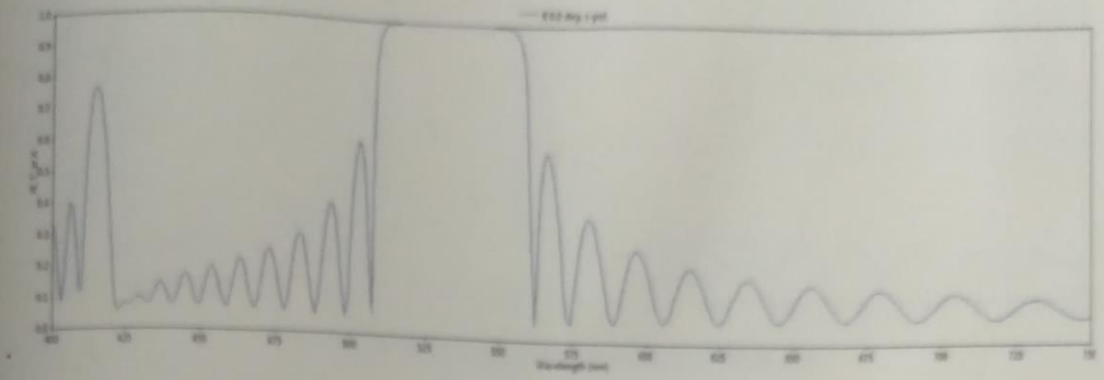

Fig 4.11: The reflectance curve of the stack a|(3H3L)^{11}|s

Then, the stack layer is increased to a$|(3H3L)^{11}|$s. The number of layers and thickness is 22 and 4821.62 nm. The obtained maximum reflectance is 99.97%. The reflectance curve is shown in the fig 4.11.

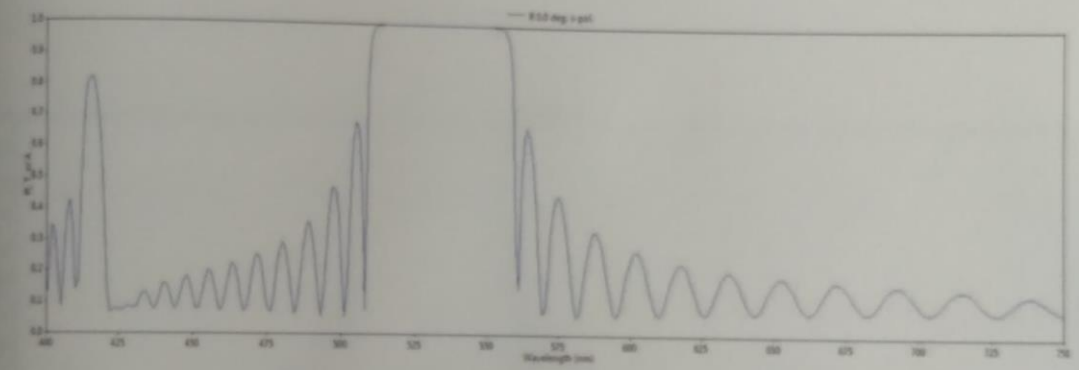

Fig 4.12: The reflectance curve of the stack a|(3H3L)^{12}|s

The above graph is represented the stack for a$|(3H3L)^{12}|$s. Here, the number of layers and thickness attained is 24 and 5259.95 nm. The obtained maximum reflectance is 99.98%.

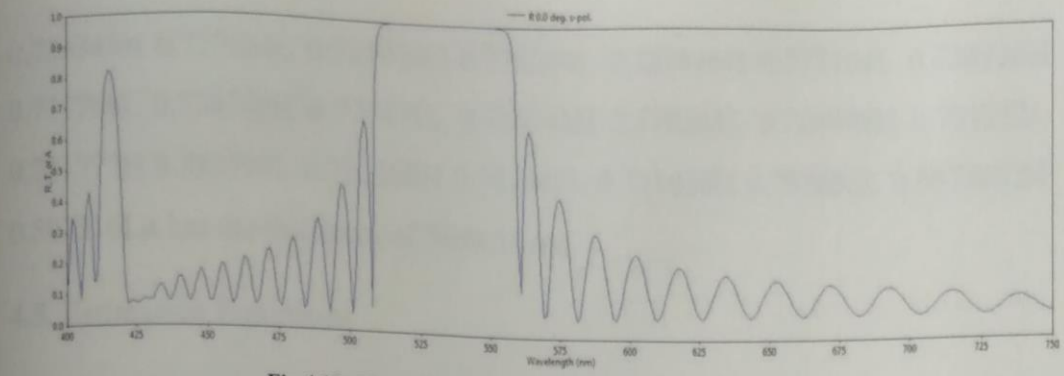

Fig 4.13: The reflectance curve of the stack a|(3H3L)^{13}|s

The stack a|$(3H3L)^{13}$|s offered the maximum reflectance of 99.99% and to be increased the bi-layers as 13.When the stack a|$(3H3L)^{13}$|s, the expected 99.99% reflectance is achieved and the thickness is 5698.28 nm. Fig 4.13 displays the reflectance curve of the conventional stack with the maximum reflectance of 99.99% at the 26th layer.

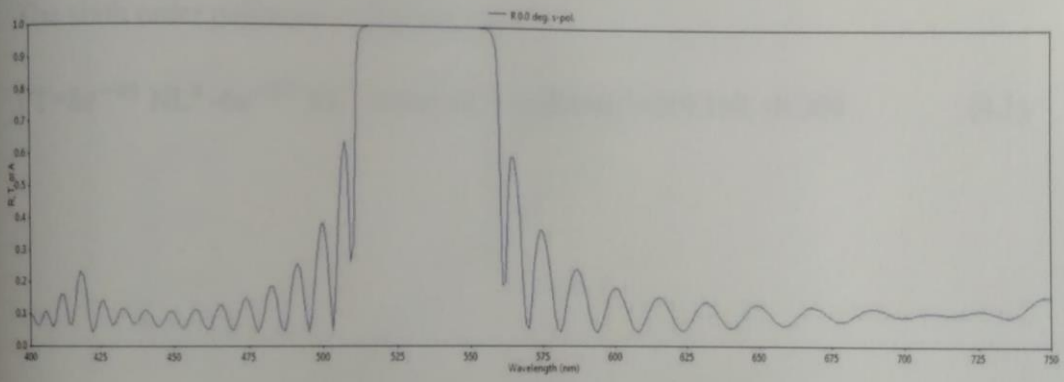

Fig 4.14: The reflectance curve of the stack a|(3H3L)^{14}|s

The ripples are raised on both the sides of the designed wavelength ranges 400-510 and 565-750 nm. These ranges are chosen on the target for optimizing and consequently, reach the final response after 71 iteration. The resulting spectral performance is displayed in the Fig 4.14. The design prescription of the highest reflecting optimized stack is a|0.713675H 0.796114L 0.716113H 0.781546L

0.724345H 0.777624L 0.727706H 0.776250L 0.727846H 0.777104L 0.726936H 0.777798L 0.726758H 0.777471L 0.726751H 0.778344L 0.724498H 0.781232L 0.721777H 0.782599L 0.721166H 0.782965L 0.721036H 0.792852L 0.6872662H 0.597516L|s has the thickness of 5690.51 nm.

4.5. Estimation Equations

4.5.1. Number of Layers Vs Thickness

The important parametric has come into focus here .The number of layers as a function of thickness. The table 4.1 and the figure 4.15 shows how the thickness is increased with the number of layers. The equation is recommended which is relevant to the number of layers and thickness. With the help of this equation, we can find out the physical thickness (PT) for known values of number of layers (NL) using excel software.

The sixth order polynomial follows on,

$$PT=8e^{-09}\ NL^{6}\ -6e^{-07}\ NL^{5}\ -0.000NL^{3}+0.001NL^{2}+219.1NL+0.004 \qquad (4.1)$$

Table 4.1: Thickness for Various Number of Layers

No. of layers	Front thickness (nm)
2	438.33
4	876.66
6	1314.99
8	1753.32
10	2191.65
12	2629.98
14	3068.31
16	3506.64
18	3944.97
20	4383.30
22	4821.62
24	5259.95
26	5698.28

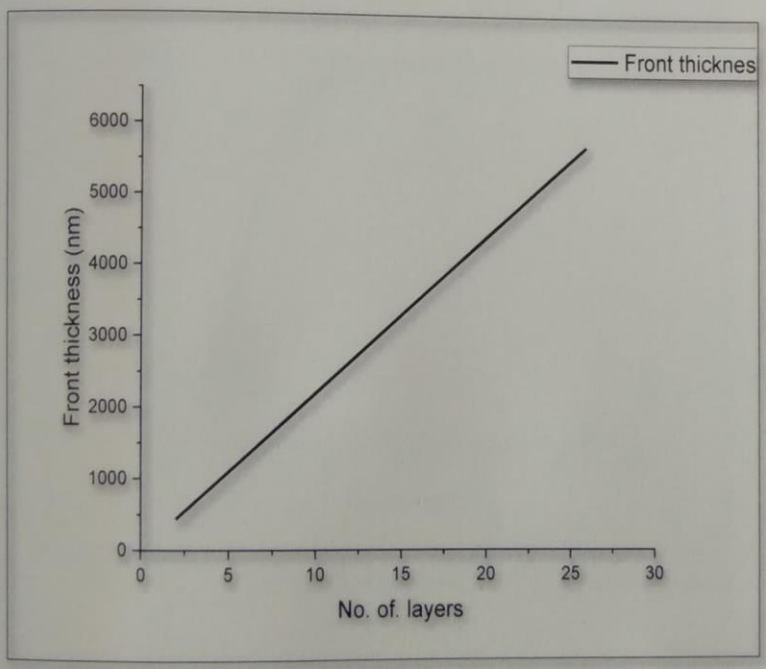

Fig4.15: Thickness for Various Number of Layers

4.5.2. Number of Layers Vs Reflectance

Reflectance mainly depends on number of stack on layers either to increase or decrease. But in this case of minus filter, the reflectance, increases on the number of stack increases. The reflectance equation which are relevant to BK7 substrate for visible region is derived here. It is obvious from the above discussion, the table 4.2 and figure 4.16 is drawn for visible region and it explains the maximum intensity of light reflected in each stack on bi-layers.

The fourth order polynomial for required reflectance for BK7 substrate as follows

$$PT=-0.000NL^4+0.068NL^3-2.129NL^2+28.75NL-41.48 \quad (4.2)$$

TABLE 4.2: Reflectance for Various Number of Layers

No. of layers	Reflectance (%)
2	9.90
4	39.40
6	68.81
8	86.12
10	94.22
12	97.66
14	99.06
16	99.62
18	99.84
20	99.93
22	99.97
24	99.98
26	99.99

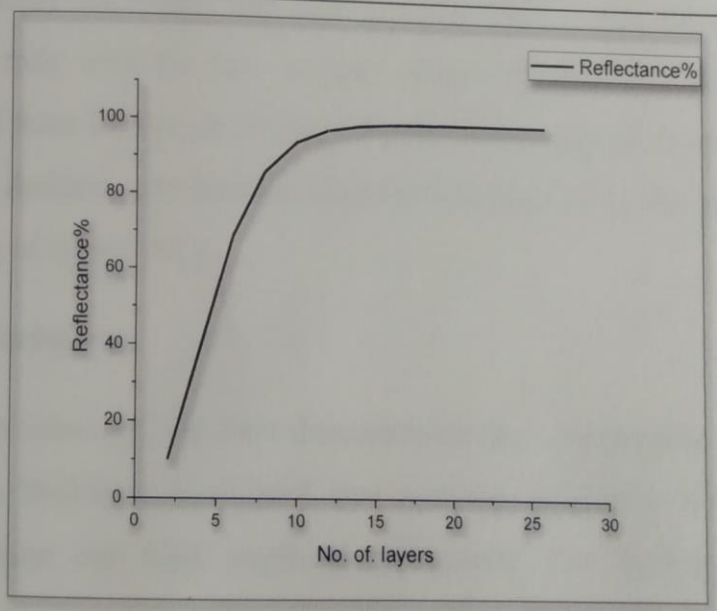

Fig4.16: Reflectance for Various Number of Layers

With the help of these equations we can detect the physical thickness (PT) and reflectance (R) of any stack if the number of layers is known.

CHAPTER V
SUMMARY, CONCLUSION AND FUTURE SCOPE

5.1. Summary

The purpose of this project is to achieve minus filter for green colour display with multilayer structure which consist of dielectric thinfilms. The multilayer minus filter is designed at normal incidence using two different dielectric materials SiO_2 and TiO_2 and BK7 is employed as the substrate in this coating. The optical thickness of each layer is equal to quaterwave thickness at designed wavelength of 533 nm. The chosen bi-layer stack a|3H3L|s is modified by increasing its number of bi-layers to provide 99.99% reflectance. The periodic structure of alternative high and low index materials are designed by $a|(3H3L)^{13}|s$ for minus filter. The achieved design has many ripples on both sides of designed wavelength i.e from 400-510 to 565-750nm this sidelobes are suppressed successfully with the help of open filters software. The binomial equations also derived from the above obtained details. With help of the estimated equations, an optical designer can find the physical thickness (PT) and reflectance (R) for any number of layers (NL).

5.2. Conclusion

In summary, we have demonstrated that it is possible to design minus filters using a thickness modulated two material multilayer with excellent sidelobes suppression and high stopband reflectance. The thickness-modulations follow simple analytical functions based on the matrix theory. Moreover, the entire structure consists of layers that are not too thick or too thin, which is quite suitadle to produce minus filter for green colour displayed.

5.3 Future Scope

A part from the development of green colour, the minus filters for blue, yellow, orange, red etc... can be designed using the same two materials and it would be another area of result.

BIBLIOGRAPHY

[1] www.britannica.com.

[2] https:\\vaccoat.com.

[3] www.corrosionpedia.com

[4] https:\\ecss.n\.com

[5] https://www.rp-photonics.com.

[6] Jinlong Zhang, Yujiang xie, xinbin Cheng, Hongfei Jiao, and Zhanshan Wang, Thin-flim thickness-modulated designs for optical minus filter, Applied optics, vol.52,No.23,10 August 2013.

[7] www.vedantu.com.

[8] www.science direct.com.

[9] www.corrosionpedia.com.

[10] www.science direct.com

[11] Jinlog zhang, Yujiang xie, xinbin cheng, Hongfei Jiao, and zhanshan wang,Thin-flim thickness-modulated designs for optical minus filter, Applied optics, vol.52,No.23,10 August 2013,www.refractive index

[12] https://en.m.wikipedia.org.

[13] https://matericon.com.

[14] https://knowledge.ulprospector.com

[15] https://matericon.com.

[16]https://www.glassdynamics//c.com.

[17]Stephane Larouche & Ludvik Martinu 2008, 'Openfilters: open–source software for the design, optimisation, and synthesis of optical filter's, Applied Optics, vol.47, no.13, pp.C219-C230.

[18]Basu, A 2007, 'Anomaly in optical thickness monitoring of a quarterwave thin film multilayer stack – Its cause and how to avoid it', Indian Journal of Pure & applied Physics, vol.45, no.11, pp.920-925.

ARNIM – DELTA WING LIGHT WEIGHT FLYER UTILISING PORTABLE WIFI

PROJECT REPORT

submitted to the Department of Physics

ST.MARY'S COLLEGE (AUTONOMOUS), THOOTHUKUDI.

affiliated to **MANONMANIAM SUNDARANAR UNIVERSITY TIRUNELVELI,** in partial fulfilment of requirements for an award of,

BACHELOR'S DEGREE IN PHYSICS

BY

P. INFANT GRACY SONA – 20AUPH07

P. MARIA ESTHER THERASA – 20AUPH16

A. MARY MIRACULIN – 20AUPH19

S. V. SHUNMUGAPRIYA – 20AUPH32

K. THARANEYA – 20AUPH38

N. VARSHA – 20AUPH40

Guidance and supervision by

Ms. A. VALENTINA M.Sc., M.Phil.,

DEPARTMENT OF PHYSICS

St. Mary's College (Autonomous), Thoothukudi – 1

(Re-Accredited with "A+" grade)

2022-2023

CERTIFICATE

This is to certify that this project work entitled, **"ARNIM – DELTA WING LIGHT WEIGHT FLYER UTILISING PORTABLE WIFI"** is submitted to St. Mary's College (Autonomous), Thoothukudi in partial fulfilment for the award of Bachelor's Degree in Physics and is a record work done during the year 2022 – 2023 by the following students

P. INFANT GRACY SONA	– 20AUPH07
P. MARIA ESTHER THERASA	– 20AUPH16
A. MARY MIRACULIN	– 20AUPH19
S. V. SHUNMUGAPRIYA	– 20AUPH32
K. THARANEYA	– 20AUPH38
N. VARSHA	– 20AUPH40

3/4/2023
GUIDE

HEAD OF THE DEPARTMENT
HEAD
Department of Physics,
St. Mary's College (Autonomous),
Thoothukudi - 628 001.

13/4/23
EXAMINER

Lucia Rose
PRINCIPAL
St. Mary's College (Autonomous)
Thoothukudi - 628 001.

DECLARATION

We hereby declare that the project, **"ARNIM – DELTA WING LIGHT WEIGHT FLYER UTILISING PORTABLE WIFI"** is submitted to St. Mary's College (Autonomous), Thoothukudi, affiliated to Manonmaniam Sundaranar University, for the Bachelor's Degree of Science in Physics is our original work and that, it has not previously formed the basis for the award of any Degree, Diploma, or similar title.

P. INFANT GRACY SONA	– 20AUPH07
P. MARIA ESTHER THERASA	– 20AUPH16
A. MARY MIRACULIN	– 20AUPH19
S. V. SHUNMUGAPRIYA	– 20AUPH32
K. THARANEYA	– 20AUPH38
N. VARSHA	– 20AUPH40

Station: Thoothukudi

Date: 03.04.2023

ACKNOWLEDGEMENT

"No man is an island"

This project has seen the light due to the efforts of many people who have dedicated their time, energy, and talent at our disposal. we extend our heartfelt thanks to them.

Firstly, we thank God almighty for his impregnable blessings and continuous guidance at each step of this project.

We wish to extend our heartful thanks to our respected principal **Dr. Sr. A. S. J. Lucia Rose M.Sc., PGDCA, M.Phil., Ph.D.,** St. Mary's College (Autonomous), Thoothukudi, for providing us this wonderful opportunity.

We owe our special gratitude to **Dr. Sr. Jessie Fernando M.Sc., M.Phil., Ph.D.,** Head of the department of Physics for her continuous encouragement and support.

We express our sincere gratitude to our guide **Ms. A. Valentina M.Sc., M.Phil.,** for her inspiring guidance and scholarly suggestion that helped us greatly in the completion of this project.

We extend our sincere gratitude to the Department of Physics, St. Mary's College (Autonomous), Thoothukudi, for providing us a lab space and many other facilities for our field test. We also wish to thank the lab assistant / non-teaching staffs for coordinating with us and supporting us throughout this project.

"All glory to the God"

CONTENTS

CHAPTER – I

CHAPTER - I

1.1 INTRODUCTION

A glider is a fixed-winged aircraft that is supported in flight by the dynamic reaction of the air against its lifting surfaces, and whose free flight does not depend on an engine. Gliders are planes without motor. They have four forces acting on them –lift, weight (gravity), drag and thrust. Although gliders do not have their own power to provide thrust the weight of the glider produces the thrust to keep it moving through the air by flying downwards at a shallow angle of decent. Gliders are principally used for the air sports of gliding, hang gliding and paragliding. However, some spacecrafts have been designed to descend as gliders and in the past military gliders have been used in warfare. Some simple and familiar types of gliders are toys such as paper planes and balsa wood gliders. **DELTA WING**-It is a wing shaped in the form of a triangle. It is named because its similarity in shape to the Greek uppercase letter Δ The delta wing is commonly used for high-speed airplane. The delta wing has a large angle of rearward sweep and for this reason the wing's leading edge will not contact the shockwave boundary formed at the nose of the fuselage as the speed of the aircraft approaches and exceeds transonic to supersonic speed. The delta wing has the advantage of a large sweep angle but also greater wing area than a simple swept wing compensates for the loss of lift usually experienced in sweepback. It is naturally stable in pitch; therefore, it does not require a separate tail surface. It can be used to survey remote areas in which humans cannot enter. A camera can be fixed in this glider to take pictures of the environment in those remote areas. Delta wings have a long root chord and therefore can have a thick main spar while retaining a low thickness to chord ratio. They have larger wing area than trapezoidal wings with the same aspect ratio. The long root chord of the delta wing and minimal structure outboard make it structurally efficient. It can be built stronger, stiffer and at the same time lighter than a swept wing of equivalent lifting capability. Thus, delta wing offers advantages such as structural integrity, high speed and low speed flight.

1.2 AIM OF THE PROJECT

- To study the working of the delta wing.
- To analyse the delta wing glider from its miniature model.
- To customize the plane design.
- To construct a circuit with ESP8266 and upload the command firmware to control the glider in Wi-Fi mode.

CHAPTER – II

CHAPTER - II

2.1 LITERATURE REVIEW

Igor Skawinski, Tomasz Goetzendorf-Grabowski [1]: - FDM 3D printing method utility assessment in small RC aircraft design. The purpose of this paper is to investigate the possibility of manufacturing fused deposition modeling (FDM) 3D printed structures such as wings or fuselages for small remote control (RC) aircraft and mini unmanned aerial vehicles (UAVs). Material tests, design assumptions and calculations were verified by designing and manufacturing a radio-controlled motor-glider using as many printed parts as possible and performing test flights. It is possible to create an aircraft with good flight characteristics using FDM 3D printed parts. The paper proves that apart from currently popular small RC aircraft structural materials such as composites, wood and foam, there is also printed plastic. Moreover, 3D printing is highly competitive in some aspects such as first unit production time or production cost. The presented manufacturing technique can be useful for quick and cost-effective creating scale prototypes of the aircraft for performing test flights.

Fadilah M Zain, M Shahrieel M Aras [2]: - Design and development of an underwater glider, using remote control. The underwater glider was driven depending on buoyancy adjustment of itself and move horizontally wing. This glider was designed by using a buoyancy control to make the glider become float and using a hydrodynamic concept. The main part of this is, an underwater glider consists of wings, tail, receiver and transmitter board, DC motor, fan and remote control. This glider was controlled by using radio frequency (RF) with 4 channels. The RC will control the movement of a glider and the DC motor will be used to rotate the fan. However, DC motor spins too fast and has too little torque to drive the loads. Thus, gear reduction is required to slow down the rotational speed and increases the torque of the motors.

Gregory D Miller, Charles HK Williamson [3]: - In the present study, we investigate the near- and far-wake instabilities in the wake of a delta wing with a view to understanding the basic instabilities, mixing, and decay rate of

the wake. Extensive visualization of the wake as a delta wing glides in free flight through water reveals a "braid wake" between the primary vortex pair and shows it imposing its structure on the primary pair. Hot-wire measurements of the fluctuating velocity in the immediate near wake not only demonstrate the periodic shedding of the spanwise vortices in this "braid wake," but also reveal a low-frequency oscillation nearer to the core of each primary vortex. The subsequent evolution of the wake is remarkable, as the scales of disturbances grow in what appear to be almost discrete steps, until a large-scale instability of the primary pair develops into a sequence of large-scale interconnecting vortex loops. Ultimately, the appearance is like a series of vortex rings. The streamwise wavelength of the ring-like structure was measured for these free-flight tests and for tests with the wing towed through water at a variety of speeds and angles of attack, yielding a wavelength between 4 and 5 spans (intervortex spacing of the primary pair). Further investigation is required before the relation of these results to theoretical analyses can be ascertained. Experiments in which the incident velocity is perturbed at selected wavelength and amplitude reveal that the wavelength of the final structure is reasonably insensitive to either parameter unless the forcing becomes as large as 5% of free-stream velocity, provided the forcing wavelength is far from the natural wavelength. While investigating the vertical mixing of the fluid due to the descending vortices, we found that the vertical extent of mixing is surprisingly large owing to the formation of a "curtain" of vortical fluid left above the descending vortex pair.

LE Ericsson, HHC King [4]: - Effect on leading-edge geometry on delta wing unsteady aerodynamics. The complexity of the flow field on aircraft and air-craft like configurations at high angles of attack prohibits the use of numerical computational methods for preliminary design. Also because of the continual changes in the early design, a purely experimental method cannot be used. One needs rapid computational methods to guide the early stages of preliminary design until a firmer design has evolved on which experimental and numerical methods can be applied. The simple flow concept developed by Pplhamus, 1 (i.e.), the leading-edge suction analogy, was used in Ref. 2 as a starting point in the development of a fast prediction method for the unsteady aerodynamics of sharp-edged delta wings.

William Chana [5]: - World's first delta wing airplane convair/air force XF-92A. The first flight of a delta wing air craft took place in the United States at the Muroc AFB Flight Test Center on 18th September 1948. The aircraft, Convair No. 7002, Air Force S/N 46-682 and designated the XF-92A was piloted by Convair's Manager of Flight Research, ED "Sam" Shannon. The author witnessed this historic flight as a Flight Test Engineer on the project. Studies and wind tunnel tests for a supersonic interceptor were conducted at the Vultee Division of Consolidated Vultee Aircraft Corporation (Convair) in 1945. These studies led to the selection of the 60-delta wing plan form. This paper reviews the major differences between the thin wing XF-92A and the thick wing DM-1 glider (never flown) designed by Alexander M. Lippisch in Germany at the close of the World War II.

Gareth J Dyke, RL Nudds, JMV Ryner [6[: - The 225-million-year-old reptile *Sharovipteryx mirabilis* was the world's first delta-winged glider; this remarkable animal had a flight surface composed entirely of a hind-limb membrane. We use standard delta-wing aerodynamics to reconstruct the flight of *S. mirabilis* demonstrating that wing shape could have been controlled simply by protraction of the femora at the knees, and by variation in incidence of a small forelimb canard. Our method has allowed us to address the question of how identifying realistic glide performance can be used to set limits on aerodynamic design in this small animal. Our novel interpretation of the bizarre flight mode of *S. mirabilis* is the first based directly on interpretation of the fossil itself and the first grounded in aerodynamics.

Ahmed Osama Mahgoub, Luca Cortelezzi [7]: - introduced the idea of numerical characterization of the vortex flow and aerodynamic performance of a reverse delta wing. They stimulated numerically the unsteady flow past a reverse delta wing to characterize the structure of the vortical flow and associated unsteady phenomena, and quantify the impact of such structures on the aerodynamic performance. They established a clear relationship between the vorticity and pressure fields. Their estimates of the aerodynamic forces generated by a reverse delta wing agree with and extend the experimental results by Dr. Lok Sun Ko and Prof. Timothy Lee. They showed and confirmed that the lift-to-drag ratio of a delta wing and a reverse delta wing was, surprisingly, about the same.

Anan Lu, Timothy Lee [8]: - introduced the idea of passive wingtip vortex control by using tip-mounted half delta wings in ground effect. The ground effect on the wingtip vortex generated by a rectangular semi wing equipped with tip-mounted regular and reverse half delta wings was investigated experimentally. The passive tip vortex control always led to a reduced lift-induced drag as the ground was approached. In close ground proximity, the presence of the corotating ground vortex (GV) added vorticity to the tip of the vortex while the counter-rotating secondary vortex (SV) negated its vorticity level. The interaction of the GV and SV with the tip vortex and their impact on the lift-induced drag were discussed. Physical mechanisms responsible for the change in the vortex flow properties in ground effect were also provided.

B. Yaniktepe and D. Rockwell [9]: - introduced the topic of flow structure on a delta wing of low sweep angle. The instantaneous and averaged flow structure past delta wing of low sweep angle was investigated using a technique of high-image-density particle image velocimetry. Control in the form of a small amplitude perturbation of the wing, at a frequency corresponding to the sub harmonic of the spectral component in the initial region of development of the separated layer, can restabilize the time-averaged patterns of streamline topology and vorticity, such that they resemble those occurring at lower angle of attack α. Investigations on averaged and unsteady structure on delta wings having relatively large sweep angle, served as a basis for interpretation of the flow structure on wings of moderate sweep angle. The onset of stall from the surface of the wing can also be a function of Reynold's number.

Ilya Bashiera Hamizi, Sher Afghan Khan [10]: - Aerodynamics investigation of delta wing at low Reynold's Number. A numerical simulation had been carried out to investigate the aerodynamics of an oscillating delta wing and to evaluate the flow structure over the leading edge at different low Reynold's numbers. Effects of Reynold's number and angle of attack is investigated for the wing lift coefficient, and the aerodynamic efficiency. Pressure contour and turbulence kinetic energy were also observed for each case. Vortex formation from each case was noted from pressure content and lift coefficient. The stall condition was also observed. The lift on sharp leading-edged delta wing was insensitive for the low Reynold's number from

the range of 80,000 and 200,000 for static condition, so it was easier to predict the flow characteristics of a Micro Air Vehicle (MAV) that was not always using the same power source which affects the MAV velocity. But the C_{LMAX} for each case of Reynold's number showed some increment. The aerodynamic efficiency also increased marginally. The higher turbulent kinetic energy for each Reynold's number increment showed that the vortex energy is stronger as Reynold's number increased.

Hiromitsu KAWAZOE and Susumu KATO [11]: - Effects of leading-edge separation vortex of flexible structure delta wing on its aerodynamic characteristics. The aerodynamic forces and moments of a flexible delta wing in pitching motion were experimentally studied in a low-speed wind tunnel. Three types of flexible delta wing were investigated, the flexible parts of which were 44, 70 and 99% of the delta wing. Aerodynamic characteristics were different among the three types of flexible and completely hard delta wing is the key factor for determining the leading-edge vortex on the upper side of the wing and the pressure distribution on the windward side. Lift, drag and pitching moment formed a hysteresis loop with an angle of attack in pitching motion, particularly in a region with a large attack angle, accompanied by leading edge vortex breakdown. The flow of visualization of leading-edge vortices was also carried out to explain the dynamic characteristics of the delta wings. The dynamic characteristics of the flexible delta wing in pitching motion besides under stable conditions were experimentally investigated by comparing them with those of the hard delta wing. The total effects of the leading-edge vortex formed above the delta wing and the pressure distribution on the windward side of the winding-up flexible delta wing determined the characteristics of the flexible delta wing. The winding up of the leading edge of the delta wing at small angle of attack made the leading edge vortex strong and produced a high Cl and a high Cd.

Rowan Eveline Muir, Abel Arredondo-Galeana, Ignazio Maria Viola [12]: - The leading-edge vortex of swift wing-shaped delta wings. In this investigation, a model non-slender delta shaped wing with a sharp leading edge is tested at low Reynold's number, along with a delta wing of the same design, but with a modified trailing edge inspired by the wing of a common swift Apus. The effect of the tapering swift wing on LEV development and

stability is compared with the flow structure over the unmodified delta wing model or triple LEV is recorded on a swift wing-shaped delta wing, where such a system is found across all tested conditions. It is shown that the spanwise location of LEV breakdown is governed by the local chord rather than Reynold's number or angle of attack. These findings suggest that the trailing-edge geometry of the swift wing alone does not prevent the common swift from generating an LEV system comparable with that of a delta-shaped wing.

John W Paulson [13]: - He did the investigation of low-subsonic flight characteristics of a model of a hypersonic boost-glide configuration having a 78-degree delta wing. This paper was published by National Aeronautics and Space Administration. It was an investigation of the low-subsonic stability and control characteristics of a model of a flat bottom hypersonic boost-glide configuration having 78 sweep of the leading edge had been made in the Langley full-scale tunnel. The model was flown over an angle of attack range from 10 to 35. Static and dynamic force tests were made in the Langley free-flight tunnel.

Masanobu Nagata, Makoto Kumon, Ryuichi Kouzawa, Ikuro Mizumoto, Zenta Iwai [14]: - Automatic flight path control of small unmanned aircraft with delta wing ICCAS 2004. It is known that an aircraft with delta wings which are attached to the body at a large angle like a kite or a hang glider has a measure of maneuverability and stability. Aircrafts of this kind can fly stably. Even if engine trouble occurs, it will not fall and might be able to land. In this paper, one of the conventional control methods, PID control, is applied to the aircraft with LQ local control block. This is based on an idea that the aircraft flies so stably that the automatic control system might be realized by a simple controller. The proposed PID controller consists of several sub-controllers which are constructed to each system neglecting the interference. In addition, the LQ control is involved as a local loop of the aileron and rudder control in order to increase stability of the altitude when circling. The effectiveness of the proposed method is shown through 3D computer simulations and experiments of the flight path control.

N Rigamonti, H Pflugshaupt [15]: - They did the investigation of the steady state behavior of two delta wing hang gliders. Investigations were reported for the flight behavior of two full size hang gliders in the 7*5 low speed wind tunnel. Flight characteristics at small angles of attack and the influence of the pilot's position in the swing seat were explored. In addition to showing the aerodynamic coefficients in modes of representation designed specifically for these craft, the relative safeties of the Delta-Plane and Chandelle Competition 16 are compared. The latter proves to be more stable and tends to enter a luffing dive more readily.

Andrey A Sidorenko, Alexey D Budovskiy, Anatoly A Maslov, Boris V Postnikov, Boris Yu Zanin, Ilya D Zverkov, Victor V Kozlov [16]: - The flow over a delta wing at high angles of attacks is characterized by the presence of two large scale primary vortices on the leeward side of the wing. These vortices contribute substantially to lift production at high angles of attack. Therefore, vortex breakdown, which can be induced by unfavorable pressure gradients or free stream disturbances, can lead to an abrupt decrease in lift and to the emergence of the roll moment. Thus, the possibility of vortex flow control can be very useful. The problem of vortex flow control was investigated experimentally under subsonic flow parameters in the range of wing chord-based Reynold's number (0.14, 0.25) $*10^6$. A dielectric barrier discharge (DBD) was used as an active control actuator. The data obtained by means of oil flow and smoke flow visualization, surface pressure measurements, and using a particle image velocimetry technique show that the DBD can provoke early vortex bursting. Under certain conditions (discharge excitation mode and frequency), flow excitation by the discharge actuator was found to result in vortex stabilization.

AA Pashilkar [17]: - A new aerodynamic modeling approach was proposed for the longitudinal static characteristics of a simple delta wing. It captured the static variation of normal force and pitching moment characteristics throughout the angle of attack range. The pressure model was based on parameterizing the surface pressure distribution on a simple delta wing. The model was then extended to a wing/body combination where body-alone data were also available. The model was shown to be simple and consistent with experimental data. The pressure model can be used as a first approximation

for the load estimation on the delta wing at high angles of attack. The modeling structure was seen to be simple and physical. A good match had been shown with the experimental data for a 60◦ delta wing and wing/body combination. The estimated parameters show close, though not exact values, as compared with the experimental data. The physical nature of the model ensures that all the estimated parameters were plausible. The initial results of the model were encouraging, indicating that there was scope to further improve the model. Extension to model unsteady aerodynamic pressures was a possibility.

Bandu Pamadi, Dhanvada Rao, T Niranjana [18]: - Wing rock and roll attractor of delta wings at high angles of attack. This paper deals with wing rock and roll phenomena wings at high angles of attack. The wing rock of an 80 deg. delta wing with and without passive aerodynamic devices was to explore the feasibility of suppressing wing rock. Vie free to roll response of a 60-deg. wing exhibited existence of multiple role attractors. A generic aircraft model fitted with this 60-deg. delta wing, exhibited wing rock. A simple one degree of freedom mathematical model using measured nonlinear static rolling moment coefficient and a constant roll damping coefficient has been developed which successfully predicts the multiple roll attractors of present 60 deg. delta wing and that of 65 deg. delta wing of previous studies at a=30deg.

Asha Crasta, SA Khan [19]: - Oscillating Supersonic delta wing with Straight Leading Edges. A supersonic similitude had been used to obtain stability derivatives in pitch and roll of a delta wing with straight leading edge for the attached shocked case. Ghosh's strip had been used in which strips at different span wise locations were independent of each other. This combined with the similitude to give a piston theory which gives the closed form of solution to stability derivatives in pitch and roll. Some of the results obtained had been compared with those of Hui et al, Ghosh and Lui & Hui. Results had been obtained for supersonic flow of perfect gas over a wide range of Mach numbers, incidences and sweep angles.

Shuxing Chen, Chao Yi [20]: - Global solutions for supersonic flow past a delta wing. In this paper we study the mathematical aspects of supersonic flow

past a delta wing. The flow was described by the potential flow equation, and the delta wing is assumed to be a triangular plate or a triangular wing with specific thickness. In the self-similar coordinates, the problem could be reduced to a boundary value problem of a nonlinear degenerate elliptic equation with a free boundary. By constructing a nonlinear iteration scheme and applying the Schauder fixed point theorem, we prove the existence of a solution to this problem, provided that the incident angle of the oncoming flow was less than a critical value determined by the data.

CHAPTER – III

CHAPTER - III

METHODOLOGY

3.1 CIRCUIT DIAGRAM

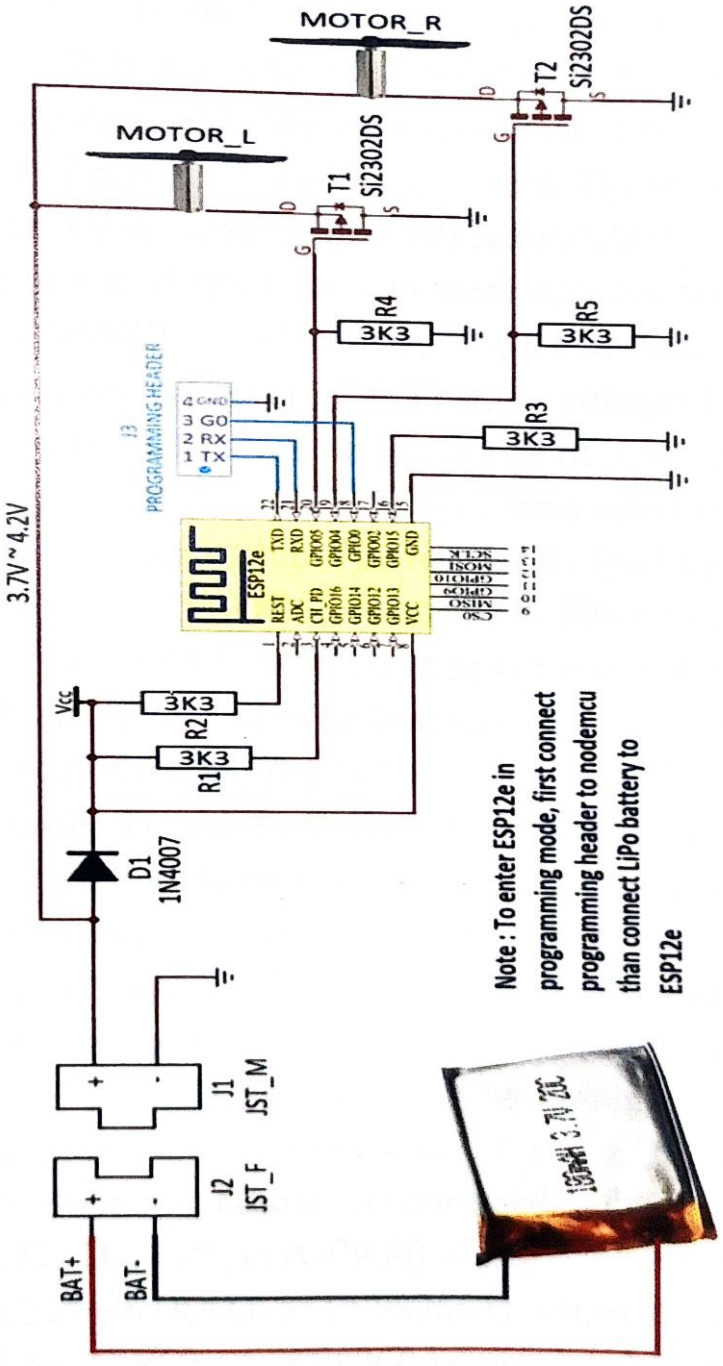

3.2 CIRCUIT EXPLANATION

The lipo battery which is capable of 130mAH 3.7V 20C is connected to the ESP12e/ ESP8266 Wi-Fi SoC controls the RPM of left and right motor and measures the battery voltage and RSSI of Wi-Fi signal and sends it to Android App, through JST connector. The JST connector consists of a female (JST-FJ_2) and male connector (JST-MJ_1). The lipo battery's positive end is connected to the positive of the female (JST-FJ_2) JST connected and the negative end of lipo battery is connected to the negative of the female JST connector and that is connected to the male connector. The negative end of the male (JST-M) J_2 JST connector is given to ground. The positive end of the female JST connector is connected to the ESP12e module through a IN4007 diode D1. Since the power of lipo battery is more than the capability of the ESP12e module, D_1 (IN4007) is used as a step-down converter. It reduces the circuit weight and complexity and drops the battery voltage(4.2V~3.7V) by 0.7V (cut in voltage of IN4007) to get voltage range of 3.5V~3.0V, which is used as supply voltage of ESP8266/ESP12e. The three resistors (3.3k Ω) are required for ESP8266 minimum setup. The resistor R_1 (pull up) is connected to the 3rd pin (CH-PN[EN]) of ESP8266, to enable it. The resistor R_2 (pull up) is connected to the 1st pin (REST) which is at active low and brings it out of reset mode. The 16th pin GPIO15 must be low, so as to connect the resistor R_3 to pull down GPIO15 of ESP8266. The 19th (GPIO04) and 20th (GPIO05) pins are connected to mosfet T_1 and T_2 through the resistors R_4 and R_5 (3.3k (3.3kΩ). The resistors R_4 and R_5 are used to pull down the gate of T_1 and T_2 (mosfets) in order to avoid any false trigger of mosfets (motor run) when ESP8266 is power up. [T_1 and T_2 -2.5 Amp rating, controls RPM of left and right motor by PWM coming from GPIO04 and GPIO05 of ESP8266]. In the mosfets, the 'G' pin is connected to the ESP8266 through the resistors, the 'D' pins are connected to the L-motor and R-motor, and 'S' pins are connected to the ground. J_3 (programming header) is connected to the ESP8266 through the pins 18, 21 and 22. The 18th pin (GPIO0) of ESP8266 is connected to the 3rd pin J_3 (GO). The 21st pin (RXD) of ESP8266 is connected to the 2nd pin in J_3 (RX_). The 22nd pin (TXD) of ESP8266 is connected to the 1st pin in J_3 (TX). The 4th pin in the J_3 (programming Header) is connected to the ground.

The other end of the resistors R_3, R_4 and R_5 are connected to the ground. The 15^{th} pin (GND) of ESP8266 is connected to ground. From the diode D_1 a wire is given to the 8^{th} pin (Vcc) of the ESP8266. The other end of the resistors R_2 is connected to Vcc. The ESP12e based WI-FI receiver module is connected to the computer via NodeMC. [Here we use a microprocessor to give the commands to the ESP12e module]. [Note: The resistors are used to bring the floating current to reset. The diode IN4007 is used as a replacement for a step-down Transformer in order to reduce the weight of the circuit.

3.3 GLIDER DESIGN

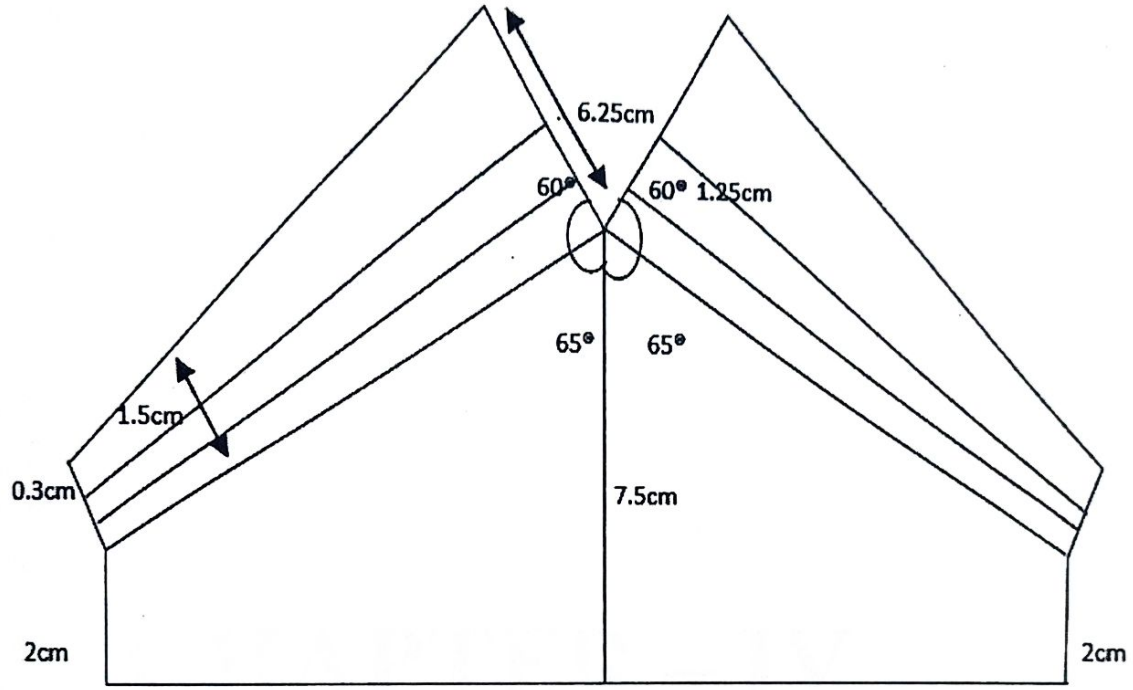

CHAPTER – IV

CHAPTER - IV

4.1 COMPONENTS LIST/ MATERIALS REQUIRED

- IN4007 Diode.
- ESP12E Soc Module.
- TP4056 Lipo Battery Charger.
- 3.7 V 180mAH 20C Lipo Battery.
- 3.3K ohm 1/10 Watt SMD.
- SOT-23 MOSFET.
- Coreless DC Motor with CW and CCW Propeller.
- JST Connector
- Flight Controller App (Android version 8)

4.2 COMPONENTS DESCRIPTION

IN 4007 DIODE:

It is a rectifier diode, with module plastic case, which is used to convert AC to DC. It passes current up to 1A. Its peak inverse voltage (PIV) is about 1000V. It has high current capability and low forward voltage drop.

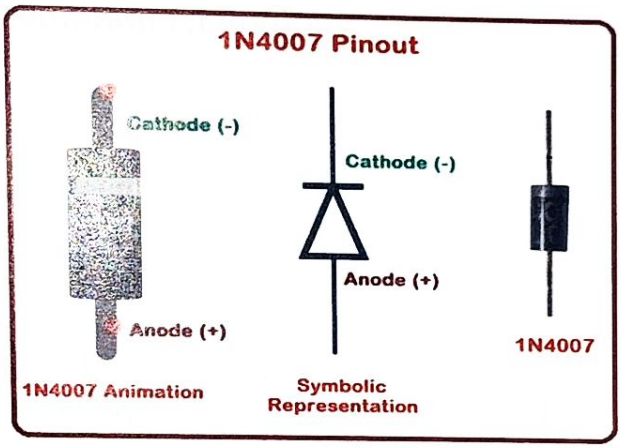

IN4007 stands for:

- 1N: Single Junction Semiconductor.
- 2N: Double Junction Semiconductor.
- '1' stands for 1 Junction.
- 'N' stands for semiconductor.
- '4007' stands for identification number of that diode.

FEATURES:

- Average forward current is up to 1A.
- Non-repetitive peak current is 30A (Maximum Current).
- Reverse current is 5μA.
- Peak repetitive reverse voltage is 1000V (Maximum Voltage).

IN4007 EQIVALENT DIODES:

IN4148, IN4733A, IN5408, IN5822, Zener Diode.

ESP12 SOC MODULE:

ESP-12 module is a miniature Wi-Fi module, which is used for establishing a wireless network connection for microcontroller or processor. The core of ESP-12E is ESP8266EX, which is a high integration wireless SoC (System on Chip). It is a low power consumption of the UART-Wi-Fi module and ultra power consumption technology.

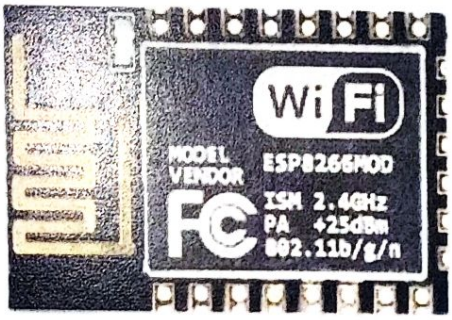

FEATURES:

- WS2812 Led on board
- 802.11 b/g/n
- Wi-Fi Direct (P2P), soft-AP
- Integrated TCP/IP protocol stack
- Integrated TR switch, balun, LNA, power amplifier and matching network
- Integrated PLL, regulators, DXCO and power management units
- +19.5dBm output power in 802.11b mode
- Power down leakage current of <10μA
- Integrated low power 32-bit CPU could be used as an application processor
- Sdio 1.1/2.0, SPI, UART
- STBC, 1*1 MIMO, 2*1 MIMO
- A-MPDU & A-MSDU aggregation & 0.4ms guard interval

TP4056 LIPO BATTERY CHARGER:

- An easy way to use battery charger chip.
- Charging current from 130mA to 1A

LIPO BATTERY:

A lithium-polymer battery (LiPo) is a rechargeable battery that, in the case of true LiPo, uses solid polymer for the electrolyte and lithium for one of the electrodes. Commercially available LiPo are hybrids: gel polymer or liquid electrolyte in a pouch format, more accurately termed a lithium-ion polymer battery.

The main advantages of LiPo battery cells are that they have about four times the energy of density of nickel cadmium or nickel metal hydride batteries. LiPo batteries are very lightweight and pliable, and can be made to almost any size or shape.

LIPO BATTERY CHARGER:

A LiPo battery charger is a handy piece of hardware that allows us to our battery's charging needs. The most important thing that this charger offers is balance charging. A balance charger has a balance connector slot in addition to the main power connectors.

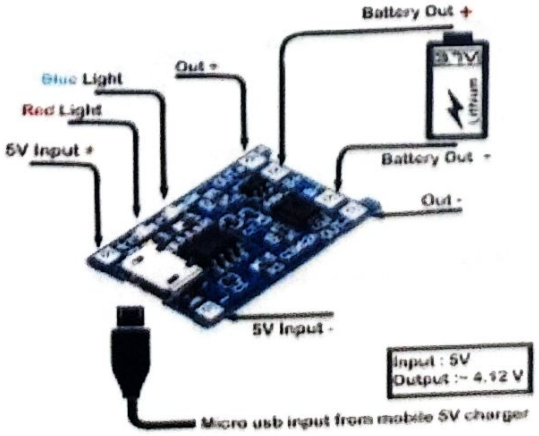

The TP4056 chip is a lithium-ion battery charger for a single cell battery, protecting the cell from over and under charging. It has two status outputs indicating charging in progress, and charging complete. It also has a programmable charge current of up to 1A.

There are two types of common breakout boards for this chip:

- One with only the charger chip on board.
- One with three chips on board.

FEATURES:

- Constant Current / Constant voltage charging method.
- C / 10 Charge termination.
- 2.9V trickle charge threshold (for deeply discharged batteries).
- Upper charge stop voltage: 4.2V.
- Soft start inrush current limit.
- Automatic recharge (keeps optimally charged when connected to a charger).

3.7 V 180mAH 20C LIPO BATTERY:

3.7V 180mAH (Lithium Polymer) Lipo Rechargeable Battery also known as Lipo or Lipo batteries are thin and powerful. This battery has the capacity of 150mah. These Batteries are widely used in GPS, Mobile Backup Power Supply, Bluetooth Speaker, IOT and other DIY and industrial applications, laptop battery packs, telephones, electronic cigarettes, flashlights and cordless power tools.

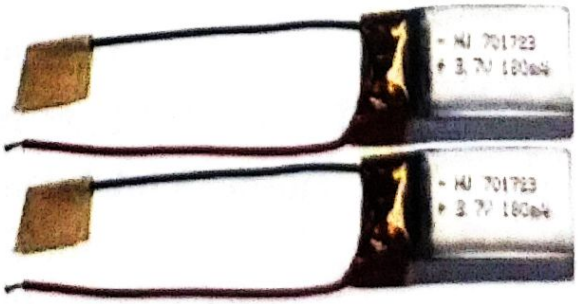

20C on a LiPo battery: The 'C' in C rating stands for capacity. The C rating is the maximum, safe, continuous discharge rate of a pack as specified by the manufacturer, so when it is seen 20C printed on the label, it means it can be discharged at 20 times the pack's capacity, "continuously". A battery that has a higher C rating delivers more energy, and that means higher performance.

The safest charge rate for most LiPo batteries is 1C, 1 * capacity of battery in Amps.

3.3KOHMS 1/10 WATT SMD:

A resistor is a passive two-terminal electrical component that implements electrical resistance as a circuit element. In electronic circuits, resistors are used to reduce current flow, adjust signal levels, to divide voltages, bias active elements, and terminate transmission lines, among other uses. High-power resistors that dissipate many watts of electrical power as heat, may be used as part of motor controls, in power distribution systems, or as test loads for generators. This product is known as 3.3kOhm, 3.3kOhm Resistor 0603 package, 3.3k Ohm SMD Resistor, 3.3kOhm 0603 Package Resistor, 3.3kOhm 0603 package and 3.3k Resistor 0603 package.

FEATURES/SPECS:

- Manufacturer: YAEGO
- Manufacturer Part No: RC0603FR-073K3L
- Product Type: Thick Film Resistors
- Resistance: 3.3kOhms
- Power Rating: 100mW (1/10 W)
- Voltage Rating: 75 V
- Tolerance: + or – 1%

- Temperature Coefficient: 100 PPM/®C
- Minimum Operating Temperature: -55®C
- Maximum Operating Temperature: +155®C
- Mounting Style: PCB Mount
- Case Code – in: 0603
- Case Code – mm: 1608

APPLICATIONS:

- ❖ Automotive
- ❖ Telecommunication
- ❖ Medical Equipment
- ❖ Industrial Equipment

SOT-23 MOSFET:

It is a voltage controlled small signal switch. It is rugged and reliable. It has high saturation current capability.

SI2302DS N-channel enhancement mode field-effect transistor in a plastic package using TrenchMOS™ technology.

FEATURES:

SI2302DS SI2302 A2SHB SOT23 Triode SOT23-3 SMD transistor N-Channel 1.25-W, 2.5-V MOSFET

- Type of transistor: MOSFET
- Type of control channel: N-Channel
- Maximum power dissipation (Pd): 1.25 W
- Maximum drain-source voltage |Vds|: 20V
- Maximum gate-source voltage |Vgs|: 8V

- Maximum gate-threshold voltage |Vgs(th)|: 1.2V
- Maximum drain current |Id|: 2.3 A
- Maximum Junction temperature (Tj): 150®C
- Rise Time (tr): 36 ns
- Drain-Source Capacitance (Cd): 115 pF
- Maximum drain-source on-state resistance (Rds): 0.085 Ohm
- High density cell design for low RDS(ON)
- Voltage controlled small signal switch
- Rugged and reliable
- High saturation current capability
- TrenchMOS™ technology
- Very fast switching
- Logic level compatible
- Subminiature surface mount package

APPLICATIONS:

- Battery management
- High speed switch
- Low power DC to DC convertor.

CORELESS DC MOTOR WITH CW AND CCW PROPELLER:

CORELESS MOTOR:

A coreless motor is a brushless or brushed motor with a coil wound on itself and not on iron. For this reason, it is also called ironless. It does away with the iron core in the rotor. Instead, the rotor windings are wound in a skewed, or honeycomb fashion to form a self-supporting hollow cylinder. The stator magnet sits inside the coreless rotor.

Coreless motors are classified by rotor shapes as cylindrical or disc. cylindrical rotors are further divided into those containing inside fields or outside fields.

FEATURES:

615 magnetic micro coreless motor with red and the blue wire is CW rotation motor and black and the white wire is CCW rotation motor.

- 615 coreless motor is high speed and low torque motor.
- Less noisy operation.
- Offers low resistance.
- They are equipped with high-quality magnets.
- This coreless motor supports 1S battery.

Major advantages of coreless motors include very low inertia, low mechanical time constant, and high efficiency. Because the core is ironless, its low mass allows more rapid acceleration and deceleration than any other class of DC motor.

JST CONNECTORS:

JST connectors are electrical connectors manufactured to the design standards originally developed by J.S.T. Mfg. Co. (Japan Solderless Terminal). JST manufactures numerous series (families) and pitches (pin-to-pin distance) of connectors.

JST connectors are used in many types of products, and commonly used by electronics hobbyists and consumer products for rechargeable battery packs, battery balancers, battery eliminator circuits, 3D printers, and radio-controlled servos.

This is a simple two wire polarized cable. It is of great use for jumping from board to board or just about anything else. There is a 2-pin JST connector on one end, bare cable on the opposite end.

This is a pack of two 20cm wires: one with a female 2-pin JST-type connector and one with a male 2-pin JST-type connector. The pin pitch in the connectors is 2mm and the cables are 24 AWG.

They are perfect for battery, LEDs, and board-to-board connections.

FEATURES:

- Two 20mm length cables, 24 AWG, with female and male connector.
- 2mm pitch pins.
- Red and black wires.
- 100mm helicopter lipo battery plug JST connector.
- Can be used on most mini-RC helicopter and indoor 3D plane.
- Great for small Lipo and NiMh connections.

Package includes 1 * 100mm JST male and female cable.

FLIGHT CONTROLLER APP:

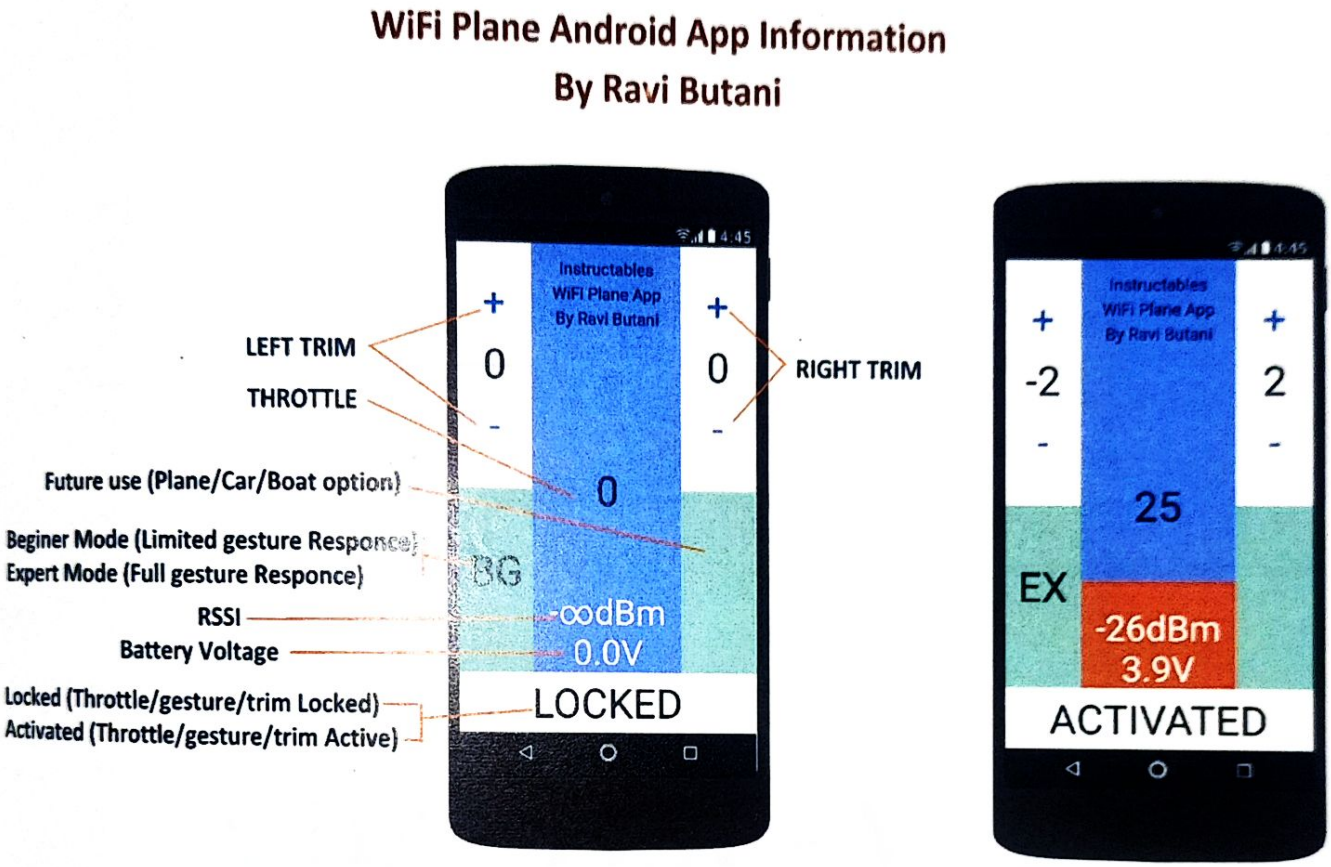

- This application is suitable for android version 8 only.
- There are two modes of controls, they are

  Beginner mode

  Expert mode.
- The app displays the voltage source in volts and the frequency of the motor.
- They have a feature which enables the users to lock the signal from the device to the ESP12e and thereby stopping the rotation of motor.

CHAPTER – V

CHAPTER - V

5.1 ESP8266 FIRMWARE CODE

```
/******************
// WiFi Controlled Tiny Airplane
//******************
#include <ESP8266WiFi.h>
#include <WiFiUdp.h>


#define P_ID 1
#define ST_LED  2
#define L_MOTOR 5
#define R_MOTOR 4
#define DC_RSSI 1500 // Time in mS for send RSSI
#define DC_RX   900   // Time in mS for tx inactivity 200 old problem of motor stopping flickring
ADC_MODE(ADC_VCC);
unsigned int l_speed = 0;
unsigned int r_speed = 0;


unsigned long premillis_rssi = 0;
unsigned long premillis_rx   = 0;


int status = WL_IDLE_STATUS;
char ssid[] = "Nagarajan";  // your network SSID (name)
```

```
char pass[] = "kuwait2017";   // your network password (use for WPA, or use as key for WEP)
int keyIndex = 0;             // your network key Index number (needed only for WEP)
IPAddress remotIp;
unsigned int localPort = 6000;      // local port to listen on
unsigned int remotPort = 2390;      // local port to talk on
char  packetBuffer[10]; //buffer to hold incoming packet
char  replyBuffer[]={P_ID,0x01,0x01,0x00}; // a string to send back
WiFiUDP Udp;

// the setup function runs once when you press reset or power the board
void setup() {
 WiFi.mode(WIFI_STA);
 //WiFi.setOutputPower(2.5);
 analogWriteRange(255);
 pinMode(L_MOTOR, OUTPUT);
 pinMode(R_MOTOR, OUTPUT);
 analogWrite(L_MOTOR,0);
 analogWrite(R_MOTOR,0);
 pinMode(ST_LED, OUTPUT);
 digitalWrite(ST_LED,HIGH);
 Serial.begin(115200);
 WiFi.begin(ssid, pass);
 while (WiFi.status() != WL_CONNECTED)
```

```
  {
   digitalWrite(ST_LED,LOW);
   delay(60);
   digitalWrite(ST_LED,HIGH);
   delay(1000);
   Serial.print(".");
  }
  remotIp=WiFi.localIP();
  remotIp[3] = 255;
  Udp.begin(localPort);
}

// the loop function runs over and over again forever
void loop() {
  delay(5);
  if(WiFi.status() == WL_CONNECTED)
  {
   digitalWrite(ST_LED,LOW);
   // if there's data available, read a packet
   int packetSize = Udp.parsePacket();
   if (packetSize)
   {
    // read the packet into packetBufffer
    int len = Udp.read(packetBuffer, 10);
```

```
if (len > 2)
{
 if(packetBuffer[0] == P_ID)
 {
  l_speed = (unsigned int)packetBuffer[1]*2-2;
  r_speed = (unsigned int)packetBuffer[2]*2-2;
  Serial.print(l_speed);
  Serial.print(" \t");
  Serial.println(r_speed);
  analogWrite(L_MOTOR,l_speed);
  analogWrite(R_MOTOR,r_speed);
  premillis_rx = millis();
 }
}

}
if(millis()-premillis_rssi > DC_RSSI)
{
 premillis_rssi = millis();
 long rssi = abs(WiFi.RSSI());
 float vcc = (((float)ESP.getVcc()/(float)1024.0)+0.75f)*10;
 replyBuffer[1] = (unsigned char)rssi;
 replyBuffer[2] = (unsigned char)vcc;
```

```
 Udp.beginPacket(remotIp, remotPort);
 Udp.write(replyBuffer);
 Udp.endPacket();
}
if(millis()-premillis_rx > DC_RX)
{
  analogWrite(L_MOTOR,0);
  analogWrite(R_MOTOR,0);
  Serial.println("nodata");
 }
}
else
{
  digitalWrite(ST_LED,LOW);
  delay(60);
  digitalWrite(ST_LED,HIGH);
  delay(1000);
  analogWrite(L_MOTOR,0);
  analogWrite(R_MOTOR,0);
  digitalWrite(ST_LED,HIGH);
 }
 }
```

CHAPTER – VI

CHAPTER - VI

6.1 WORKING

- Using Arduino IDE, the microprocessor, ESP12E firmware is developed.
- The firmware is uploaded using a NodeMCU method to ESP12e.
- Here we can use the NodeMCU alone to build a circuit but to reduce the weight we are using the ESP12e.
- Once the firmware is ready, we can upload it to the SOC module Wi-Fi.
- Now we set the Wi-Fi network – android hotspot.
- After connecting the ESP12e to the android's Wi-Fi we are ready to fly the glider.
- Here in this circuit the MOSFETS are the one which control the rpm of the motors.
- The motors whose ends are connected to MOSFETS and positive terminal of the batteries receive its command signal from the android device which in turn receive its signal from ESP12e SOC Module.
- By learning the control techniques of the flight app, we can make the glider fly in the sky.

CHAPTER – VII

CHAPTER - VII

7.1 CONCLUSION

Hereby we conclude that DELTA Wing Glider named ARNIM, is used for surveillance purposes in oil and gas pipes, power stations, railway tracks, sewage system by some additional setup like cameras, gas sensors, thermos sensors etc. It is one of the advanced growing technologies which helps mankind to achieve his/her deeds in critical and harsh situations. The future developments of this glider include attachments of cameras, gas sensor, navigation sensor, thermo detectors etc.....Using this glider we can inspect large power plant tower, gas pipeline which cannot be performed by human with his potential, especially during time of night. The limitation of this model is that it contains lift induced drag, greater internal impedance in MOSFETs may mislead the command signal from the app.

CHAPTER – VIII

CHAPTER - VIII

8.1 BIBLIOGRAPHY

[1] https://www.emerald.com/insight/content/doi/10.1108/AEAT-07-20180189/full/html

[2]https://scholar.google.com/scholar?hl=en&as_sdt=0%2C5&q=RC+glider&oq=#d=gs_qabs&t=1676129698492&u=%23p%3DJlqCQ6CZztYJ

[3]https://scholar.google.com/scholar?hi=en&as_sdt=0%2C5&q=delta+wing+glider&oq=#d=gs_qabs&t=1676818154373&u=%23p%3DtCHaiiMjkX0J

[4]https://scholar.google.com/scholar?hl=en&as_sdt=0%2C5&q=delta+wing+glider&oq=#d=gs_qabs&t=1676818189040&u=%23p%3DLnuECWQXPd8J

[5]https://scholar.google.com/scholar?hl=en&as_sdt=0%2C5&q=delta+wing+glider&oq=#d=gs_qabs&t=1676818204191&u=%23p%3DPz30kaj-HmsJ

[6]https://scholar.google.com/scholar?hl=en&as_sdt=0%2C5&q=delta+wing+glider&oq=#d=gs_qabs&t=1676818283190&u=%23p%3DdUtQRNVLvdkJ

[7]https://doi.org/10.2514/1.J058021

[8]https://asmedigitalcollection.asme.org/fluidsengineering/article-abstract/142/2/02/201/960572/passive-wingtip-Vortex-Control-by-Using-Tip?redirectedFrom=fulltext

[9]https://arc.aiaa.org/doi/10.2514/1.1207

[10]https://www.academia.edu/70354144/Aerodynamics_investigation_of_delta_wing_at_low_Reynold_snumber

[11]https://www.jstage.jst.go.jp/article/jsmeb/49/4/49_4_1049/_pdf

[12]https://www.researchgate.net/publication/319281137_The_leading-edge_vortex_of_swift_wing-shaped_delta_wings

[13]https://apps.dtic.mill/sti/citations/AD0255532

[14]https://scienceon.kisti.re.kr/srch/selectPORSrchArticle.do?cn=NPAP08127135&SITE=CLICK

[15]https://scholar.google.com/scholar?hl=en&as_sdt=0%2C5&q=investigation+of+the+steady+state+behavior+of+two+delta+wing+hang+gliders.+&btnGt=#d=gs_qabs&t=1679034882395&u=%23p%3DQG0WlfTnot0J

[16]https://scholar.google.com/scholar?hl=en&as_sdt=0%2C5&q=The+flow+over+a+delta+wing+at+high+angles+of+attacks+is+characterized+by+the+presence+of+two+large+scale+primary+vortices+wing.+&btnG=#d=gs_qabs&t=1679035061092&u=%23p%3Db8M-jR8Va-QJ

[17]https://scholar.google.com/scholar?hl=en&as_sdt=0%2C5&q=AA+pashillkar%2C+2001%3A-
+A+new+aerodynamic+modeling+approach+was+proposed+for+the+longitudinal+static+characteristics+of+a+simple+delta+wing.+&btnG=#d=gs_qabs&t=1679035220863&u=%23p%3DS8GxJaHpEzMJ

[18]https://scholar.goggle.com/scholar?hl=en&as_sdt=0%2C5&q=Wing+rock+and+roll+attractor+of+delta+wings+at+high+angles+of+attack.+&btnG=

[19]https://scholar.google.com/scholar?hl=en&as_sdt=0%2C5&q=Oscillaing+Supersonic+delta+wing+with+Straight+Leading+Edges.+&btnG=

[20]https://scholar.google.com/scholar?hl=en&as_sdt=0%2C5&q=Global+solutions+for+supersonic+flow+past+a+delta+wing.+btnG=

STUDY OF ACOUSTICAL PARAMETERS OF ETHYL PROPIONATE WITH n-PROPANOL USING ULTRASONIC TECHNIQUE

Project report submitted to St. Mary's College (Autonomous), Thoothukudi affiliated to Manonmaniam Sundaranar University, Tirunelveli, in partial fulfilment of the requirement for the award of

BACHELOR'S DEGREE IN PHYSICS

By

G. Jaisla - 20AUPH08

M. Maria Disniya - 20AUPH16

P. Segupriya - 20AUPH29

A. Sheela Varsha - 20AUPH31

L. Siva Nandhini - 20AUPH34

Under the Guidance of

DR.S. EUCHRISTA IMMACULATE SYLVIA, M.Sc.,M.Phil.,Ph.D.,

Department of Physics

ST. MARY'S COLLEGE (AUTONOMOUS)

Reaccredited with "A+" Grade by NAAC

Thoothukudi.

2022-2023

CERTIFICATE

This is to certify that this project work entitled, "STUDY OF ACOUSTICAL PARAMETERS OF ETHYL PROPIONATE WITH n-PROPANOL" is submitted to St. Mary's College (Autonomous), Thoothukudi, in partial fulfilment for the award of Bachelor's Degree in Physics and is a record of work done during the year 2022-2023 by the following students.

G. Jaisla	-	20AUPH08
M. Maria Disniya	-	20AUPH15
S. Segupriya	-	20AUPH29
A. Sheela Varsha	-	20AUPH31
L. Siva Nandhini	-	20AUPH34

S. Eucharista Emmaculate

GUIDE

HEAD OF THE DEPARTMENT

HEAD
Department of Physics,
St. Mary's College (Autonomous),
Thoothukudi - 628 001.

13/4/23

EXAMINER

Lucia Rose

PRINCIPAL

St. Mary's College (Autonomous)
Thoothukudi - 628 001.

ACKNOWLEDGEMENT

First, we thank to The Almighty God for His blessings which carried us through these days.

Our special thanks to our principal Rev. Sr. Dr. A. S. J. Lucia Rose M.Sc., M.Phil., Ph.D., PGDCA., who provided necessary facilities in the institution for carrying out our project work.

We express our sincere gratitude to our head of the department Rev. Sr. Dr. Jessie Fernando M.Sc., M.Phil., Ph.D., who offered constant support for completing the project.

It gives immense pleasure to express our deep sense of thanks and gratitude to our guide Dr. Mrs. S. Euchrista Immaculate Sylvia M.Sc., M.Phil., Ph.D., for her encouragement and constant support in bringing out this project work well.

We are highly indebted to thank Mrs. P. Padmavathi M.Sc., M.Phil., SET for her guidance and constant support in every stage of our project.

We are thankful to the star college scheme sponsored by DBT, New Delhi for providing all the facilities to carry on the project work successfully.

We are thankful to all our department professors and supportive staff for their constant support.

We are also thankful to our parents and everyone else who have helped us directly and indirectly to bring out this project successfully.

DECLARATION

We hereby declare that the project entitled, "STUDY OF ACOUSTICAL PARAMETERS OF ETHYL PROPIONATE WITH n-PROPANOL" submitted to St. Mary's College (Autonomous), Thoothukudi, affiliated to Manonmaniam Sundaranar University, for the Bachelor's Degree of Science in Physics is our original work and that, it has not previously formed the basis for the award of any Degree, Diploma or similar title.

G. Jaisla	-	20AUPH08
M. Maria Disniya	-	20AUPH15
P. Segupriya	-	20AUPH29
A. Sheela Varsha	-	20AUPH31
L. Siva Nandhini	-	20AUPH34

Station: Thoothukudi

Date: 03.04.2023

CHAPTER-I

INTRODUCTION:-

Ultrasonic method has wide applications in molecular interactions of liquid mixture. The studies of physiochemical behavior and molecular interactions in a variety of liquid mixture are helpful to know about the thermodynamic and acoustical properties. In recent years, many research have been made in the field of physical acoustics and ultrasound on solids, liquids and gases [9,17,21]. Excess parameters are relatively more insightful to the molecular interactions than the thermodynamic properties. Thermodynamic properties provide great knowledge concerning mass transport and fluid flow. Ultrasonic propagation parameters have been found to provide information regarding the behavior of binary liquid system because intermolecular association, dipolar interactions, complex formation and related structural changes affect the compressibility of the system which in turn produces corresponding variations in the ultrasonic velocity. Ultrasonic velocity is used to determine the nature of molecular interaction between the liquid mixture constituents [10,14,15]. The study of molecular interactions plays an important role in the development of molecular science. However, during the last forty years there has been a considerable importance and a number of experimental techniques have been used to investigate the interactions between the components of the binary liquid mixtures [20]. Ultrasonic velocity determined by the interferometer method is considered as more reliable and precise as compared to other methods. Thermodynamic property of liquid mixture finds extensive application in industrial processes. Industries like photochemical, dye and pharmaceutical widely consider the molecular interactions of polar and non-polar component of the liquid mixture [3,5]. Ultrasonic measurements are very useful in chemical, food processing, underwater ranging and cleaning and they are commonly employed in mechanical machinery of materials, preparation of colloids or emulsions and imaging of biological tissues [12].

Considering, the varied applications of ultrasonic studies we designed this project using Ethyl propionate with n-propanol to carry out the acoustical study of parameters. Ethyl propionate appear as clear colorless liquid with a pineapple like odor. It is a propanoate ester of ethanol. It has a role of metabolite. It is used in perfumery and fragrance. It is used to manufacture various propionates which is used in reduction of pharmaceuticals, antifungal agents, agrochemicals, plastics, plasticizers, rubber chemicals, dyes, artificial flavors, and perfumery synthesis. It is used as a solvent and in nickel-electroplating solutions. (PubChem release).

1-propanol appear as a clear colorless liquid with a sharp musty odor like rubbing alcohol. It is used in making cosmetics, skin and hair preparations, pharmaceuticals, perfumes, lacquer formations, dye solutions, antifreezes, soaps, window cleaners and other chemical products. Vapors are heavier than air and mildly irritate the eyes, nose and throat. (PubChem release)

OBJECTIVES:

Taking into account the significant reasons for the study of acoustic parameters, we carried out the project with the following objectives.

1. To determine the ultrasonic velocity (U) of the experimental mixtures of different concentrations.
2. To determine the density (ρ) of the experimental mixtures.
3. To determine the coefficient of viscosity (η)of the experimental mixtures.
4. To calculate the values of derived parameters such as Adiabatic compressibility(β_a), Free length(L_f), Relaxation time(τ), Acoustic impedance(Z) and Ultrasonic attenuation(α/f^2).

CHAPTER-II

REVIEW OF LITERATURE:

Mrs. Monika Dhiman *et al* (2020) have studied the excess acoustical and thermo dynamical parameters of binary solutions of polypropylene glycol-400 and n-alkanols at 303 K. The values of excess ultrasonic velocity(U^E), excess acoustic impedance(Z^E), excess intermolecular free length (L_f^E) and excess internal pressure(π_i^E) were evaluated.The effect of the increasing size of the alkyl group of alkanols based on the molecular interactions has also been discussed.

Mr. Edward Jeyakumar *et al* (2020) have studied the liquid-liquid interactions in 2-Nitroanisole, 1-Pentanol in n-Hexane at various temperature with constant frequency of 2MHz.From the measured values of ultrasonic velocity(U), the acoustical parameters such as Acoustic Impedance (Z), Intermolecular free length (L_f), Adiabatic compressibility(β_a) have been calculated.

Mr. S. Bahadur Alisha *et al* (2018) have studied the excess ultrasonic velocity(U^E), Intermolecular free length (L_f^E), Acoustic impedance(Z) on Binary Liquid mixtures of Benzene with Carbitols at 308.15 K. The results were discussed in terms of the existence of intermolecular interactions between the components in the liquid mixture.

Mr. Manoj Kumar Praharaj *et al* (2017) have studied the ultrasonic and conductometric studies of aqueous Potassium Chloride solutions at different temperature at 4MHz frequency. The experimental data have been used for study of the molecular interaction in the different solutions using different parameters such as Adiabatic compressibility(β_a), Intermolecular free length (L_f), Acoustic impedance(Z) and Relaxation time (τ).

Mrs. K. Vijayalakshmi (2016) has studied the Ultrasonic velocity(U) on Binary Liquid mixtures of methyl acrylate with 2-Alkoxy Ethanols at 308.15 K . The parameters such as Acoustic impedance(Z), Intermolecular free length (L_f),were calculated.The various excess properties like Excess ultrasonic velocity(U^E), Excess acoustic impedance(Z^E), Excess intermolecular free length(L_f^E) were also calculated.

Mr. K. Kaur and K. C. Juglan (2016) have measured the viscosity, density and ultrasonic velocity of binary liquid mixtures of ethyl acetate and hexane at constant temperature of 292 K at frequency of 2MHz using ultrasonic interferometer. The experimental values were used to determine acoustic parameter such as Acoustic impedance(Z), Adiabatic compressibility(β_a), Intermolecular free length (L_f) and Internal pressure(π_i) and ultrasonic attenuation (α/f^2), free volume, Gibb's free energy and enthalpy has been calculated.

Mr. Jitindra Gupta (2014) have studied the ion solvent interactions of glucose in water-methanol and ethanol based on ultrasonic technique. From this experiment Isotropic compressibility, Intermolecular free length (L_f) and several parameters were calculated.

Mr. A. Raguraman *et al* (2014) have studied the molecular interactions of 1,3,4-Pyrazoline derivatives using ultrasonic technique at 303.15 K. From the measured values of Ultrasonic velocity(U), Density(ρ), Viscosity (η) the acoustical parameters such as Adiabatic compressibility(β_a), Intermolecular free length (L_f), Acoustic impedance(Z), Internal pressure(π_i) have been discussed in terms of molecular interactions.

Mr. B. Nagarjun *et al* (2013) have studied the thermodynamic and acoustic based on molecular interactions in certain Binary liquid systems involving Ethyl benzoate. The acoustical parameters such as Adiabatic compressibility(Z), Intermolecular free length (L_f), Molar volume have been computed.

Mr. R. Kumar *et al* (2013) have studied molecular interactions of antibiotic doxycycline hycalte based on ultrasonic technique. The parameters such as Adiabatic compressibility(β_a), Acoustic impedance(Z), Intermolecular free length (L_f) have been evaluated.

Mr. R. K. Shukla *et al* (2013) have studied the ultrasonic interactions of some ligands and its metal complexes. The value of apparent molar volume, Acoustic Impedance(Z), Adiabatic compressibility(β_a), Intermolecular free length (L_f) were computed. The results have been analyzed and interpreted in terms of molecular interactions.

Mrs. Amara Jyothi Koppula *et al* (2012) have studied the densities and ultrasound velocities in γ-Butyrolactone and aliphatic ester at temperature of 303.15 K to 313.15 K. The ultrasonic velocity(U), density (ρ), viscosity (η) were used to calculate the acoustical parameters.

Mr. S. Nithiyanantham *et al* (2012) have studied the acoustical studies on Fructose with enzyme amylase in aqueous media at 298.15 K. From the measured value of ultrasonic velocity (U), density (ρ) and viscosity (η) acoustical parameters such as Acoustical Impedance(Z), Relaxation time (τ), Adiabatic compressibility(β_a), Excess free length (L_f^E), Excess free volume and Internal Pressure(π_i) have been calculated.

Mrs. B. Tanuja *et al* (2012) have studied the intermolecular interactions in binary mixtures of 4- methoxy benzoin with various solvents such as ethanol, chloroform, acetonitrile, benzene, di-oxane at 298 K using ultrasonic technique. Acoustical parameters such as Adiabatic compressibility (β_a), Intermolecular Free length (L_f) and Acoustic impedance were measured. These parameters were used to study the nature and extent of intermolecular interactions between component molecule in binary mixture.

Mr. A. G. Peshwe *et al* (2012) studied the ultrasonic velocity on 1,4-dioxane and methanol binary liquid mixtures at different temperature using ultrasonic interferometer. The acoustical parameter such as Intermolecular free length (L_f), Acoustical impedance(Z), Excess intermolecular free length were computed.

Mr. Elangovan Sampandam *et al* (2012) have studied the ultrasonic velocity in mixtures of ethyl formate and n-alcohols in carbon tetra chloride using ultrasonic interferometer. Acoustical parameter such as Adiabatic compressibility(β_a), Acoustic impedance(Z), Relaxation time(τ), Intermolecular free length (L_f), Intermolecular free volume and internal pressure(π_i) were calculated.

Mr. Saneel K. Thakur *et al* (2011) have studied the acoustical behavior of drug climax in aqueous mixture of methanol at 25℃. From the experimental values the acoustical parameters such as Acoustic impedance(Z), Adiabatic compressibility(β_a) and Intermolecular free length (L_f) were estimated. The results were analyzed and interpreted in terms of molecular interactions.

Mr. K. Raju *et al* (2011) have studied the molecular interactions of ethyl cellulose in n-Alkane at various temperature of 303 K, 313 K, 323 K using ultrasonic technique. The acoustical parameter such as Adiabatic compressibility(β_a), Intermolecular free length(L_f) and Internal pressure(π_i) have been calculated.

Mrs. T. Sumathi *et al* (2011) have studied molecular interactions in ternary liquid system by ultrasonic technique at various temperature of 303.15 K 308 K, 313 K. From the experimental values the acoustical parameter such Adiabatic compressibility (β_a), Intermolecular free length (L_f), Relaxation time(τ) and Internal pressure (π_i) were computed.

CHAPTER-III

MATERIALS AND METHODS:

The knowledge of thermodynamic and transport properties of liquid mixtures is useful in industrial processes. Ultrasonic and viscometric parameters offer simple, easy and accurate ways for calculating several physical parameters which throw light on molecular interactions in solutions. Many engineering problems require quantitative data of the viscosity and density of the liquid mixtures.

This project deals with the experimental study of ultrasonic velocity, density and viscosity in liquid mixture at room temperature. It deals with a detailed study of ultrasonic velocity in liquid mixtures of Ethyl propionate with 1-propanol for different concentration at 301K. The experimental parameters such as Ultrasonic velocity (U), Density (ρ) and viscosity (η) and derived parameters such as Adiabatic compressibility(β_a), Free length(L_f), Acoustical impedance(Z), Relaxation time(τ) and Ultrasonic Attenuation (α/f^2)are studied.

MATERIAL CHOSEN:

ETHYL PROPIONATE:

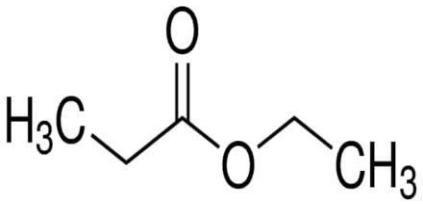

USES:

1. Ethyl propionate is used in perfumery and fragrance.
2. It is used to manufacture various propionates which is used in the reduction of pharmaceuticals, anti-fungal agents, agrochemicals, plastics, rubber chemicals, artificial flavors and perfumery synthesis.
3. It is also used as solvent and in nickel-electroplating solutions.

1-propanol:

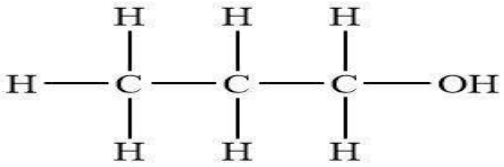

1-Propanol (n-propanol)

USES:

1. 1-propanol appears as a clear and colorless liquid with a mild alcohol odor.
2. It has wide applications in making cosmetics, skin and hair preparations, pharmaceuticals, soaps and window cleaners.

PHYSICAL PROPERTIES:

PROPERTIES	**ETHYL PROPIONATE**	**1-PROPANOL**
Molecular formula	$C_5H_{10}0_2$	C_3H_8O
Molecular weight	102.13 g/mol	60.1 g/mol
Boiling point	99.2℃	97.2℃
Melting point	-73.9℃	-126.1℃
Appearance and odor	Colorless liquid and fruity odor	Colorless liquid with a mild alcohol like odor
Density	0.884325 g/cm^3	0.804 g/cm^3
Refractive Index	1.3844 at 20℃	1.3862 at 20℃

ULTRASONIC INTERFEROMETER

THEORY:

Plate (3.1) Ultrasonic Interferometer.

Ultrasonic interferometer is a simple and direct device which yields accurate and consistent data, from which one can determine the velocity of ultrasonic sound in a liquid medium with a high degree of accuracy. A crystal controlled interferometer with operating frequencies ranging from 1 to 3 MHz has been used to measure the ultrasonic velocity.

ULTRASONIC DEFINITION:

Ultrasonic sound refers to sound pressure with a frequency greater than the human available range(20 Hz to 20 KHz). When an ultrasonic wave propagates through a medium , the molecules in that medium vibrate over short distance in a direction parallel to the longitudinal wave. During this vibration, momentum is transferred among molecule. This causes the wave to pass through the medium.

ULTRASONIC INTERFEROMETER:

An Ultrasonic Interferometer is a simple and direct device to determine the ultrasonic velocity in liquid with a high degree of accuracy. It is simple in design, rugged and gives very accurate and reproducible results. Experiments may be performed over a wide range of temperature from -30℃ to +80℃ on all liquids except those which reacts with the plating of cell and crystal. Nearly, 10 ml of experimental liquid is required. There is no danger of any change such as depolymerization, due to ultrasonic effect since a very small ultrasonic energy is required. In an ultrasonic interferometer, the ultrasonic waves are produced by the piezoelectric methods. At a fixed frequency variable path Interferometer, the wavelength of the sound in an experimental liquid medium is measured, and from this one can calculate its velocity through the medium. The ultrasonic cell consists of a double walled brass cell with chromium plated surfaces having a capacity of 10 ml. The double wall allows water circulation around the experimental liquid to maintain it at a known constant temperature. The micrometer scale is marked in units of 0.05 mm and has an overall length of 25 mm.

Ultrasonic waves of known frequency are produced by a quartz crystal which is fixed at the bottom of the cell. There is a movable metallic plate parallel to the quartz plate, which reflect the waves. The waves interfere with their reflections, and if the separation between the plates is exactly an integer multiple of half wavelength of sound, standing waves are produced in the liquid medium. Under these circumstances, acoustic resonance occurs. The resonant waves are a maximum in amplitude, causing a corresponding maximum in anode current of the piezoelectric generator.

WORKING PRINCIPLE:

The principle used in the measurement of velocity is based on the accurate determination of the wavelength in the medium. Ultrasonic waves of known frequency (f) are produced by quartz crystal fixed at the bottom of the cell. These waves are reflected by a movable metallic plate kept parallel to the quartz crystal. If the separation between these two plates is exactly a whole multiple of the sound wavelength, standing waves are formed in the medium. This acoustic resonance gives rise to an electrical reaction on the generator driving the quartz crystal and anode current of the generator become a maximum. If the distance is now increased or decreased and the variation is exactly one-half wavelengths or multiple of it, anode current become maximum. From the knowledge of wavelength, the velocity can be obtained by the relation,

Velocity = Wavelength x Frequency

$$U = \lambda \times f$$

ADJUSTMENT OF ULTRASONIC INTERFEROMETER:

For initial adjustment two knobs are provided on high frequency generator, one is marked with "ADJ" to adjust the position of the needle on the ammeter and the knob marked "GAIN" is used to increase the sensitivity of the instrument for greater deflection, if desired. The ammeter is used to notice the number of maximum deflection while micrometer is moved up or down in liquid.

PROCEDURE:

- Unscrew the knurled cap of cell and lift it away from double walled construction of the cell. In the middle position of it pour experimental liquid and screw the knurled cap. Wipe out excess liquid overflowing from the cell.
- Insert the cell in the heavy base socket and clamp it with the help of a screw provided on its side. Connect the high frequency generator with cell by coaxial cable provided with the instrument. In ultrasonic interferometer frequency selector knob should be positioned at desired frequency (same frequency as that of liquid cell chosen).
- Move the micrometer slowly in either clockwise or anticlockwise direction till the anode current on the ammeter on the high frequency generator shows a maximum or minimum. Note the reading of micrometer corresponding to the maximum or minimum (which is sharper) in micro ammeter.
- Take about 50 reading of consecutive maximum or minimum and tabulate them. Take average of all differences($\lambda/2$). Once the wavelength (λ) is known the velocity (U) in the liquid can be calculated with the help of the relation.

MEASUREMENT OF THE DENSITY:

The density measurement was made by specific gravity bottle. The specific gravity bottle was initially rinsed using acetone (cleaning agent). The weight of the specific gravity bottle was measured. Then the weight of the specific gravity bottle with the liquid was measured. From the weight measurement the density of the liquid was calculated.

$$\text{Density} = \frac{M}{V} \ (\text{kg/m}^3)$$

Where,

M = mass of the sample in kg

V = volume of the sample in m^3

M = Mass of the specific gravity bottle with liquid – Mass of the empty specific gravity bottle.

Plate (3.2) Specific gravity bottle

MEASUREMENT OF VISCOSITY:

The viscometer is filled with reference liquid (distilled water). Using a suitable arrangement , the water is sucked above the marked level and then it is allowed to flow freely. The water is replaced with a mixture, whose viscosity is to be determined. Using the same procedure, the time taken for flow of liquid mixture at the experimental temperature was determined. Using the time taken for the distilled water and mixture, the viscosity of unknown liquid mixture is determined.

$$\eta = \rho t \times \frac{\eta_0}{\rho_0 t_0} \left(Nsm^{-2} \right)$$

Where,

ρ = density of a liquid concentration in kg/m^3

t = time taken by liquid concentration in s

η_0 = coefficient of viscosity of water in Nsm^{-2}

t_0 = time taken by the distilled water in s

ρ_0 = density of distilled water in kg/m^3

Viscosity is an important transport property for process design in petroleum, petrochemical, chemical and other chemical industries involving fluid transportation, mixing agitation, heat exchange and concentration. The estimation of the viscosity of a mixture is more difficult than of the pure compound.

Plate (3.3) Ostwald's Viscometer

ADIABATIC COMPRESSIBILITY:

The adiabatic compressibility is the fractional decrease of volume per unit increase of pressure, when no heat flows in or out. These changes are related to the compressibility of the medium by thermodynamic relation.

$$\beta_\alpha = \frac{1}{U^2\rho}$$

where,

U = ultrasonic velocity of a liquid in m/s

ρ = density of a liquid in kg/m^3

FREE LENGTH:

The free length is the distance covered by sound wave between the surfaces of the neighbouring molecules. It is measure of intermolecular attractions between the components in binary mixture. The increase of decrease in free length indicates weaken and strengthen of intermolecular attraction. As the ultrasonic velocity increases due to increases in concentration, the interaction free length has to decrease and vice-versa. It is related to ultrasonic velocity and density as

$$L_f = K_T\beta^{1/2} \ (kgms^{-2})$$

Where,

K_T = temperature dependent constant $[93.875+0.357T(10^{-8})]$

T = absolute temperature

U = velocity of liquid in m/s

ρ = density of liquid kg/m^3

The compressibility of a liquid can be expressed in terms of the intermolecular free length which is the distance between the surfaces of the neighbouring molecules.

RELAXATION TIME:

Relaxation time is the time taken for the excitation energy to appear as translational energy and it depends on temperature and on impurities. The dispersion of the ultrasonic velocity in binary mixture reveals information about the characteristic time of the relaxation process that causes dispersion. The relaxation time (τ) can be calculated from the relation,

$$\tau = \frac{4}{3}\beta_a \eta \ (s)$$

where,

β_a = adiabatic compressibility of a liquid in m^2N^{-1}

η = coefficient of viscosity of a liquid in Nsm^{-2}

ACOUSTIC IMPEDANCE:

Sound travels through materials under the influence of sound pressure. Because molecules or atoms of a solid are bound elastically to one another, the excess pressure results in wave propagation through the solid.

The acoustic impedance (Z) of a material is defined as the products of the density (ρ) and ultrasonic velocity (U) given as,

$$Z = U\rho \ (kgm^{-2}s^{-1})$$

where,

U = velocity of a liquid in m/s

ρ = density of a liquid in kg/m^3

ULTRASONIC ATTENUATION:

The amplitude and intensity of ultrasonic waves decrease as they travel through tissue, this phenomenon is known as attenuation. For a given fixed propagation distance, attenuation affects the high frequency ultrasound waves to a greater degree than lower frequency waves. The ultrasonic attenuation (α/f^2) can be calculated from the relation,

$$\frac{\alpha}{f^2} = \frac{8\pi^2\eta}{3\rho U^3} (\text{NP/ms}^2)$$

where,

η = coefficient of viscosity of a liquid in Nsm^{-2}

ρ = density of a liquid in kg/m^3.

U= velocity of a liquid in m/s

CHAPTER-IV

RESULT AND DISCUSSION:

Velocity of 3MHz ultrasonic wave , densities and viscosities of ethyl propionate with n-propanol and in pure liquid were measured with pre calibrated interferometer, density bottle and viscometer respectively to nearest mg in the room temperature and the values of derived parameters such as Adiabatic compressibility(β_a), Intermolecular free length(L_f), Acoustical impedance(Z), Relaxation time(τ) and Ultrasonic attenuation (α/f^2) are calculated using standard relations and are tabulated.

Serial no.	Mole fraction		Velocity(U) (m/s)
	Ethyl Propionate	n-propanol	
1.	1.0	0.0	1143
2.	0.8	0.2	1158
3.	0.6	0.4	1161
4.	0.4	0.6	1182
5.	0.2	0.8	1193
6.	0.0	1.0	1203

Table (4.1): Value of experimental parameter: Velocity (U)

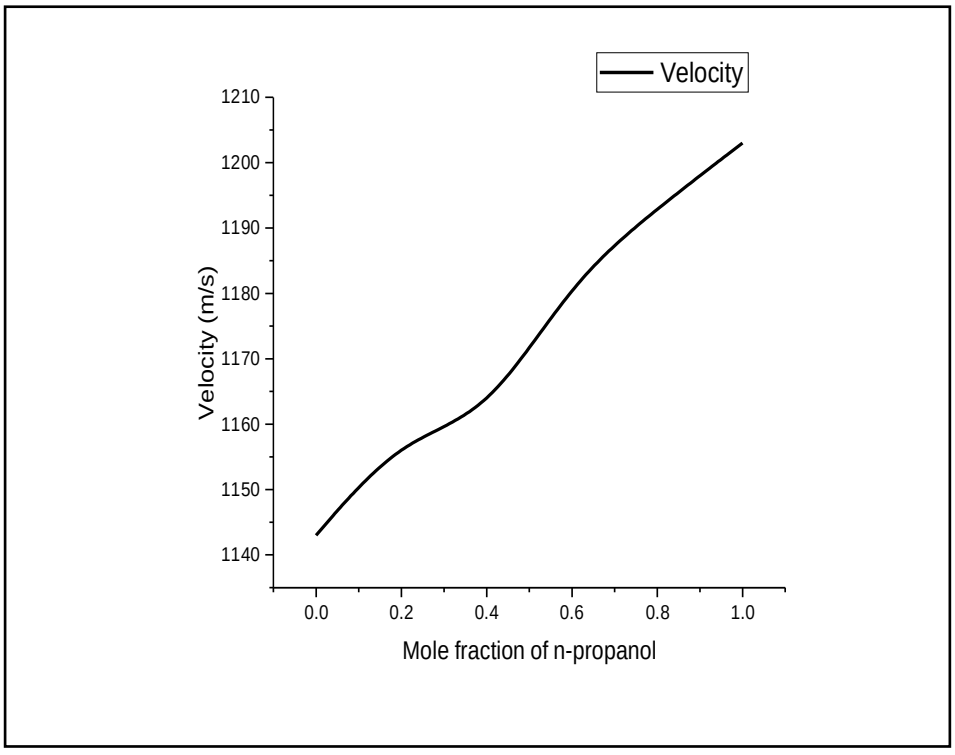

Figure (4.1): Experimental parameter: Velocity (U)

Ultrasonic Velocity (U) was found to increase with the increasing concentrations of n-propanol. It was found to be maximum for 1.0 concentration and minimum for 0.0 concentration of n-propanol. Table (4.1)

Serial no.	Mole fraction		Density(ρ) (kg/m^3)
	Ethyl Propionate	n-propanol	
1.	1.0	0.0	914.9
2.	0.8	0.2	913.9
3.	0.6	0.4	909.9
4.	0.4	0.6	858.6
5.	0.2	0.8	850.3
6.	0.0	1.0	844.1

Table (4.2): Value of experimental parameter: Density (ρ)

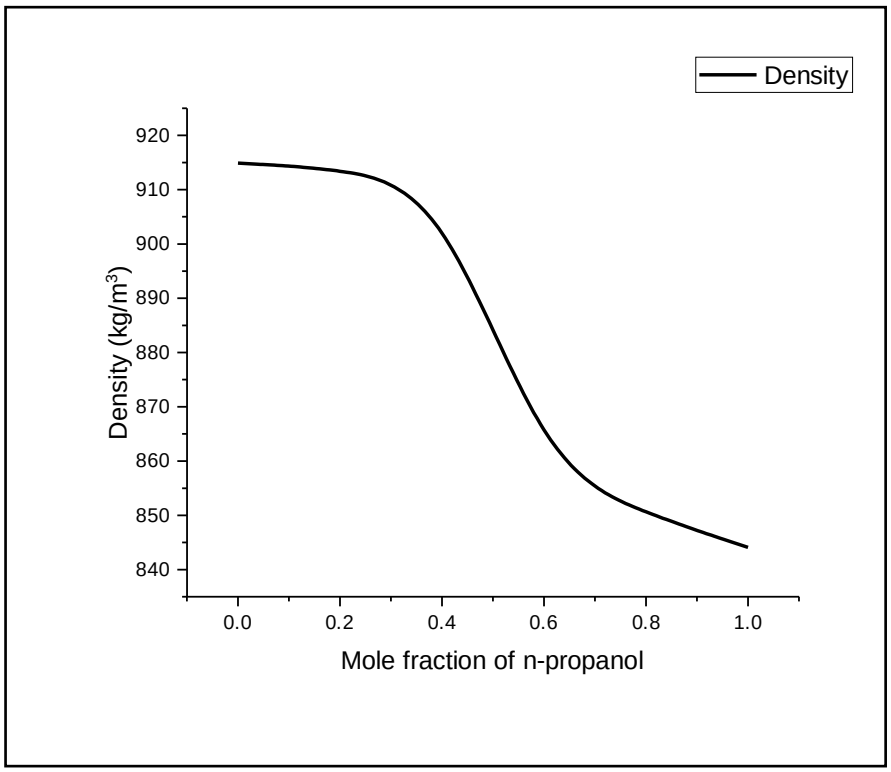

Figure (4.2): Experimental parameter: Density (ρ)

Density (ρ) was found to decrease with the increasing mole fraction of n-propanol. Table (4.2)

Serial no.	Mole fraction		Co-efficient of viscosity(η) (10^{-3}) (Nsm^{-2})
	Ethyl Propionate	n-propanol	
1.	1.0	0.0	0.5085
2.	0.2	0.2	0.5368
3.	0.4	0.4	0.6299
4.	0.6	0.6	0.7475
5.	0.8	0.8	1.0346
6.	0	1.0	1.5052

Table (4.3): Value of experimental parameter: Coefficient of Viscosity (η)

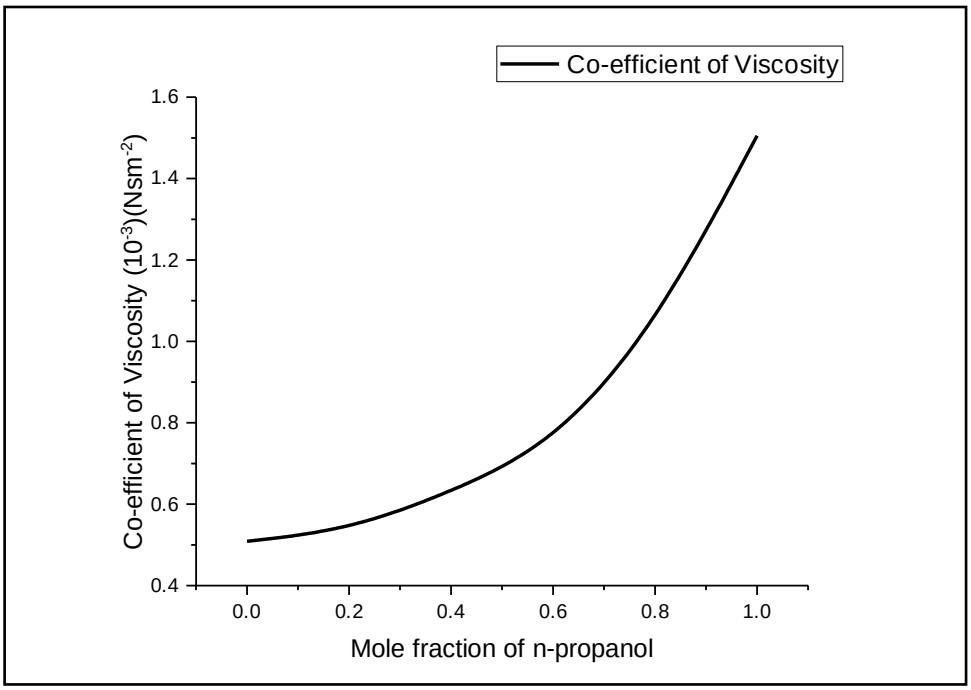

Figure (4.3): Experimental parameter: Coefficient of Viscosity (η)

The Co-efficient of viscosity (η) was found to increase for the increasing concentrations of n-propanol. Table (4.3)

Serial no.	Mole fraction		Adiabatic compressibility(β_a) (10^{-10}) ($N^{-1}m^2$)
	Ethyl Propionate	n-propanol	
1.	1.0	0.0	8.366
2.	0.2	0.2	8.159
3.	0.4	0.4	8.153
4.	0.6	0.6	8.336
5.	0.8	0.8	8.263
6.	0.0	1.0	8.186

Table (4.4): Value of derived parameter: Adiabatic Compressibility (β_a)

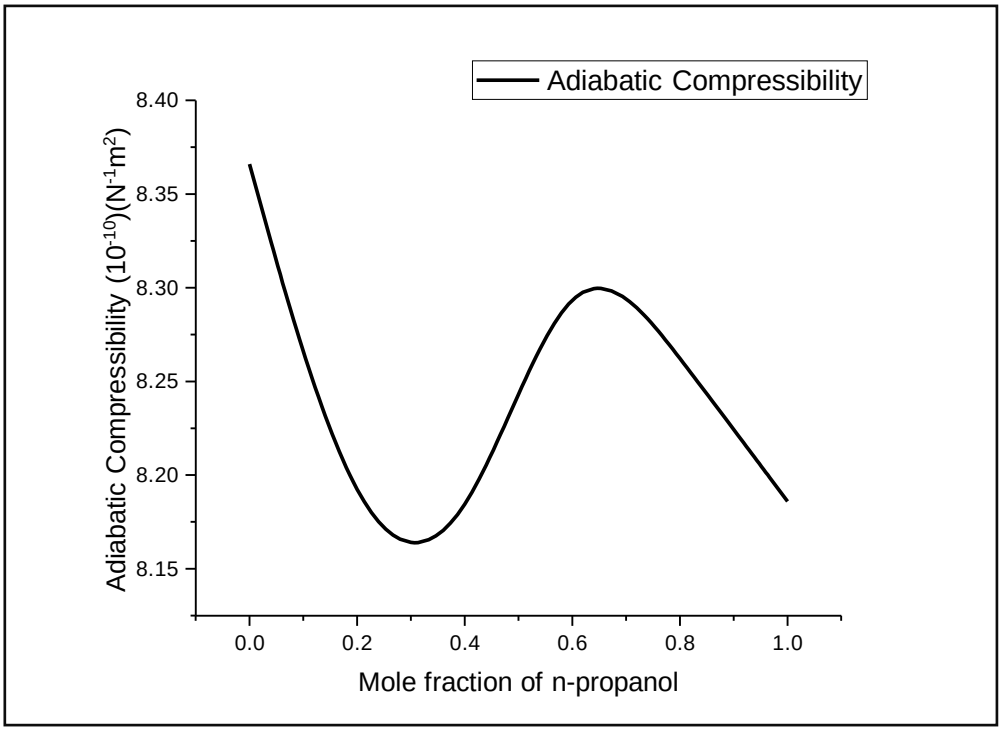

Figure (4.4): Derived parameter: Adiabatic Compressibility (β_a)

Adiabatic compressibility (β_a) was found to be almost equal for 0.0 and 0.6 concentration of n-propanol. It was also found to be more or less equal for 0.2 and 0.4 concentrations of n-propanol. It was found to be more or less equal for 0.8 and 1.0 concentrations of n-propanol. The lowest value was found for 0.4 concentration of n-propanol. Table (4.4)

Serial no.	Mole fraction		Free length (L_f) (10^{-10}) ($kgms^{-2}$)
	Ethyl Propionate	n-propanol	
1.	1.0	0.0	0.6001
2.	0.2	0.2	0.5927
3.	0.4	0.4	0.5924
4.	0.6	0.6	0.5910
5.	0.8	0.8	0.5964
6.	0.0	1.0	0.5936

Table (4.5): Value of derived parameter: Free Length (L_f)

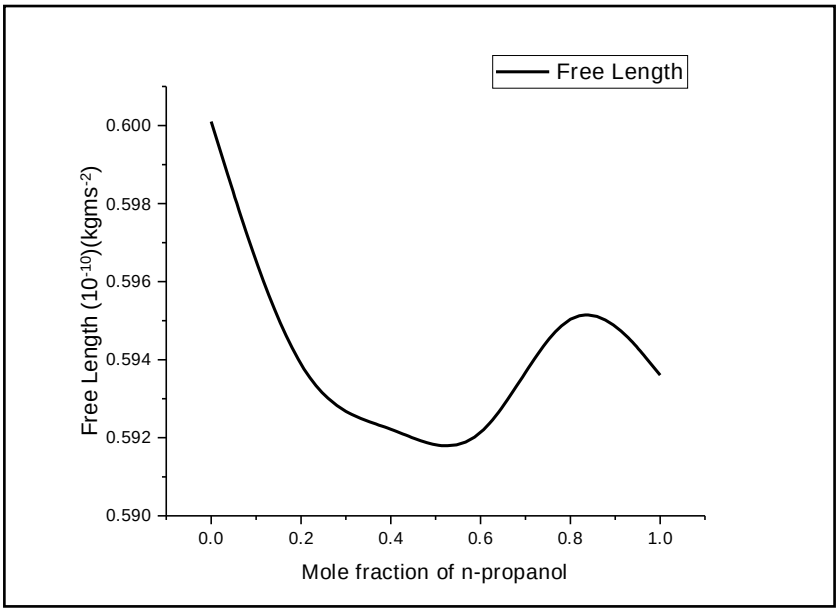

Figure (4.5): Derived parameter: Free Length (L_f)

Free length (L_f) was found to decrease with increasing concentrations of n-propanol upto 0.6 concentrations. Increase in value was noticed for 0.8 concentrations and followed by a decrease in value for the concentration of 1 of n-propanol. Table (4.5)

Serial no.	Mole fraction		Acoustic Impedance(Z) (10^6) $(kgm^{-2}s^{-1})$
	Ethyl Propionate	n-propanol	
1.	1.0	0.0	1.0457
2.	0.8	0.2	1.0582
3.	0.6	0.4	1.0563
4.	0.4	0.6	1.0802
5.	0.2	0.8	1.0144
6.	0.0	1.0	1.0154

Table (4.6): Value of derived parameter: Acoustic Impedance (Z)

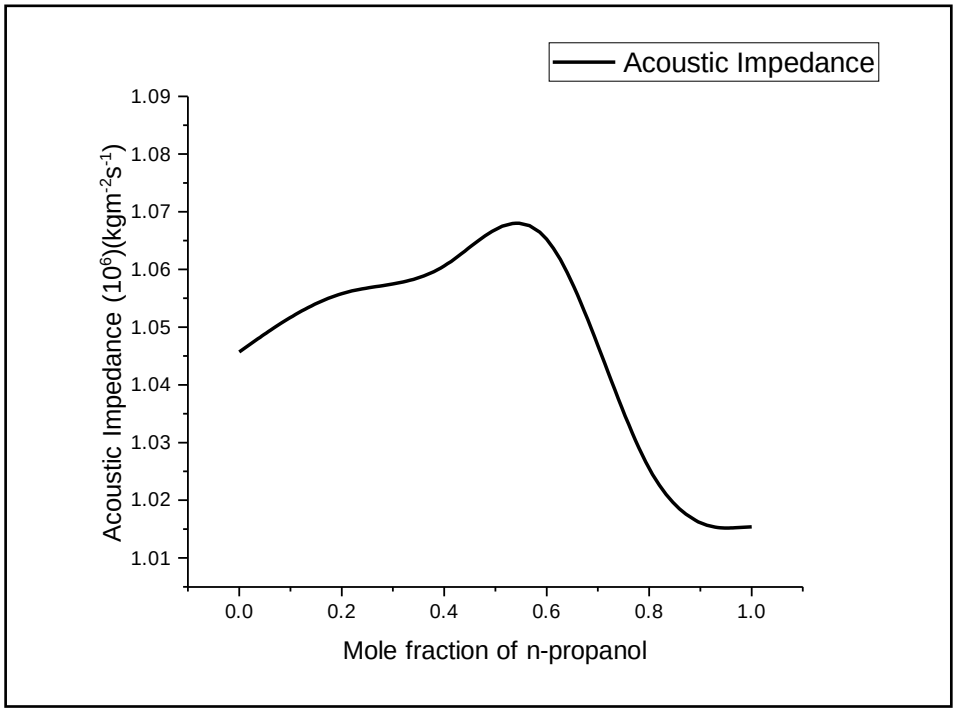

Figure (4.6): Derived parameter: Acoustic Impedance (Z)

In case of Acoustic Impedance (Z), the highest value was reported for 0.6 concentration of n-propanol. It was found to be more or less equal for 0.0, 0.2 and 0.4 concentrations of n-propanol. The values for the concentrations of 0.8 and 1.0 of n-propanol were found to be minimum. Table (4.6)

Serial no.	Mole fraction		Relaxation time(τ) (10^{-12}) (s)
	Ethyl Propionate	n-propanol	
1.	1.0	0.0	0.5671
2.	0.8	0.2	0.5838
3.	0.6	0.4	0.6846
4.	0.4	0.6	0.8306
5.	0.2	0.8	1.1396
6.	0.0	1.0	1.6418

Table (4.7): Value of derived parameter: Relaxation Time (τ)

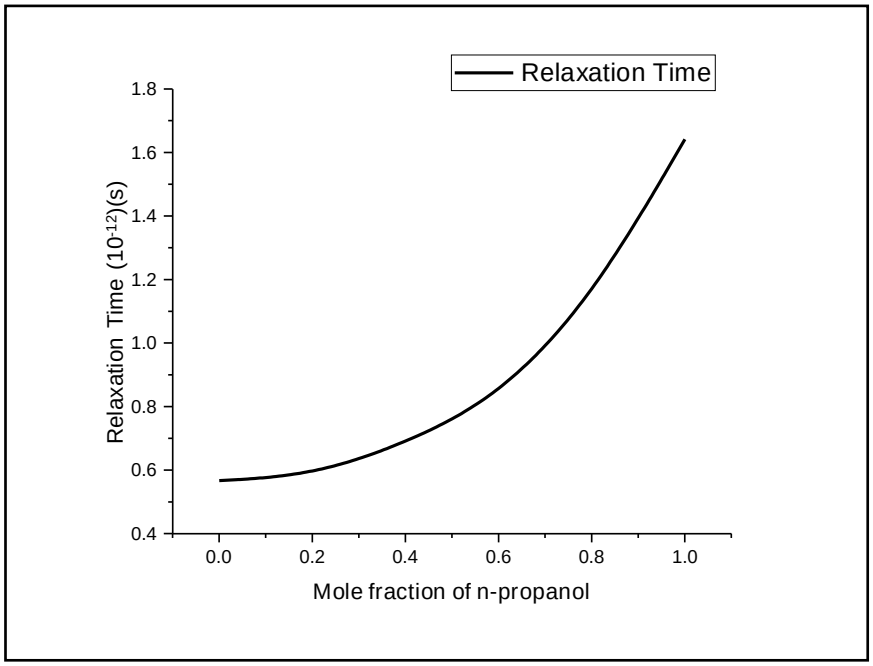

Figure (4.7): Derived parameter: Relaxation Time (τ)

Relaxation time (τ) was found to be increasing with the increasing concentration of n-propanol. It was found to be maximum for 1.0 concentration of n-propanol and minimum for 0.0 concentration of n-propanol. Table (4.7)

Serial no.	Mole fraction		Ultrasonic Attenuation(α/f^2) (10^{-15}) (NP/ms^2)
	Ethyl propionate	n-propanol	
1.	1.0	0.0	9.7875
2.	0.8	0.2	9.9452
3.	0.6	0.4	11.630
4.	0.4	0.6	13.861
5.	0.2	0.8	18.841
6.	0.0	1.0	26.919

Table (4.8): Value of derived parameter: Ultrasonic Attenuation (α/f^2)

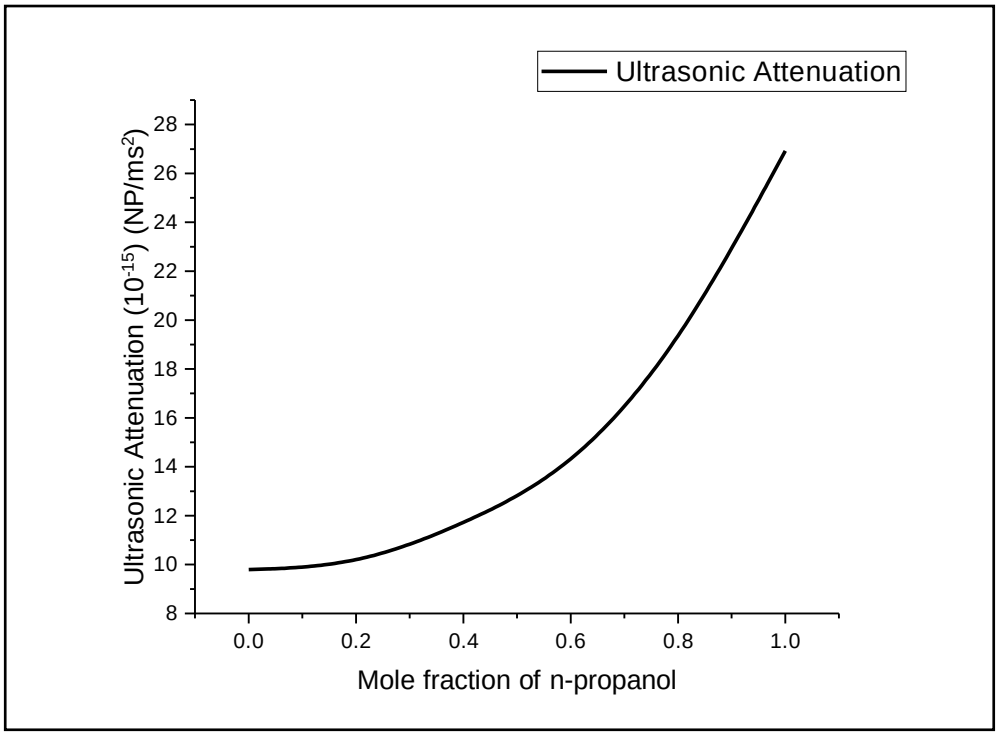

Figure (4.8): Experimental parameter: Ultrasonic Attenuation (α/f^2)

Ultrasonic Attenuation (α/f^2) was found to increase with the increasing mole fraction of n-propanol. It was found to have more or less equal values for 0.0 and 0.2 concentration of n-propanol. Table (4.8)

CHAPTER – V

CONCLUSION:

The ultrasonic velocity (U), density (ρ) and viscosity (η) have been measured for experimental liquid mixture of Ethyl propionate with n-propanol. From these data few acoustical parameters such as Adiabatic compressibility (β_a), Free Length (L_f), Relaxation Time (τ), Acoustical impedance (Z) and Ultrasonic Attenuation (α/f^2) have been computed using standard relations. The variation in ultrasonic velocity and other parameters play significant role in understanding the solvent – solvent , intramolecular interactions between the constitute molecules.

Serial no.	Mole fraction		Velocity(U) (m/s)	Density(ρ) ($kg/m^{3)}$	Coefficient of Viscosity(η) (10^{-3}) (Nsm^{-2})
	Ethyl propionate	n-propanol			
1.	1.0	0.0	1143	914.9	0.5085
2.	0.8	0.2	1158	913.9	0.5368
3.	0.6	0.4	1161	909.9	0.6299
4.	0.4	0.6	1182	858.6	0.7475
5.	0.2	0.8	1193	850.3	1.0346
6.	0.0	1.0	1203	844.1	1.5052

Table (5.1): Values of experimental parameters: U, ρ, η

Serial no.	Mole fraction		Adiabatic compressibility (β_a) (10^{-10}) ($N^{-1}m^2$)	Free length (L_f) (10^{10}) ($kgms^{-2}$)	Acoustic Impedance(Z) (10^6) ($kgm^{-2}s^{-1}$)
	Ethyl propionate	n-propanol			
1.	1.0	0.0	8.366	0.6001	1.0457
2.	0.8	0.2	8.159	0.5927	1.0582
3.	0.6	0.4	8.153	0.5924	1.0563
4.	0.4	0.6	8.336	0.5910	1.0802
5.	0.2	0.8	8.263	0.5964	1.0144
6.	0.0	1.0	8.186	0.5936	1.0154

Table (5.2a): Values of derived parameters: β_a , L_f, , Z

Serial no.	Mole fraction		Relaxation time(τ) (10^{-12}) (s)	Ultrasonic Attenuation(α/f^2) (10^{-15}) (NP/ms^2)
	Ethyl propionate	n-propanol		
1.	1.0	0.0	0.5671	9.7875
2.	0.8	0.2	0.5838	9.9452
3.	0.6	0.4	0.6846	11.630
4.	0.4	0.6	0.8306	13.861
5.	0.2	0.8	1.1396	18.841
6.	0.0	1.0	1.6418	26.919

Table (5.2b): Values of derived parameters: τ, α/f^2

BIBLIOGRAPHY

1. Amara Jyothi Koppula.,Murali Krishnan Patwari.,Sathyanarayana Boodida.(2012).,Study of ultrasound velocities in γ-Butyrolactone and aliphatic ester at temperature of 303.15 K to 313.15.,IJEKT.,vol.1.,issue 8.

2. BahadurAlisha.S.,Nafeesbanu.S.,KrishnaRao.,Subha.M.C.S.(2017)., Ultrasonic Studies on Binary Liquid mixtures of Benzene with Carbitols at 308.15 K.,Indian Jornal of Adavances in Chemical Science 5(3).,pg:142-147 .

3. Bhandhakar .K.,V.D., Bedare G.P., Suryavanshi B. M.(2014).,Study on binary liquid mixture of Metyl Methaculate in 1,4-Dioxane at 303 K.,(IJARPS).,vol.1., issue 5., pg:1-5.

4. Edward Jeyakumar.(2020).,Study on liquid-liquid interactions in 2-Nitroanisole, 1-Pentanol in n-Hexane at various temperature with constant frequency of 2MHz.,International Conference in on Advances in Material Science and Nanotechnology.,vol.24.,part 4.,pg:2123-2136.

5. Elangovan. S.,Mullainathan .(2013).,Ultrasonic studies of mixtures of Ethyl Formate and N-Alcohols in Carbon Tetrachloride.,Indian Journal of Physics.,pg:373-378.

6. Jitindra Gupta.,Rajesh.C.V.(2014).,Study on ion solvent interactions of glucose in water-methanol and ethanol.,IJPRBS.,vol.3(3).,pg:66-72.

7. Kirandeep Kaur.K., K. C. Juglan .(2016).,Study on binary liquid mixtures of ethyl acetate and hexane at constant temperature of 292 K at frequency of 2MHz.,J.Chem.Pharm.Res.,vol.8(9).,pg:49-53.

8. Kumar.R.,Mohammed Kamil.M.G.,Shabeer.,T.K.,Gayathiri.,Shri Prasad.G.S .(2013).,Study on molecular interactions of antibiotic doxycycline hycalte.,Indian Journal of Pure and Applied Physics.,vol. 5.,pg:701-707.

9. Manoj Kumar Parahaj., Abiram Satapathy., Ilyas Ahmed .(2015).,Ultrasonic and Conductometric Studies of Aqueous Potassium Chloride Solutions at Different Temperature.,International Journal of Current Research and Academic Review.,vol. 5.,no.6.,pg:1-5.

10. Monika Dhiman.,Kuljeetsingh.,Arun Upmanyu .(2020).,Study of Excess Acoustical and Thermodynamical Parameters of Binary Solutions of Polupropylene Glycol-400 and n-Alkanols at 303k.,AIP Conference Proceedings.

11. Nagarjun.B.,Sarma.A.V.,Rama Rao .(2013).,Thermodynamic and Acoustic based on molecular interactions in certain Binary liquid systems involving Ethyl benzoate.,Journal of Thermodynamics.,9 pages.

12. Nayeem. S. K.,Sreekanth.,Kondaiah.,Krishna Rao .(2014).,Ultrasonic Investigation of Molecular Interactions in Binary Mixture of Cyclohexanone with Isomers of Butanol.,Journal of Applied Chemistry.,11 pages.

13. Nithiyanantham.S.,Palaniappan.L .(2012).,Study on the acoustical studies on Fructose with enzyme amylase in aqueous media at 298.15K .,Russian Journal of Physical Chemistry.,vol.86.,no.2.,pg:219-222.

14. Paul Divakar.P.Rao.,Samatha.K .(2012).,Study on Molecular Interactions in Binary Liquid Mixtures by Acoustical Method at 303k.,E-Journal of Chemistry.,pg:1332-1335.

15. Peshwa.A.G., Gore.K.U .(2012).,Ultrasonic Studies on 1,4-Dioxane and Methanol Binary Liquid Mixture at Different Temperature.,International Journal of Chemical Science.,10(2).,pg:741-750.

16. Raguraman.A.,Shanthi.N .(2014).,Study on molecular interactions of 1,3,4-Pyrazoline derivatives using ultrasonic technique at 303.15 K.,International letters of Chemistry,Physics and Astronomy.,vol. 39.,pg:100-115.

17. Rajendra K.Shukla.,Amit Sahu .(2013).,Study of Ultrasonic Interaction of Some Ligands and its Metal Complexes.,School Research Library.,Der Pharma Chemical.,vol.5.,pg:291-295.

18. Raju.K.,Rakkapan.C .(2011).,Study on molecular interactions of ethyl cellulose in n-Alkane at various temperature of 303 K, 313 K, 323 K using ultrasonic technique.,Asian Journal of Chemistry.,Vol. 23.,no.1.,pg:19-22.

19. Saneel K. Thakur.,Shivani Chauchan .(2011).,Study on the acoustical behavior of drug climax in aqueous mixture of methanol at 25℃.,Advances in Applied Science Research.,vol.2(2).,pg:208-217.

20. Sathyanarayan.B.,Savitha Jyostna .(2006).,Studies of Binary Mixtures of n-Methylaceta Amide with some Chloroethanes at 308.15 K.,Indian Journal of Pure of Applied Physics.,vol.44.,pg:587-591.

21. Sumathi.T.,Uma Maheswari.J .(2009).,Ultrasonic and Theoretical Studies of some Ternary Liquid Mixtures at Various Temperatures.Indian Journal of Pure and Applied Physics.,vol.47.,pg:782-786.

22. Tanuja.B.,Nithya.G.,Charles C Kanagam .(2012).,Study on the intermolecular interactions in binary mixtures of 4- methoxy benzoin with various solvents such as ethanol, chloroform, acetonitrile, benzene, di-oxane at 298 K using ultrasonic technique.,Ultrasonics Sonochemistry.,vol.19.,issue 6.,pg:1213-1220.

23. Vijalakshmi. K .(2016).,Study on Binary liquid mixtures of methyl acrylate with 2-alkoxy ethanols at 308.15 K .,Int.J.Adv.Res.,4(8).,pg:1888-1895.

EFFECT OF ANNEALING TEMPERATURE ON THE STRUCTURAL AND MORPHOLOGICAL PROPERTIES OF NiO NANOPARTICLES

Project work submitted to St. Mary's college (Autonomous), Thoothukudi, affiliated to Manonmaniam Sundaranar University, Tirunelveli in partial fulfilment of requirements for an award of,

BACHELOR'S DEGREE IN PHYSICS

BY

C. Mariammal - 20AUPH18

S.Santhana Priya - 20AUPH28

P.Sharon Gunarathy - 20AUPH30

P.Sreemathi - 20AUPH36

K.Vijayashanthi - 20AUPH41

Guidance and supervision by

DR. SR. JESSIE FERNANDO

DEPARTMENT OF PHYSICS

St. Mary's College (Autonomous), Thoothukudi- 1

(Re-Accredited with "A+" grade)

2022-2023

CERTIFICATE

This is to certify that this project work entitled, "**EFFECT OF ANNEALING TEMPERATURE ON THE STRUCTURAL AND MORPHOLOGICAL PROPERTIES OF NiO NANOPARTICLES**" is submitted to **ST. MARY'S COLLEGE (AUTONOMOUS), THOOTHUKUDI** in partial fulfilment for the award of Bachelor's Degree in Physics and is a record work done during the year 2022-2023 by the following students.

C.Mariammal	**-20AUPH18**
S.Santhana Priya	**-20AUPH28**
P.Sharon Gunarathy	**-20AUPH30**
P.Sreemathi	**-20AUPH36**
K.Vijayashanthi	**-20AUPH41**

Neesii Lobo
GUIDE

Neesii Lobo
HEAD OF THE DEPARTMENT

HEAD
Department of Physics,
St. Mary's College (Autonomous),
Thoothukudi - 628 001.

13/4/23
EXAMINER

Lucia Rose
PRINCIPAL
St. Mary's College (Autonomous)
Thoothukudi - 628 001.

DECLARATION

We hereby declare that the project entitled, "**EFFECT OF ANNEALING TEMPERATURE ON THE STRUCTURE AND MORPHOLOGICAL PROPERTIES OF NiO NANOPARTICLES**" submitted to **St. Mary's College (Autonomous), Thoothukudi,** affiliated to Manonmaniam Sundaranar University, for the Bachelor's Degree of Science in Physics is our original work and that, it has not previously formed the basis for the award of any Degree, Diploma or similar title.

C.Mariammal	**-20AUPH18**
S.Santhana Priya	**-20AUPH28**
P.Sharon Gunarathy	**-20AUPH30**
P.Sreemathi	**-20AUPH36**
K.Vijayashanthi	**-20AUPH41**

Station: Thoothukudi.

Date : 03.04.2023

ACKNOWLEDGEMENT

In the development of this project, thanks must flow outward as the sparks fly upward. Invaluable guidance without which, this project would not have seen the light of this day. A large number of people have devoted their time, energy and talent at our disposal and we salute them all.

First of all, we would like to thank God Almighty for His sunny disposition and skill in pulling everything together. We are infinitely indebted to our college principal **Dr. Sr. A.S.J. LUCIA ROSE M.Sc., M.Phil., Ph.D., and PGDCA** for providing this opportunity and we are extremely thankful for all the help encouragement and invaluable moral support provided to us throughout the project work.

We owe our special gratitude to **Dr. Sr. JESSIE FERNANDO,** Head of the department of Physics and our project guide for her inspiring guidance, encouragement and scholarly suggestion which helped us to complete this work successfully.

We profusely thank **Mrs. P. PADMAVATHI,** Assistant Professor of Physics (SSC) for her assistance and support throughout this project.

We would like to extend our gratitude to department of Physics, St. Mary's College (Autonomous), Thoothukudi for providing us with Hot air oven and Muffle furnace used for the preparation of nanoparticles.

We also thank the **MARIAN STAR CENTER**, for providing the latest equipment to carry on our project successfully, under the STAR COLLEGE SCHEME, sponsored by DBT, Chennai.

And also, we thank **Mr. VINCENT, St. JOSEPH'S COLLEGE, TRICHY** for carrying out the characterization studies and providing us with the result promptly.

We wish to accord our sincere gratitude to our non-teaching staff members who helped us to carry out our project work in the lab smoothly.

"DO THE BEST YOU CAN UNTIL YOU KNOW BETTER. THEN WHEN YOU KNOW BETTER, DO BETTER."

We also thank our parents and friends from the depth of our hearts for their profound encouragement and timely help.

CHAPTER 1

1.1. INTRODUCTION:

Nanoscience is the study of structures and materials on the scale of nanometers. The term 'nano' refers to the metric prefix 10^-9. It means "one billionth of something". A single strand of DNA, the building blocks of all living things, is about three nano meters wide. Scientists have created nanostructures in the laboratory that mimic some of nature's amazing nanostructures. Nanostructures can be created by reacting chemicals in liquids and gases to generate nano-fibers, nano-crystals and quantum dots some as small as one nanometer wide.

Although breakthroughs in any research field are difficult to predict, the future of nano-science will likely involve scaling up from atomic assembly and individual nanodevices to macroscopic system and structures with evolving properties and multiple function. These structures can interact with their surroundings at dimensions ranging from that of humans and beyond it[1].

1.2. OPPORTUNITIES OF NANOWORLD :

The word Nanoscience refers to the study of manipulation and engineering of matter, particles and structures on the Nano meter scale (one million of a millimetre, the scale of atoms and molecules). Important properties of materials, such as electrical, optical, thermal and mechanical properties are determined by the way molecules and atoms assemble on the nanoscale into larger structures. Moreover, in Nano meter size structures these properties often differ then on macroscale, because quantum mechanical effects become important.

Nanotechnology is the application of nanoscience leading to the use of new nanomaterials and nanoscience components as useful products. Nanotechnology will eventually provide us with the ability to design custom-made materials and product with new enhanced properties. New nano electronics components, new types

of smart devices, medicines and sensors, and even interfaces between electronics and biological systems.

These new born scientific disciplines are situated at the interface between physics, chemistry, materials science, microelectronics, biochemistry & biotechnology control of these disciplines therefore requires an academic & multidisciplinary scientific education[2].

1.3. NANOSCALE:

Nanoscale materials are broadly defined set of substances that have at least one critical dimension less than 100 Nano meters and possess unique optical, magnetic, or electrical properties. Ultra fine particulate matter is a well-known example of nanoscale particles found in the environment[3].

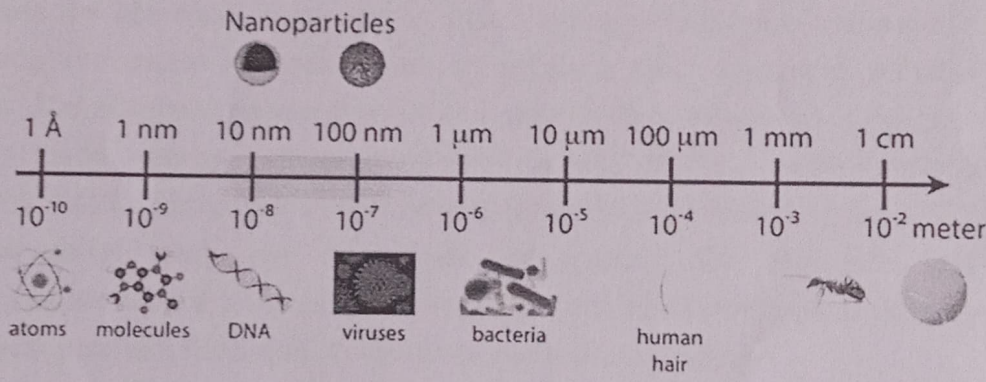

Fig 1.1

1.4. CLASSIFICATION OF NANOPARTICLES:

Nano particles can be classified according to their size, morphology, physical and chemical properties. Often, the classification of these nanomaterials determines their function.

Carbon based Nanoparticles:

Carbon based nanoparticles are split into carbon nanotubes and fullerenes. The use of these nanomaterials tends to focus on structural reinforcement as they are 100 times stronger than steel. Carbon based nanoparticles can be classified into single-walled carbon nanotubes and multi-walled carbon nanotubes. Carbon nanotubes are

unique in a way as they are thermally conductive along the length and non-conductive across the tube.

Ceramic Nanoparticles:

These nano materials are inorganic solids composed of oxides, carbides, carbonates and phosphates. ceramic nanoparticles have high heat resistance and chemical inertness and have applications in photocatalysis, photodegradation of dyes, drug delivery and biological imaging. By controlling their specific characteristic like size, surface area, porosity, surface to volume ratio, these nanomaterials perform as good drug delivery agents.

Metal Nanoparticles:

Metal nanoparticles are prepared from metal precursors and can be synthesised by chemical, electrochemical or photochemical methods. In chemical method the metal nanoparticles are obtained by reducing the metal-ion precursors in solution with chemical reducing agents. The resultant nanomaterials can adsorb small molecules and have high surface energy. Metal nanoparticles are utilized across several research fields, including detection and imaging of biomolecules and in environmental and bio analytical application for example gold nanoparticles are used to coat the sample before SEM analysis to enhance SEM and produce high quality electron microscopy images.

Semiconductor Nanoparticles:

Semiconductor nanoparticles have properties like those of metals and non-metals and are found in the periodic table in group II-VI, III-V or IV-VI. These nanoparticles have wide bandgaps, which upon tuning show different properties. Some examples of semiconductor nanoparticles are GaN, GaP, InP, InAs from group III-V, ZnO, ZnS, CdS, CdSe, CdTe are group II-VI semiconductor and sillicon and germanium are from group IV. Semiconductor nanoparticles are applied to photocatalysis, electronic devices, nanophotonic and water splitting applications.

Polymeric Nanoparticles:

Polymeric nanoparticles are organic based nanoparticles. Depending upon the preparation method, polymeric nanoparticles have structures shaped like nanocapsules or nanospheres. A nanosphere nanoparticles has a matrix like structure, whereas nano capsules have core-shell morphology. In nanosphere polymeric nanoparticles, the active compounds and the polymer are uniformly dispersed while in nanocapsule nanoparticles, the active compounds are confined and surrounded by a polymer shell. It has the application in drug delivery and diagnostics. Drug delivery systems with polymeric nanoparticles are also highly biodegradable and biocompatible

Lipid Nanoparticles:

Lipid nanoparticles are generally spherical with a diameter ranging from 10 to 100nm. Their structure consists of a solid core made of lipid and a matrix containing soluble lipophilic molecules, and the external core is stabilized by surfactants and emulsifiers. Lipid nanoparticles have applications in the biomedical field as drug carriers and RNA release in cancer therapy[4].

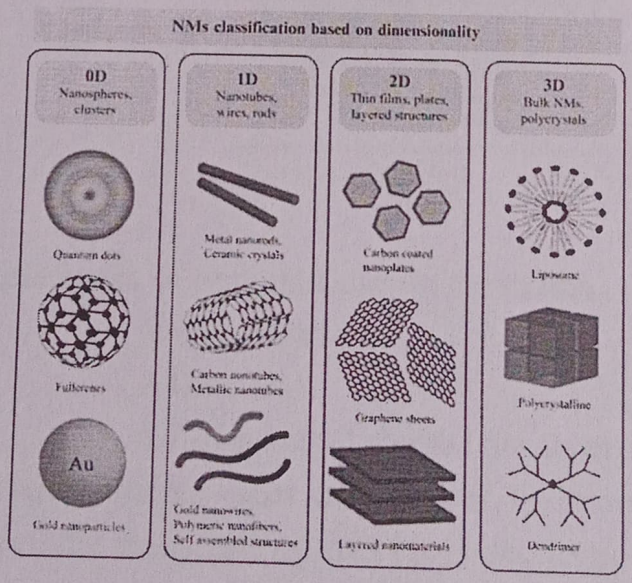

Fig 1.2

1.5. SRUCTURES OF NANOPARTICLES:

Nanoparticles can have a regular crystalline structure, can be amorphous, or can form a pseudo close packing indescribable by any of the crystallographic space group. The structure of a nanoparticle of a material is generally determined by the chemical composition of the material, the number of atoms in the particle, and the character of the chemical interaction between atoms. Nanoparticles can have a regular crystalline structure, can be amorphous, or can form a pseudo close packing indescribable by any of the crystallographic space groups. For each of these structural states of a nanoparticle, there is a certain set of numbers of the atoms involved in the particle that corresponds to optimum stable configurations. These numbers are usually called the magic numbers.

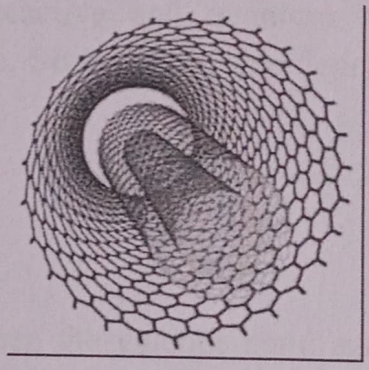

Fig 1.3

Three unique states of nanoparticles in particular

1.Spherical

2.Disc and

3.Cylindrical shaped are used

Nanoparticles sizes and shapes in three dimensions are deduced from the measured optical cross-sections.

Here, rod shaped nanoparticles could be the best option, due to its more infrared absorption property as compare to spherical gold nanoparticles[5].

1.6. WORLD AT NANOLEVEL:

Nano world is a highly integrated and extensively broad area of research and development. The Royal Society and The Royal Academy of Engineering have categorized nanoscience into nanoscale in one dimension; nanoscale in two dimensions, and nanoscale in three dimensions[6].

1.7. PROPERTIES OF NANOPARTICLES:

The physical and chemical properties of NPs are function of their size and shape and are therefore different as compared to size independent constant physical properties of bulk materials. This difference in properties at nanoscale is due to their large surface area which makes them highly reactive and quantum size effects which become dominant at nanoscale. Some of the size dependent properties of NPs are brifely described here:

(i) BAND GAP:

The band gap between the valence band and conduction band increases as the size of NP's decreases.

(ii) MELTING POINT:

The melting point or phase transition temperature of NPs is low and this decrease becomes more pronounced when the particle size gets below 5nm.

(iii) MECHANICAL PROPERTIES:

The probability of defects is low at nanoscale, due to which their mechanical strength is high and they are characterized as highly tough and hard materials.

(iv) ELECTRICAL PROPERTIES:

The electrical conductivity is influenced in two ways at

nanoscale. It decreases because of large surface scattering while it may increase because of better ordering.

(v) OPTICAL PROPERTIES:

Colour or optical properties of NPs are highly dependent on the size of particle. This change in colour can be explained on the basis of shift of λSPR to higher wavelengths as the particle size increases in case of plasmonic NPs.

(vi) MAGNETIC PROPERTIES:

Due to large surface energy of materials at nanoscale, ferromagnetism vanishes and shifts to super magnetism.

(vii) CATALYTIC PROPERTIES:

The catalytic efficiency of NPs is very high as compared to bulk material due to their large surface area[7].

1.8. APPLICATIONS OF NANOSCIENCE:

Nanoscience also has applications in different aspects of life such as food, medical science and fiction

Nanoscience in food processing:

In food processing nanoscience is used for improving food ingredients, packaging, flavouring and colouring and safety monitoring. Major food processing companies are using nanoscience in testing the chemical reactions ad for enhancing preservatives.

Nanoscience in medicine:

In the field of medical sciences nanoscience is used to detect the cancerous bacterial in the human body at early stages. Blood thinner used to regulate the blood level and the body also uses nanostructure particles.

Nanoscience and fiction:

Nanoscience is comparatively newer concept in the world of fiction sciences nanotechnology is a root of nanoscience. When both were combined together, we get extra ordinary devices muscle-massaging devices and movie graphics are the result of nanoscience

Nanoscience and automobiles:

In automobile engineering nanoscience plays important role in making brakes of the vehicles more efficient and soft and for improving the liquids of the disc brakes. In the world of automobile industry, nanoscience is also used for making engines stronger and reliable. Protective nano-paints for cars are made that resist water and dirt, Resistant to chipping and scratches, Brighter colours, enhanced gloss to cars all these advancement came into being when nanoscience stepped into field.

Influence of nanoscience in our lives:

Nanoscience has a great impact in our lives and lifestyle. Nanoscience when merged with nanotechnology provided us with the Neuro-electrical mechanics and other health care device, which has reduced the death rate in the world. Nanoscience has given us the better way to live and provided us with the exigent and flawless products. Later on we would be definite seeing the more improved products of nanoscience because it has given us the new eye to see and realize the world[1].

1.9. REVIEW OF LITERATURE:

Dhivya Christo Anitha et al.,(2019) reported the pure NiO nano particle were prepared by Green synthesis method using Thepesia populena leaf extra and nickel sulphate as raw materials. The synthesized NiO nanoparticles were characterized by powder X-ray diffraction, UV-V is analysis, FTIR analysis, SEM and EDAX analysis. From UV spectrum the optical properties of the samples were determined. FTIR spectrum reveals the various functional groups present in the sample. SEM image

shows the surface morphology of pure and NiO nano particles. From EDX the presence of Ni, and O were confirmed. VSM confirms the super paramagnetism of NiO nanoparticle[8].

Abdul Ameer (2018) explained the Low cost Co-Precipitation method was used for preparation of novel oxide(NiO) nano particle thin films with simple, with two different PH values 6,12 and its effect on structural and optical properties as an active optical filter. Experimental results of structural properties X-ray diffraction (XRD) showed that both Nickel oxide nanoparticles with (PH=6 and 12) have polycrystalline structure smaller average particle size about 8.5 nm for PH=6 in camparison with PH=12. Morphological studies using Scanning electron microscopy (SEM) and atomic force microscope (AFM) show uniform nano rod distribution for PH=6 with smaller average diameter, average roughness as compared with NiO with PH=12 that showed larger diameter, grain size, spherical shapes with scope of excellent sensing applications due to high roughness. Optical properties results show blue shift for PH=6 as compared with PH=12m leading to potential of optoelectronic applications and as active optical[9].

Vijaya kumar et al.,(2019) contributed to the reports on the synthesis and also compares the main physical properties of nickel oxide nanoparticles (NiO NPs) synthesized by a completely green process using Gymnema sylvestere plant extract and sodium hydroxide as an effective reducing agent for co-precipitation method. The synthesized nanoparticle were characterized by XRD, HRTEM, EDS, FTIR, UV-visible, XPS,ERP and zeta potential analysis methods. Further the synthesized NiO NPs were evaluated the in vitro toxicity studies using microbial and MCF-7 cancer cell cell line models. Further cytotoxicity studies and acridine orange and ethidium bromide staining confirmed that green synthesized NiO Nps possess low toxicity compared with chemically synthesized NiO NPs[10]

Pooja Khandagale et al., (2017) explained the synthesis of Nickel oxide nano particle using Co-Precipitation method. The prepared nano particles of metal oxide (NiO) were characterized by using XRD, SEM, TEM, FTIR&EDAX. The average particle size, crystalline structure were estimated using XRD Analysis. The structural functional groups & optical characters were analysed by using SEM,FTIR&UV-Visible

Techniques. EDAX spectrum that showed the elemental composition of Nickel oxide,FTIR showed the functional groups present in the synthesized Nickel oxide Nanoparticles . TEM Results confirmed the synthesis of nickel oxide nanoparticles[11].

Siraj Uddin et al.,(2020)reported that nickel oxide nanoparticles (NiO NPs) were synthesized using leaf extract of Berberis balochistanica (BB) an endemic medicinal plant. The BB leaves extract act as a strong reducing, stabilizing, and capping agent in the synthesis of BB@NiONPs. Further, BB@NiONPs were characterized using UV–visible spectroscopy (UV–vis), X-ray diffraction (XRD), Fourier transform infrared spectroscopy (FT-IR), Energy dispersive spectroscopy (EDS), scanning electron microscopy (SEM), and average size was calculated _21.7 nm). Multiple in vitro biological activities were performed to determine their therapeutic potentials. The BB@NiONPs showed strong antioxidant activities in term of 2,2-diphenyl-1-picrylhydrazyl (DPPH) and total antioxidant capacity (TAC) with scavenging potential of 69.98 and 59.59% at 200 µg/ml, respectively. The antibacterial and antifungal testes were examined using different bacterial and fungal strains and dose-dependent inhibition response was reported. The result determined potential cytotoxic activity with LD50 value (49.10 µg/ml) and outstanding stimulatory effect of BB@NiONPs on seed germination at lower concentrations as compared to control. Overall, result concluded that biosynthesis of NiONPs using leaf extracts of Berberis balochistanica is cheap, easy, and safe method and could be used in biomedical and agriculture field as nanomedicine and nano fertilizer[12].

Karpagavinayagam et al.,(2019)presented work on Eco-friendly synthesis of Nickel Oxide Nanoparticles (NiO-NPs) using Avicennia Marina leaf extract in an aqueous medium. The prepared NiO-NPs were characterized by UV–Visible, FT-IR, X-ray diffraction, AFM, FE-SEM, TEM, and electrochemical techniques to find the band gap energy, functional group, grain size, morphology, and the structure, particle size respectively. UV–Vis absorption spectrum of nickel oxide nanoparticles (NiO-NPs) shows a peak in the region of 297 nm. The FTIR spectrum of NiONPs shows bands at 872 cm_1 and 466 cm_1. From the FESEM results, the average size of NiO-NPs is seen to be in the range of 30–100 nm. Electrochemical studies were carried out to assess the redox behavior

of NiO-NPs. The obtained results confirmed the formation of nickel oxide nanoparticles from the biomaterial leaf component. The methanol oxidation of NiO-NPs has been studied by voltammetry[13].

Angel Ezhilarasi et al.,(2016)followed the Green protocols for the synthesis of nickel oxide nanoparticles using *Moringa oleifera* plant extract has been reported in the present study as they are cost effective and ecofriendly,moreover this paper records that the nickel oxide (NiO) nanoparticles prepared from green method shows better cytotoxicity and antibacterial activity. The NiO nanoparticles were characterized by X-ray diffraction (XRD), Fourier transform infrared spectroscopy (FTIR), High resolution transmission electron microscopy (HRTEM), Energy dispersive X-ray analysis (EDX), and Photoluminescence spectroscopy (PL). The formation of a pure nickel oxide phase was confirmed by XRD and FTIR. The synthesized NiO nanoparticles was single crystalline having face centered cubic phase and has two intense photoluminescence emissions at 305.46 nm and 410 nm. The formation of nano and micro structures was confirmed by HRTEM. The invitro cytotoxicity and cell viability of human cancer cell HT- 29 (Colon Carcinoma cell lines) and antibacterial studies against various bacterial strains were studied with various concentrations of nickel oxide nanoparticles prepared from *Moringa oleifera* plant extract. MTT assay measurements on cell vialbility and morphological studies proved that the synthesized NiO nanoparticles pocess cytotoxic activity against human cancer cells and the various zones of inhibition (mm),obtained revealed the effective antibacterial activity of NiO nanoparticlesagainst various Gram positive and Gram negative bacterial pathogens[14].

Infantiya Stephen Grace et al.,(2019) reported that porous nanostructured transition metal oxide comprehensively pursued by the virtue of their optimistic applications of their peculiar catalytic, electrical, and magnetic behavior properties. Nanostructured nickel oxide nanoparticles are a promising metal oxide have been fabricated via the sol-gel route to examine their morphological, optical, and structural properties. Nickel oxide nanoparticles are an anti-ferromagnetic material of the NaCl structure with p-type semiconductor. The synthesis was achieved by using Nickel (II) nitrate hexahydrate ((NiNO3)2. 6H2O) as

the precursor and citric acid as solvent. The nickel oxide calcinations temperature has been investigated. The morphological, structural, and optical properties of as-synthesized nickel oxide nanoparticles were distinguished by X-ray diffraction (XRD), UV-vis spectroscopy, scanning electron microscopy (SEM), and Fourier transform infrared spectroscopy (FTIR). The high phase purity crystalline constitution with a cubic structure of the nickel oxide nanoparticles was characterized by the X-ray diffraction technique. The nickel oxide nanoparticles of the band gap (eV) are examined by the ultraviolet visible spectroscopy using the Tauc plot, where the blue shift was investigated. Using the Fourier transform infrared spectroscopy confirmed the existence of functional group (NiO) on the surface of the material[15].

Zahara Sabouri et al.,(2018) Experimentally determined that dispersed nickel oxide nanoparticles (NiO-NPs) have been obtained through a "green" co-precipitation method using nickel nitrate hexahydrate and starch as Ni precursor and stabilizing/capping agent, respectively, while ammonia has been applied in the role of a complex agent throughout this procedure. The structural photocatalyst, optical, and magnetic qualities of the NiO-NPs have been enquired into by FTIR, UV–Vis, XRD, FESEM, EDX, VSM, and TGA/DTG. Magnetic measurement has confirmed the superparamagnetic behavior of NiO-NPs at ambient temperature after calcination procedures. The band gap of NiO-NPs has been calculated to be about 3.55 eV and thus, this sample is a semi-conductor that can be utilized as photocatalysts. According to the obtained results, about 80 % of methylene blue (MB) degrades in the presence of NiO-NPs under UV light after 270 min. *In vitro* cytotoxicity investigations on cells has exhibited a dose dependent toxicity with non-toxic consequences in concentrations below ~7 µg/mL. The synthesis outcomes have shown that starch can be an interesting material with the potential of being employed as a stabilizer for preparing small nanoparticles, as well as being a bio-template for nanoparticles growth [16].

Israa Muzahem Rashid et al.,(2021) found out the green synthesis of nickel oxide nanoparticles (*NiO-NP*) using Ni(*NO3*)*2* as a precursor, olive tree leaves as a reducing agent, and D-sorbitol as a capping agent.

The structural, optical, and morphology of the synthesized *NiO-NP* have been characterized using ultraviolet–visible spectroscopy (*UV-Vis*), X-ray crystallography *(XRD)* pattern, Fourier transform infrared spectroscopy *(FT-IR)* and scanning electron microscope *(SEM)* analysis. The *SEM* analysis showed that the nanoparticles have a spherical shape and highly crystalline as well as highly agglomerated and appear as cluster of nanoparticles with a size range of (30 to 65 nm). The Scherrer relation has been used to estimate the crystallite size of *NiO-NP* which has been found about 42 nm. The *NiO-NP*s have subsequently used as adsorbents for adsorption of two types of dyes; methylene blue *(MB)* as cation dye and methyl orange *(MO)* as anion dye. The removal efficiency of dyes from contaminated water was investigated during various key parameters at room temperature; initial dye concentration (Co), pH, contact time (t), agitation speed, and adsorbent dosage. The maximum removal of *MB* dye was found to be 96% (Co=25 mg/l, pH=10, contact time=100 min, agitation speed=300 rpm and adsorbent dosage=6 g/l), while for *MO* the maximum removal reached 88% at (Co=20 mg/L, pH=2, t =160 min, agitation speed=300 rpm and adsorbent dosage=6 g/L). The experimental adsorption data were found to well obey Freundlich isotherm. The kinetic investigation showed that the adsorption process for both dyes followed a pseudo-second-order model with rate constants 0.0109 and 0.0079 (mg/g min) for *MB* and *MO*, respectively[17].

Mohd Kashif Aziz et al.,(2022) reported that unique and bio-inspired synthesis of nickel oxide nanoparticles by using an innocuous and ecofriendly waste material that is watermelon rind. In the reaction, watermelon rind recycled and used its extract as a solvent which act as a reductant for a synthesis of nickel oxide nanoparticle. The synthesized NiO NPs were analyzed by using X-ray Diffraction (XRD), transmission electron microscopy (TEM), Fourier transform infrared spectroscopy (FTIR) and UV-Vis spectroscopy. FTIR peak at 745 cm-1 and 671 cm-1 indicated that the formation of Ni-O bond. A prominent peak of UV-Vis spectra at 283 nm and band gap, calculated with the help of UV data, was ~3.3 eV. The obtained PXRD pattern and JCPDS data suggested the formation of nickel oxide nanoparticle and the average crystallite size calculated by Scherrer's equation in between 30 to 150 nm. The average grain size of NiO NPs perceived from TEM images was 46.55 nm and

polygonal barrel shape particles. Since, a simple, straightforward, pollutant-free, and economical technique for the synthesis of nickel oxide nanoparticles. However, the above synthesized nickel oxide nanoparticles have been explored for biophysical parameter vis. radicle length, plumule length and germination percentage on a *Vigna radiata* (moong) seed by the treatment of some concentration i.e. 25 ppm, 50 ppm, 100 ppm and 200 ppm in germination processes. At a low concentration of 25 ppm, a beneficial improvement in the germination process of *Vigna radiata* seed was observed[18].

1.10. AIM OF THE CURRENT WORK

- To synthesis NiO nanoparticles by green approach.
- To study it's various characteristics using XRD and SEM.

1.11. IDEAS OF MATERIAL IMPORTANCE:

1.11.1. NICKEL OXIDE:

NiO is an intrinsic P-type semiconductor with a wide band gap and good thermal and chemical stability.

NiO is halite, rock salt structured .

It is insoluble in water but soluble in KCN.

Its melting point is very high-1955 C (3,551 F; 2,228K).

NiO is a commonly used hole transport material in thin film solar cells.

It's a component in nickel-ion battery and its component in fuel cells.

NiO was used to make the NiCO rechargeable batteries found in many electronic desires until the development of the environmental superior NiMH battery.

Nanostructured nickel oxide nanoparticle is a metal oxide have been fabricated via the sol-gel oxite to examine their morphology, optical, and structured properties.

Nickel oxide nanoparticle are an antihetro magnetic material of the NaCl structure with P-type semiconductor many methods have been attempted to prepare nanosized. NiO NPs synthesis using a reduction agent from visit vinifera and it showed

the significant cytotoxicity against MCF and AMGM5 cell lines[19].

1.11.2. USAGE:

Owing to their specific functional characteristics and importance in a widely variety of technical applications, nickel oxide (NiO) is extensively investigated as electronic component ceramic material and catalysts.

Recent studies indicate the great potential of NiO NPs in biomedical applications, including cancer diagnosis and therapy[10].

NiO nanoparticles may have many applications such as in the manufacture of electronics, films, magnetic material P-type transparent conducting films, gas sensors, catalysts alkaline batteries cathode, and solid oxide fuel cells anode[20].

The potential applications of NiO are in various areas like in water treatment, gas sensing, electronical performance, and antimicrobial activities[7].

They also find environmental applications in the field of absorption of hazardous dye and inorganic pollutants and thus play a vital role in the cleanliness of environment. Due to their good antibacterial and anti-inflammatory they are used in the field of biomedicine[10].

1.12. APPLICATIONS OF ALOE VERA:

TREATMENT OF SKIN CONDITION SUCH AS PSORIASIS AND ACNE:

Treatment of skin conditions like psoriasis acne and skin breakout aloe creams effects on the skin and have been displayed to lessen irritations and aggravation.

WOUND HEALING:

Aloe vera gel could not just increment how much collagen in injuries at any point yet additionally change the creation of collagen cross-connecting and accordingly advance injury mending.

LESS HEARTBURN:

Researchers found that the normalized Aloe Vera extract in syrup decreases a few side effects such as gastroesophageal, reflux illness (GERD), including heartburn, belching, and vomiting over a period of four weeks. It has a calming property as well as acts as cancer prevention agent.

LOWERS BLOOD SUGAR:

A part of clinical preliminary studies found that two tablespoons of Aloe Vera squeeze intake consistently brought down sugar levels.

A PAIN RELIEVER:

Salicylic acid found normally in Aloe Vera is a compound that give aspirin its anti-inflammatory effects. The Aloe Vera may assist the lessening of chronic pain that is not connected with disease.

A WAY TO KEEP PRODUCE FRESH:

Aloe Vera gel applied on the exterior of tomatoes helped delay ripening, supported keeping up with their quality and freshness and prevents specific bacteria from developing[21].

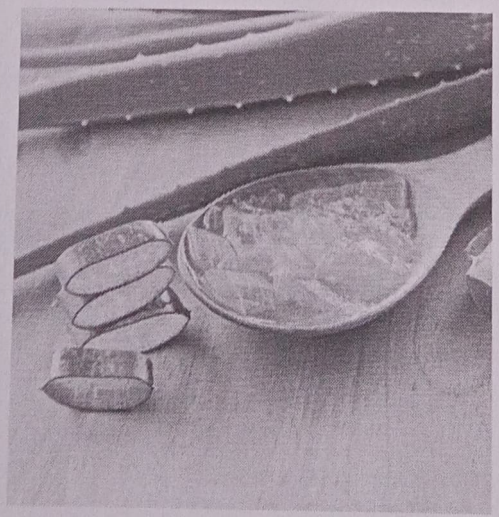

Fig 1.4

CHAPTER 2

PREPARATION OF PURE NiO NANOPARTICLES

2.1 INTRODUCTION:

The approach to synthesis of nano particles can be divided into top-down and bottom-up methods. This includes sol-gel process, spray pyrolysis, co-precipitation, hydro-thermal synthesis and inert gas condensation. Here we synthesized the NiO nano particles by Co-precipitation method[22][23].

2.2 CHEMICAL APPROACH:

In the chemical approach, the main components are the metallic precursors, stabililizing agents and reducing agents (organic and inorganic both). Reducing agents such as sodium citrate, ascorbate, sodium borohydride (NaBH4), elemental hydrogen, polyol process, tollens reagent, N, N-dimethylformamide (DMF) and poly(ethylene glycol)-block co polymers are used[24].

2.3 GREEN APPROACH FOR SYNTHESIS OF NiO NPs:

Green synthesis is more beneficial than traditional chemical synthesis because it costs less, decreases pollution and improves environmental and human health safety. At present green synthesis mainly uses micro-organisms (fungi, bacteria and algae) or extracts from leaves, flowers, roots, peelings, seeds of various plants. In the presence of green materials and under suitable conditions (temperature, concentration, ambient air and others) metal nanoparticles can be synthesised. Physical and chemical approaches of synthesizing nano particle have posed several stress on environment due to their toxic metabolites. Generation of nano particles from green techniques can be created effortlessly and they are fairly smart too. Green methods are significantly attractive because of their potential to reduce the toxicity.

ADVANTAGES:

- Non - toxic.
- Pollution free.
- Environmentally – friendly.
- Economical and more sustainable [25].

2.4 CO-PRECIPITATION METHOD:

2.4.1 CO-PRECIPITATION:

Co-precipitation as a simple technique is usually used for the preparation of inorganic and metal-based nanoparticles. Iron oxide nanoparticles are widely famous in the biomedical field for several advantages, and they are frequently synthesized using co-precipitation method. This method has several advantages such as high product yield, environmentally friendly solvent, and narrow size distribution. The precipitation is included by the addition of a base under stirring at room temperature under a non-oxidation atmosphere, leading to the formation of nanoparticles.

2.4.2 CHARACTERISTICS OF CO-PRECIPITATION:

- The products are generally insoluble species formed under conditions of high super saturation.
- Nucleation is a key step, and a large number of small particles will be formed.
- Secondary processes such as Ostwald ripening and aggregation, dramatically affect the size, morphology, and properties of the products.
- The super saturation conditions necessary to induce precipitation are usually the result of a chemical reaction.

2.4.3 TYPICAL CO-PRECIPITATION SYNTHETIC METHODS:

- Metals formed from aqueous solutions, by reduction from non -aqueous solutions, electrochemical reduction, and decomposition of metal organic precursors.

- Oxides formed from aqueous and non-aqueous solutions.
- Metal chalconides formed by reactions of molecular precursors.
- Microwave/sonication- assisted co-precipitation.

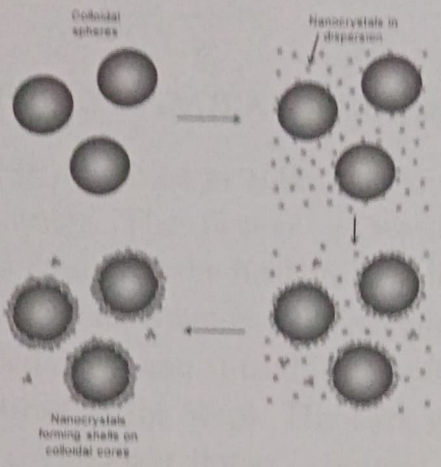

Fig 2.1

2.4.4 ADVANTAGES:

- Simple and rapid preparation.
- Easy control of particle size and composition.
- Various possibilities to modify the particle surface state and overall homogeneity.
- Low temperature.
- Energy efficient.
- Does not involve use of organic solvent.

2.4.5 DISADVANTAGES:

- Not applicable to uncharged species.
- Trace impurities may also get precipitated with the product.
- Time consuming.
- Batch -to-batch reproducibility problems.
- This method does not work well if the reactants have very different precipitation rates [26].

2.5 MATERIAL PREPARATION:

In the present work, pure NiO nanoparticles are prepared by Co-precipitation method. This method is simplest and convenient pathway to synthesize nano particles.

2.5.1 SYNTHESIS OF PURE NiO NANOPARTICLES:

1 mole of Nickel is dissolved in 100ml of Aloe Vera extract mixed with distilled water. The beaker is washed well with Ethanol. The mixture is poured in the beaker, kept in the magnetic stirrer and stirred thoroughly for 3 hours. 50ml of ethanol and 50ml of distilled water is added again and stirred for another 15 minutes. The beaker is kept undisturbed for hours. The dark green colour of nickel solely disappears. The clear liquid is poured out now 50ml of ethanol and 50ml of distilled water is added and again stirred for 3 hrs. Now the liquid changes into pale green colour. The procedure is repeated for 4 times. The liquid thus obtained is a very pale green liquid. The sample is filtered and heated in hot air oven at 150°C for 6 hours. The dried sample is divided into 3 parts and each part is kept in the muffle furnace at different temperature, 500°C, 600°C and 700°C respectively for 6 hours. The precipitate thus obtained is finely powdered. Thus the nano particles of NiO is obtained.

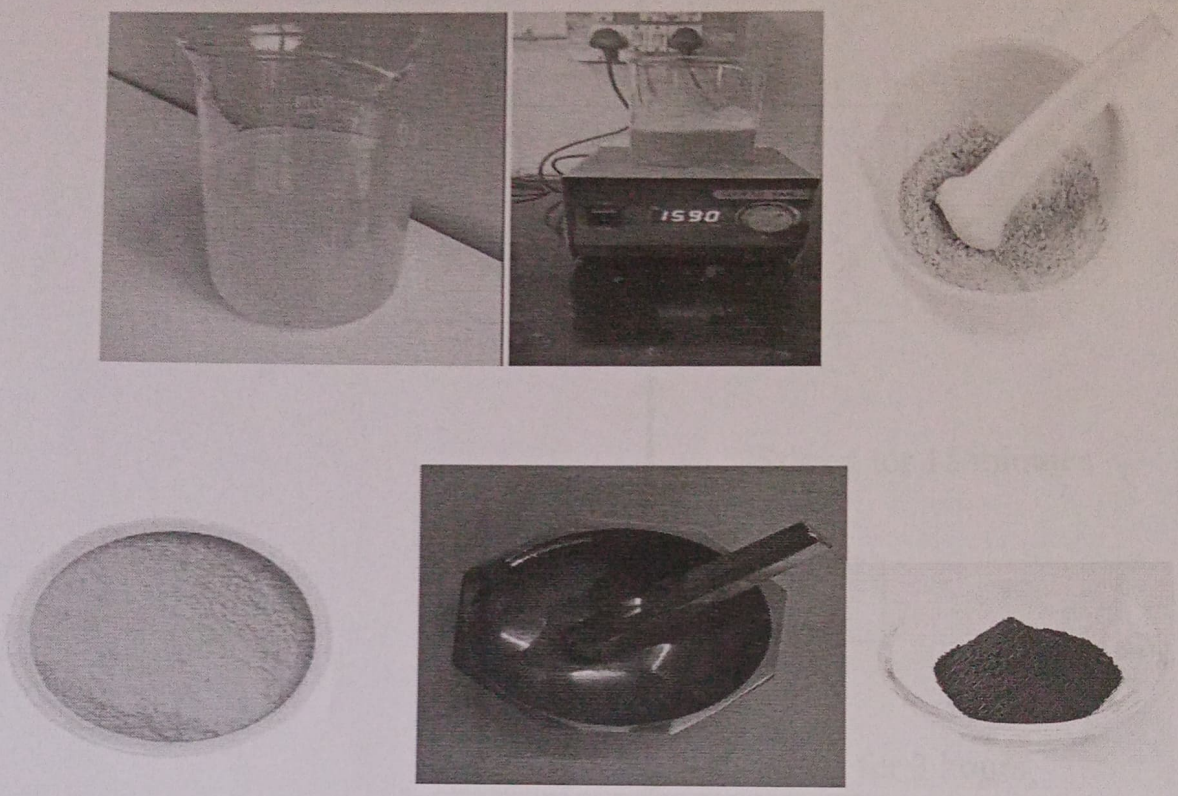

Fig 2.2

2.6 FLOWCHART:

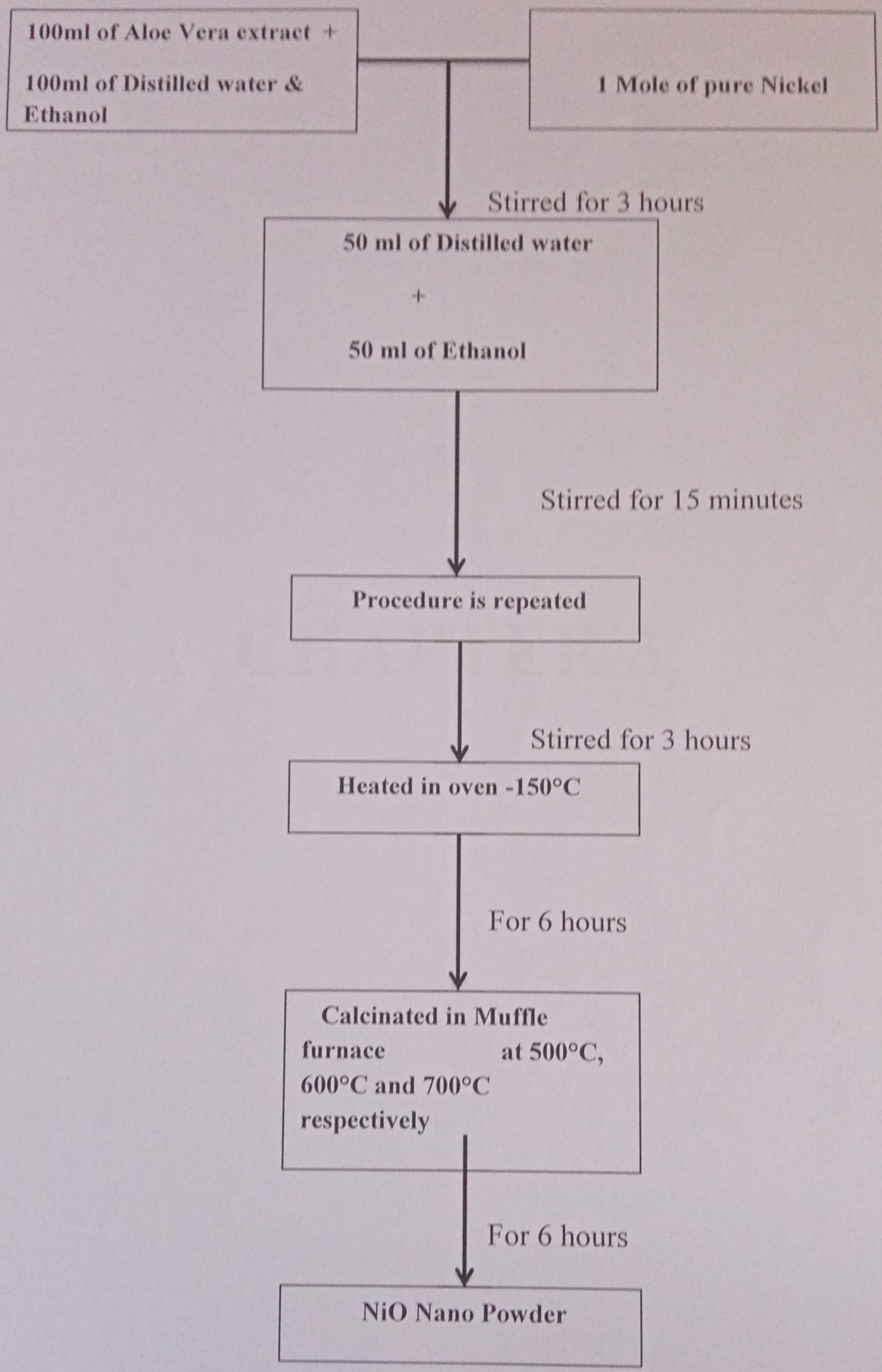

CHAPTER 3

CHARACTERIZATION

3.1 INTRODUCTION:

After the synthesis of NPs it is must to ponder the morphology and other conformational subtle elements by utilizing different spectroscopic strategies. The most widely utilized systems are: UV-via absorption spectroscopy, X-ray diffraction (XRD), Fourier transmission infrared (FTIR) spectroscopy, dynamic light scattering (DLS), energy dispersive X-ray examination (EDAX), scanning electron microscopy (SEM), transmission electron microscopy (TEM) and so on.

3.2 XRD SPECTROSCOPY:

X-ray diffractograms of nano-materials give an abundance of data from phase creation to crystallite estimate, from cross section strain to crystallographic introduction, XRD is non-contact and non-destructive, which makes it ideal for in situ studies[27].

Other techniques for characterization of NPs are EDS and DLS, the energy dispersive spectroscopy (EDS) is used to separate the characteristic X-rays of different elements into an energy spectrum, is used for detection of elemental composition of metal NPs. Dynamic light scattering analysis of incident photons is used to determine the surface charge and the hydrodynamic radius of the NPs.

3.2.1 X-RAY DIFFRACTION (XRD):

X-ray diffraction is based on constructive inference of monochromatic X-rays and a crystalline sample. These X-rays are generated by a cathode ray tube, filtered to produce monochromatic radiation, collimated to concentrate, and directed toward the sample. The interaction of incident rays with the sample produces constructive interference (and a diffracted ray) when condition satisfy Bragg's law,

$$2d\sin\Theta=n\lambda$$

where,

n is the order of the diffracted beam.

λ is the wavelength of the incident X-ray beam.

d is the distance between adjacent planes of atom (the d-spacing).

Θ is the angle of incident X-ray beam.

When a crystal is bombarded with X-rays of a fixed wavelength (similar to spacing of the atomic-scale crystal lattice planes) and at certain incident angles, intense reflected X-rays are produced when the wavelengths of the scattered X-rays interfere constructively. In order for the waves to interfere constructively the difference in the travel path must be equal to integer multiples of the wavelength. When this constructive interference occurs, a diffracted beam of X-rays will leave the crystal at an angle equal to that of the incident beam.

Bragg's law:

$$n\lambda = 2d \sin\Theta$$

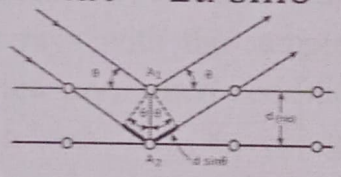

Fig 3.1

A similar process occurs upon scattering neutron waves from the nuclei or by a coherent spin interaction with an unpaired electron. These re-emitted waves interfere with each other either constructively or destructively (overlapping waves either add up together to produce stronger peaks or are subtracted from each other to some degree), producing a diffraction pattern on a detector or film. The resulting wave interference pattern is the basis of diffraction analysis.

3.2.2 INSTRUMENTATION AND CHARECTERIZATION:

X-RAY POWDER DIFFRACTION ANALYSIS:

X-ray powder diffraction (XRD is a rapid analytical technique primarily used for phase identification of a crystalline material and can provide information on unit cell dimensions. The analysed material is finally ground, homogenized, and average bulk composition is determined.

PRINCIPLE:

Max von Laue, in 1912, discovered that crystalline substances act as three dimensional diffraction gratings for X-ray wavelengths similar to the spacing of planes in a crystal lattice. X-ray diffraction is now a common technique for the study of crystal structures and atomic spacing.

X-ray diffraction is based on constructive interference of monochromatic X-rays and a crystalline sample. These X-rays are generated by a cathode ray tube, filtered to produce monochromatic radiation, collimated to concentrate, and directed toward the sample. The interaction of the incident rays with the sample produces constructive interference (and a diffracted ray) when conditions satisfy Bragg's law ($n\lambda=2d\sin\Theta$). This law relates the wavelength of electromagnetic radiation to the diffraction angle processed and countered. By scanning the sample through a range of 2Θ angles, all possible diffraction directions of the lattice should be attained due to the random orientation of the powdered material. Conversion of the diffraction peaks to d-spacing's allows identification of the mineral because each mineral has a set of unique d-spacing's. Typically, this is achieved by comparison of d-spacing's with standard reference patterns.

3.2.3 X-RAY DIFFRACTOMETER:

A diffractometer is a measuring instrument for analysing the structure of a material from the scattering pattern produced when a beam of radiation or particles (such as X-rays are neutrons) interacts with it.

X-ray diffractometers consist of three basic elements: an X-ray tube, a sample holder, and an X-ray detector. X-rays are generated in a cathode ray tube by heating a filament to produce electrons, accelerating the electrons toward a target by applying a voltage, and bombarding the target material with electrons[28].

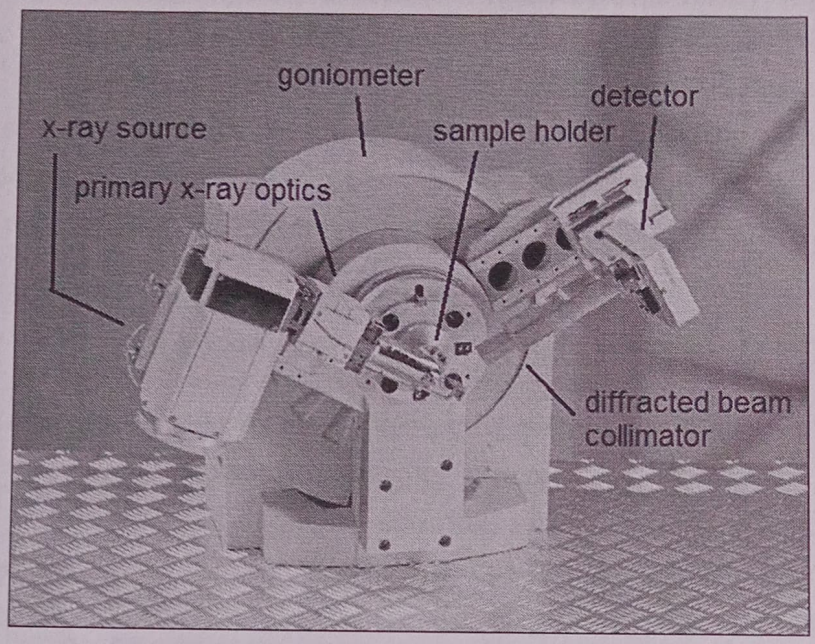

Fig 3.2

3.3 SCANNING ELECTRON MICROSCOPY:

THE ROLE OF ELECTRONS:

As the name implies, electron microscopes employ an electron beam for imaging. You can see the various products that are possible as a result of the interaction between electrons and matter. All these different types of signals carry different useful information about the sample and it is the choice of the microscope's operator which signal to capture. In SEM, two types of electrons are primarily detected:

- Backscattered electrons (BSE)
- Secondary electrons (SE)

Backscattered electrons are reflected back after elastic interactions between the beam and the sample. Secondary electrons, however, originate from the atoms of the sample: they are a result of inelastic interactions between the electron beam and the sample. BSE come from deeper regions of the sample, which SE originate from surface regions. Therefore, BSE and SE carry different types of information. BSE images show high sensitivity to differences in atomic number: the higher the atomic number, the brighter the material appears in the image. SE imaging can provide more detailed surface information.

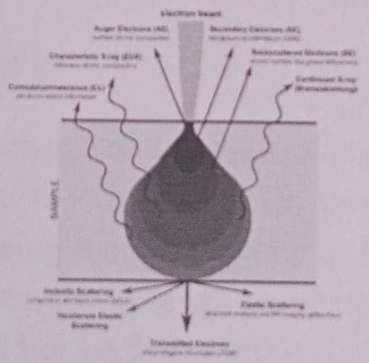

Fig 3.3

3.3.1 SCANNING ELECTRON MICROSCOPE: ELECTRON BEAM AND ELECTRON COLUMN:

Electrons are emitted from the filament of an electron source and subsequently collimated into a beam. The electron beam travels through

the electron column, which consists of a set of lenses that focus the beam onto the sample surface. Electron microscope lenses can be electrostatic or magnetic, depending on whether they use an electrostatic field or a magnetic field to focus the electron beam. To better understand how electrons can be deflected in a electrostatic field.

DEFLECTORS:

Electrons are negatively charged particles and travel through the electron column at high energy and high speed. One way to deflect these particles is to let them travel through an electric field generated by two plates at potential +U and –U, Under the influence of the electric field, the electron is deflected at an angle that depends on the electron energy, the electric field applied in between the plates, and the length of the plates. The faster, or the more energetic the electron, the smaller the deflection angle. The higher the electric field and the longer the plates the bigger the deflection angle. A device consisting of two plates at different potential is called a deflector.

To get an electrostatic lens, one could think of mirroring the effect of a deflector, such that the outer electrons travelling of the optical access can be focused on the same point. Whenever there is a lens effect, the energy of the beam changes, ie the electrons either accelerate or decelerate. This can be done simply by having an aperture on different potential around the beam.

ELECTROSTATIC LENSES:

Electrostatic lenses consist of metallic plates connected to high voltage with an aperture that the electron beam travels through. Single-aperture lenses consist of a single metallic plate at high voltage and can often be found in electron sources. The single-aperture lenses can either terminate an accelerating field or be followed by an accelerating field. In the first case, the lens is positive, meaning that the beam converges into a crossover, while in the second case, the lens is negative, meaning that the beam diverges.

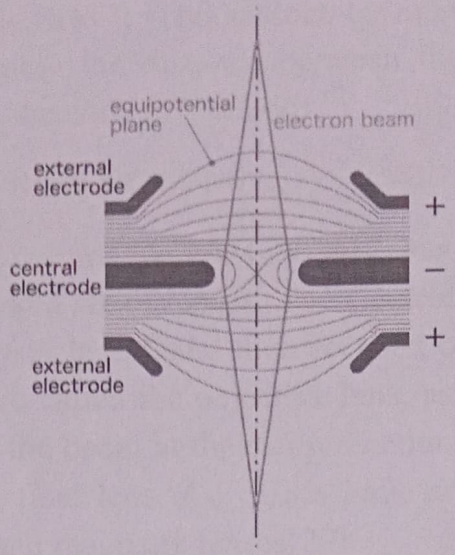

Fig 3.4

A two-aperture lens consists of two metallic plates at different potential with aligned apertures. In an accelerating two aperture lens, the electric field is placed in between the two plates points at the top plate. The electrons that enter this lens will feel a strong field that pushes them closer to the optic axis. As they travel through the second plate, the electrons feel an opposite force that pushes them towards the aperture. As a total effect, this is a positive lens and the beam is focused in a plane below the second plate.

A three-aperture Einzel lens consists of three plates with aligned apertures that can either have the same diameter or a different one. Einzel lenses are commonly used in electron optics for the advantage of having an equal beam potential at the entrance and exit of the lens. The three electrodes generate three lenses: the first and the third are positive, where the electric field lines point towards the plates and the second is negative. The total lens is positive and the beam is focused on a plane below the third lens.

MAGNETIC LENSES:

Magnetic lenses use the Lorentz force, that is proportional to the electron charge and velocity, to deflect electrons. Magnetic lenses consist of a metallic body (called the ferromagnetic circuit) that ends with two pole pieces. The magnetic field is given by a coil positioned at the top of the ferromagnetic circuit, The strength of the lens can be altered by

varying the magnetic field B. This is done by modifying the geometry of the pole piece, namely the distance between the pole pieces, and the current flowing into the coils (excitation).

THE SEM ELECTRON COLUMN:

The electron column consists of the electron source, where the electrons emitted, and a set of lenses. The electrons are condensed into a beam by the condenser lenses and then focused onto the sample surface by the final lens, also called the objective lens, as shown. The source tilt and the scanning of the beam at the sample is done by coils at the source and right above the final lens. All SEMs have an electron column with electrostatic lenses and magnetic lenses[29].

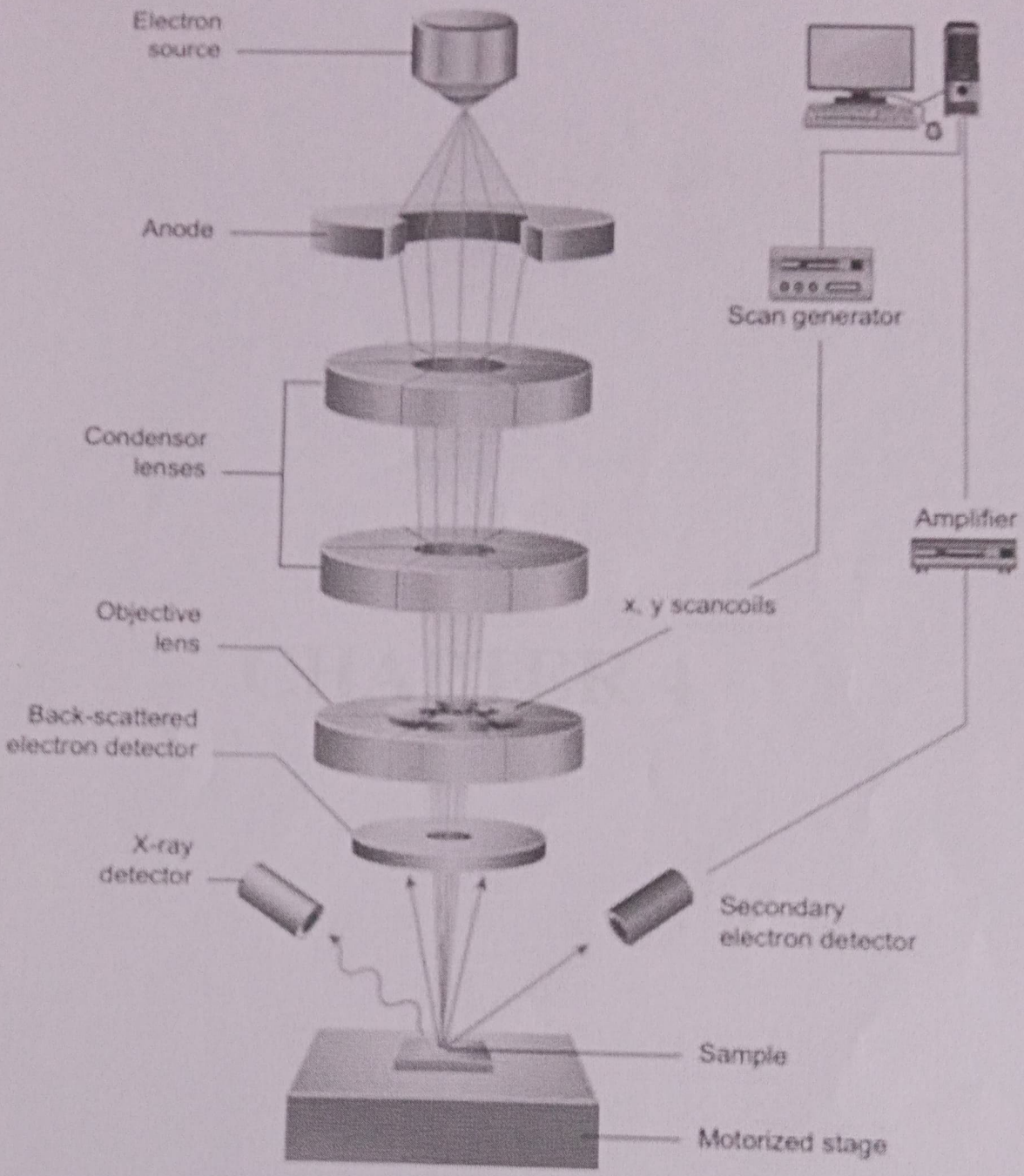
Electron source
Anode
Condensor lenses
Objective lens
Back-scattered electron detector
X-ray detector
Scan generator
Amplifier
x, y scancoils
Secondary electron detector
Sample
Motorized stage

Fig 3.5

CHAPTER 4

4.1 Characterization using XRD:

XRD profile investigation is a simple and effective technique to assess the crystallite size of the nanoparticles. The X-ray diffraction experiment are carried out with a XPERT-PRO diffraction system using the Cuk $\propto$ radiation of wavelength 1.5406A°. The type of the scan used is continuous and ranging from 10° to 80°. The average grain size is calculated using the Debye Scherrer formula,

$$\mathbf{D} = \frac{K\lambda}{\beta \cos\theta} \ \mathbf{(nm)}$$

Where,

- D is the mean size of the ordered (crystalline) domains, which may be smaller or equal to the grain size or the particle size. (nm)
- K is the dimensionless shape factor, with a value close to unity (0.9)
- λ is the wavelength of the X-Ray radiation [λ =1.5406 A°]
- β is the line broadening at half the maximum intensity (FWHM)
- θ is the angle of diffraction. (degree)

The dislocation density is found out using the formula,

$$\delta = 1/D^2 \ \mathbf{(lines/sq.m)}$$

Fig.4.1 depicts the XRD pattern of the pure NiO nanoparticles calcined at 500^0 C. Well defined diffraction peaks are observed in the figure corresponding to (2 2 0), (2 2 2), (4 0 0), (4 4 0) and (6 2 2) planes of NiO nanoparticles, which are in accordance with the standard spectrum (JCPDS : 89-5881).

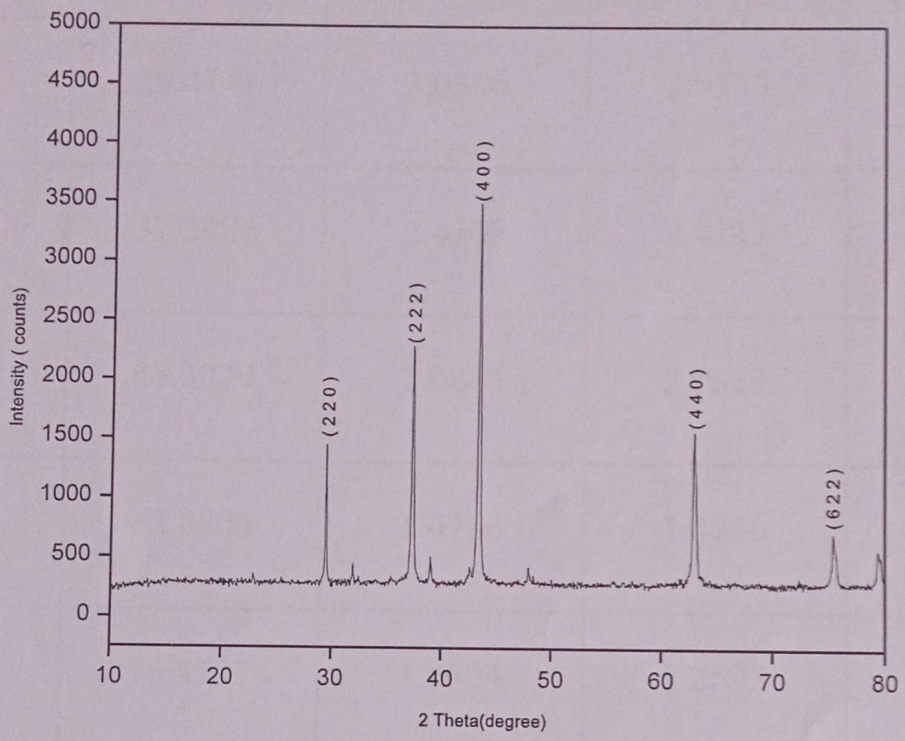

Fig.4.1. XRD pattern of the pure NiO nanoparticles calcined at 500^0 C

The d-spacing values obtained from XRD data of the NiO nanoparticles calcined at 500^0 C and their respective plane values corresponding to JCPDS card No. 89-5881 are presented in table 4.1.

Table 4.1. Comparison of standard and observed d-spacing values for the NiO nanoparticles calcined at 500^0 C

S.No.	2θ (degree)	Observed d- spacing	JCPDS d-spacing	hkl
1.	29.4141	3.0366	2.9533	2 2 0
2.	37.2986	2.4108	2.4113	2 2 2
3.	43.3229	2.0885	2.0883	4 0 0
4.	62.8806	1.4780	1.4766	4 4 0
5.	75.4131	1.2604	1.2592	6 2 2

Fig.4.2. represents the XRD pattern of the pure NiO nanoparticles calcined at 600^0C. Well defined diffraction peaks are observed in the figure corresponding to (2 2 2),
(4 0 0), (4 4 0) and (6 2 2) planes of NiO nanoparticles, which are in accordance with the standard spectrum (JCPDS : 89-5881).

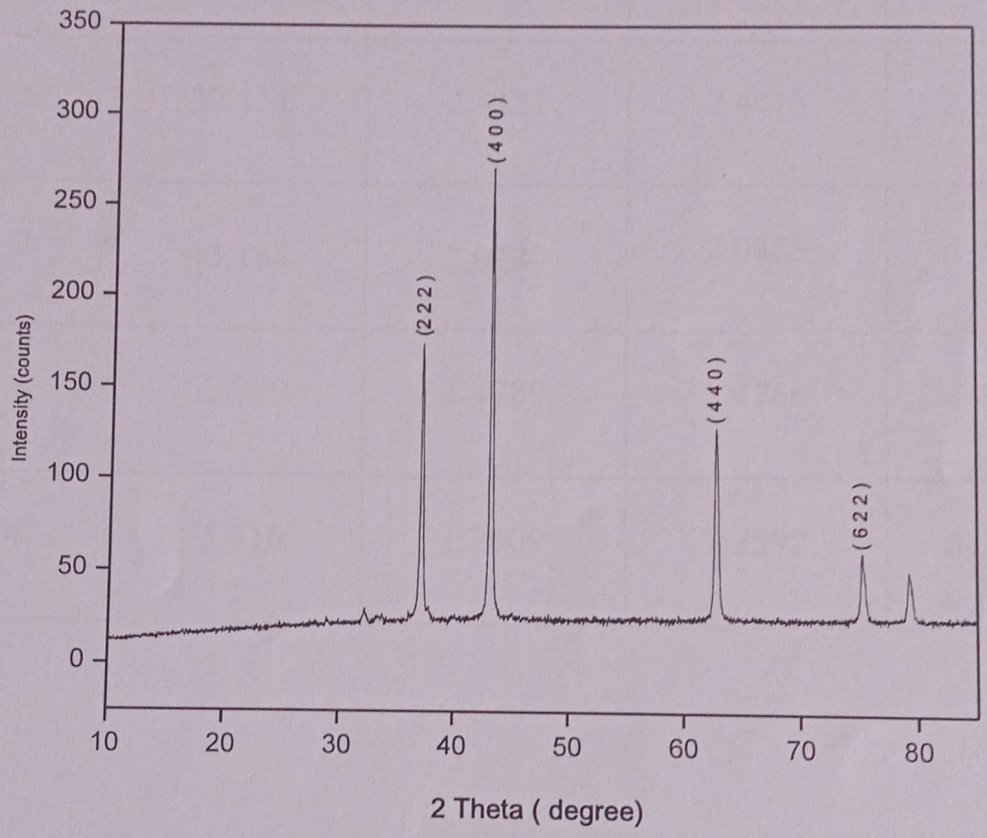

Fig.4.2. XRD pattern of the pure NiO nanoparticles calcined at 600^0 C

The d-spacing values obtained from XRD data of the NiO nanoparticles calcined at 600^0 C and their respective plane values corresponding to JCPDS card No. 89-5881 are presented in table 4.2.

Table 4.2. Comparison of standard and observed d-spacing values for the NiO nanoparticles calcined at 600^0 C

S.No.	2θ (degree)	Observed d- spacing	JCPDS d-spacing	hkl
1.	37.151	2.4181	2.4113	2 2 2
2.	43.188	2.0930	2.0883	4 0 0
3.	62.779	1.4789	1.4766	4 4 0
4.	75.310	1.2609	1.2592	6 2 2

Fig.4.3. represents the XRD pattern of the pure NiO nanoparticles calcined at 700^{0}C. Well defined diffraction peaks are observed in the figure corresponding to (2 2 2),
(4 0 0), (4 4 0) and (6 2 2) planes of NiO nanoparticles, which are in accordance with the standard spectrum (JCPDS : 89-5881).

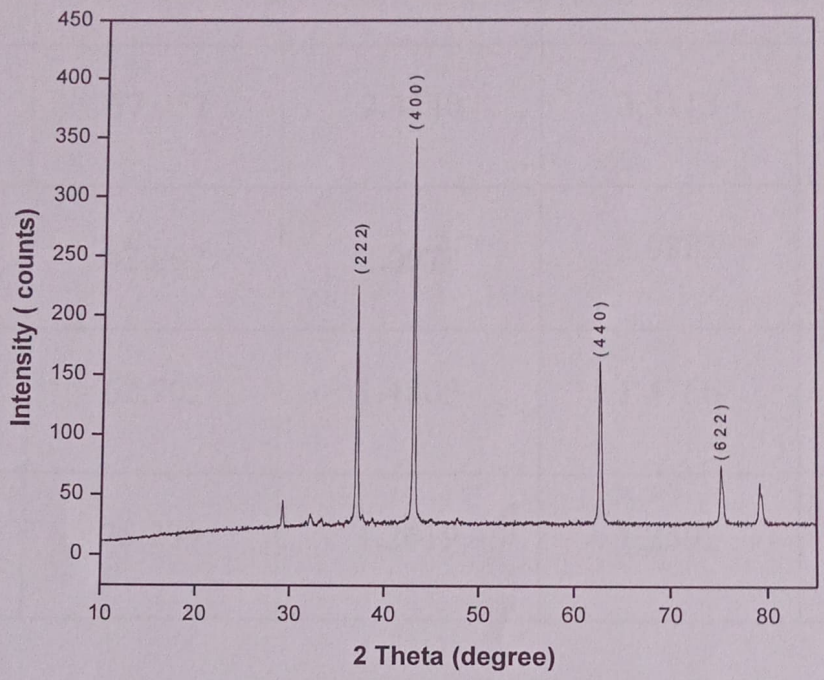

Fig.4.3. XRD pattern of the pure NiO nanoparticles calcined at 700^0 C

The d-spacing values obtained from XRD data of the NiO nanoparticles calcined at 700^0 C and their respective plane values corresponding to JCPDS card No. 89-5881 are presented in table 4.3.

Table 4.3. Comparison of standard and observed d-spacing values for the NiO nanoparticles calcined at 700^0 C

S.No.	2θ (degree)	Observed d- spacing	JCPDS d-spacing	hkl
1.	37.057	2.4240	2.4113	2 2 2
2.	43.097	2.0972	2.0883	4 0 0
3.	62.702	1.4805	1.4766	4 4 0
4.	75.239	1.2619	1.2592	6 2 2

The crystallite size calculated using Debye Scherrer formula and dislocation density of all the samples are given in table.4.4.

S.No.	Sample	Crystallite size (nm)	Dislocation density (lines/sq.m)× 10^{15}
1.	NiO nanoparticles calcined at 500^0 C	52	0.369822
2.	NiO nanoparticles calcined at 600^0 C	32	0.976562
3.	NiO nanoparticles calcined at 700^0 C	30	0.111111

All samples exhibits cubic structure as confirmed with the JCPDS file no.89-5881.The XRD patterns of the prepared NiO nanoparticles shows cubic crystal structure confirming the synthesis process efficiency. These observations indicate that the particle size of NiO nanoparticles decreases with increasing annealing temperature. This decrease in particle size may be due to the addition of Aloe vera extract during the synthesis process. In all the three samples, the high intense peak appears at $2\theta=43^0$. Thus, it appears that the crystallite size may be controlled by varying the annealing temperature of the sample.

4.2. Characterization using SEM:

The effect of annealing temperature on the surface morphology of the NiO nanoparticles was assessed by SEM. SEM micrographs of NiO annealed at different temperatures are shown in Fig. 4.4 – 4.6.

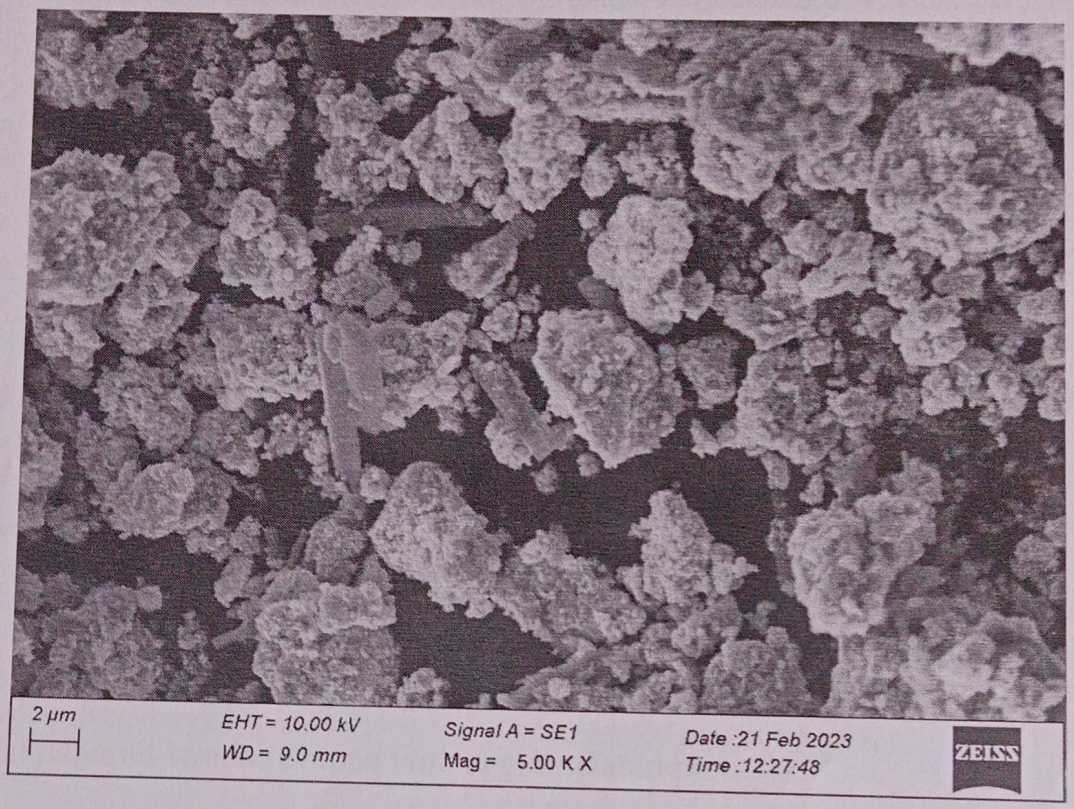

Fig.4.4. SEM image of NiO nanoparticles calcined at 500^0C

The SEM image of NiO nanoparticles calcined at 500^0C exhibits nanorod structure along with agglomerated flower patterns.

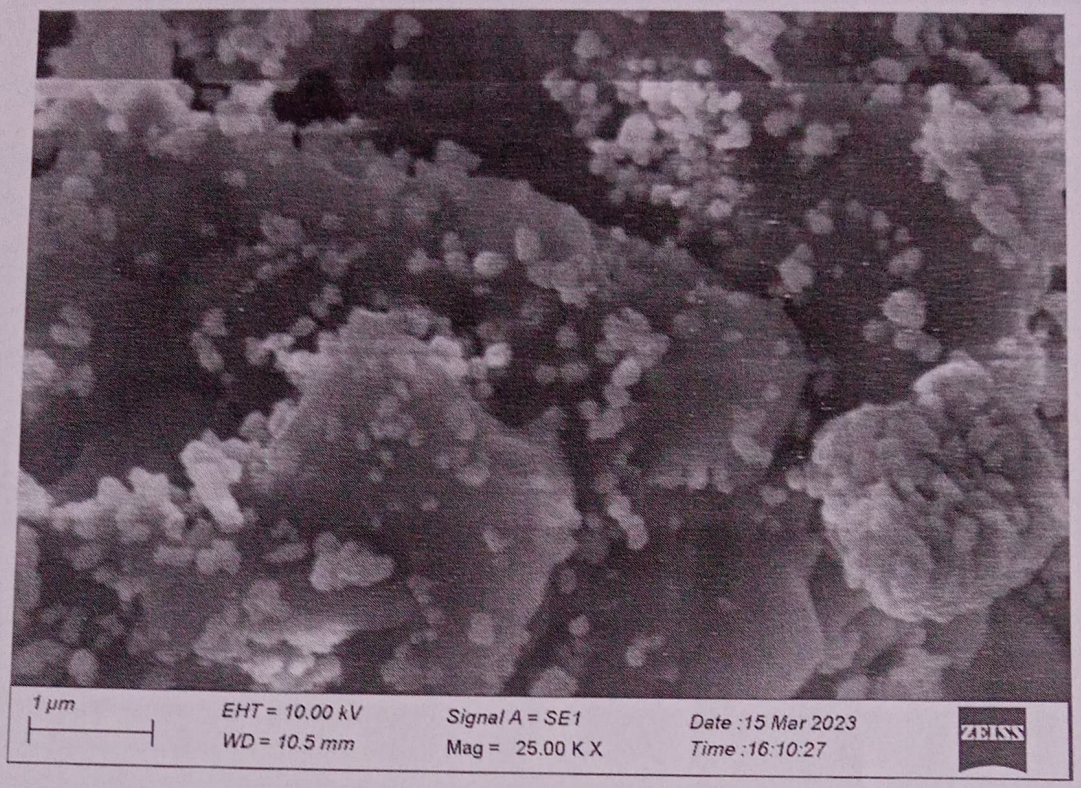

Fig.4.6. SEM image of NiO nanoparticles calcined at 700^0C

The SEM image of NiO nanoparticles calcined at 700^0C exhibits spherical structure along with agglomerated particles.

From SEM analysis, It is noted that the agglomerations might be due to the overlapping of the small and medium particles, which have been caused by various kinds of forces such as weak surface force (soft agglomerates), strong chemical bonds (hard agglomerates), and lack of water on the surface structures. The annealing temperature interferes with the crystal structure and the material's morphology, which affects the specific surface area.

CHAPTER 5

5.1 CONCLUSION:

In this present investigation, the NiO nanoparticles were synthesized via Green route using Aloe vera extract as a reducing agent. This method is an ecofriendly approach to synthesis of NiO nanoparticles without adding any surfactant. The samples were treated with three different temperature at 500^0C , 600^0C and 700^0C to study the structure and morphology. XRD analysis revealed that the annealing temperature has high impact on the crystallinity. Therefore, annealing temperature improves the nanomaterial crystallinity, causes phase transformation, and affects photocatalytic activity. The size of the NiO nanoparticles decreases with increasing annealing temperature. This decrease in particle size may be due to the addition of Aloe vera extract during the synthesis process. SEM analysis illustrates the rising of calcination temperatures resulting in proximal clustering which are bounded to another.

5.2 Bibiliography:

[1] Dr. Yashwanth Kumar: Nanoscience and Nanotechnology, (2016) pg(1-2), (14-15).

[2] https://www.em-nano.org/what-is-nanoscience-nanotechnology/

[3] https://ntp.niehs.nih.gov>factsheets

[4] Khan, I; Saeed, K. and Khan, I., et al., (2019)Nanoparticles: properties, applications and toxicities: Arabian Journel of Chemistry, 12(T), pp. 908-931.

[5] Shevchenko, V, Y., Madison, A.E. et al.,(2002)Nanoparticles: 1 Generalized Crystallography of nanoparticles and Magic numbers Glass Physics and chemistry 28, pg 40-43

[6] https://www.researchgate.net

[7] Muhammed Imran Din et al.,(2015) Recent Advances in the Synthesis and stabilization of Nickel Oxide Nanoparticles. A Green Adeptness: International journal of Analytical Chemistry. Volume 2016, Article ID 3512145 pages 14.

[8] Dhivya Christo Anitha et al.,(2019) Synthesis of NiO Nanoparticles using Thespesia populnea Leaves by Green Synthesis method :EPRA International journal of Research and Development [IJRD] Volume:4;Issue:9.

[9] Abdul-Ameer(2018),Novel Co-precipitation Method for synthesis of Nano structured Nickel Oxide in Accordance to PH: Structural and optical filter: Ibn Al-Haitham journal for pure and Applied Science:Volume.32(1).

[10] Vijaya Kumar et al.,(2019) Synthesis and characterization of NiO nanoparticles by chemical as well as green routes and their comparisons with respect to cytotoxic effect and toxicity studies in microbial and MCF-7 Cancer Cell Models: SN Applied science(2019) 1:1083.

[11] Pooja Khandagale et al.,(2017)Synthesis& Characterization of Nickel Oxide Nanoparticles by using Co-precipitation method: InternationalJournalofAdvanced Research(IJAR):10:21474/IJAR01/4253.

[12] Siraj Uddin et al.,(2020)Green synthesis of Nickel oxide nanoparticles using leaf extract of Berberis balochistanica: Characterization and diverse biological applications: Microscopy research and technique.

[13] Karpagavinayaganam et al.,(2019)Ecofriendly synthesis of Nickel oxide nanoparticles using Avicennia Marina leaf extract: Morphological Characterization and electrochemical application: elsevier.com/locate/matpr:10.1016

[14] Angel Ezhilarasi et al.,(2016)Green synthesis of NiO nanoparticles using Moringa Olifera extract and their bio medical applications: Cytotoxicity effect of nanoparticles against HT-29 Cancer cells(JPB 10602)S1011-1344(16)30756-4.

[15] Infantia Stephan Grace etal.,(2019)Synthesis and Characterization of Nickel oxide nanoparticles by sol-gel technique: API Conference Proceedings 2244,070017(2020).

[16] Zahara Sabouri et al.,(2018)Facile green synthesis of NiO nanoparticles and investigation of dye degradation and cytotoxicity effects: Journal of Molecular Structure: MOLSTR 25468.

[17] Israa Muzham Rashid et al.,(2021)Green synthesis of Nickel oxide nanoparticles for Adsorption of Dyes: Sains Maalaysiana 51(2)(2022): 533-546.

[18] Mohd Kashif Aziz et al.,(2022)The biosynthesis of nickel oxide nanoparticles using Watermelon rind extract and their biophysical effects on the germination of Viga radiata seeds at various concentrations: International Journal of Science and Research Archive, 2022, 07(02), 245-254.

[19] P.Ghosh et al., (2016)Reference module in materials science and materials engineering(chapter 9204).

[20] Y.Bahari Molla Maheleh et al.,(2008) NiO Nanoparticles Synthesis by chemical precipitation and Effect of Applied Surfactant on

Distribution of particle size: Journal of Nanomaterials, Volume 2008 Article ID 470595,pages 4.

[21] https://pharmeasy.in/blog/aloe-vera-gel-uses-and-uses/

[22] www.ncbi.nlm.nih.gov

[23] https://www.sciencedirect.com

[24] Zhang X-F, Liu Z-G et al.,(2016)Silver nanoparticles: synthesis, characterization, properties, applications and therapeutic approaches. IJMS. vol 17 pg 1534.

[25] Shuai Xuan Ying et al.,(2022)Green synthesis of nanoparticles: Current developments and limitations Volume(26).

[26] Ajay Vasudeo Rane et al.,(2018)Synthesis of Inorganic Nanomaterials.

[27]Anandalakshmi K, Venugobal J, Ramasamy V, (2019) Characterization of silver nanoparticles by green synthesis method using Pedaliummurex leaf extract and their antibacterial activity. Apply Nanoscience. vol 6 pg 399-408.

[28]https://serc.carleton.edu/research_educational/geochemsheets/techniqueue/XRD.html

[29]https://www.thermofisher.com/in/en/home/materials-science/learning-centre/applications/scanning-electron-microscope-sem-electron-column

5.3 IMAGES:

5.4 TABLE: